Doctoral Dissertation
Doctoral Program in Science and Material Technology (32th Cycle)

SERS active Ag/silicon based nanostructures for biosensing applications

Niccolò Paccotti

* * * * * *

Supervisors
Prof. F. Geobaldo
Prof. F. Giorgis

Doctoral Examination Committee:
Prof. Marina Scarpa, Referee, University of Trento
Prof. Ivano Alessandri, Referee, University of Brescia
Dott. Pietro Giuseppe Gucciardi, Referee, CNR of Messina.
Prof. Davide Luca Janner, Politecnico di Torino
Prof. Alberto Fina, Politecnico di Torino

Politecnico di Torino
October 31, 2019

I hereby declare that, the contents and organisation of this dissertation constitute my own original work and does not compromise in any way the rights of third parties, including those relating to the security of personal data.

…………………………………..…

Niccolò Paccotti

Turin, October 31, 2019

Summary

Surface Enhanced Raman Spectroscopy (SERS) has emerged as a powerful technique for the analysis of biological environments. Indeed, it combines the specific molecular information with the signal-enhancement provided by plasmonic nanostructures. The development of SERS-active platforms has undergone intense study to provide high-sensitivity label free devices that can be exploited in many fields, ranging from biomedical application, to environmental and food safety.

This written dissertation mainly consists in three parts. In the first section an introduction to the fundamentals of the SERS spectroscopy is provided (Chapter 1), followed by a brief discussion about the main techniques used to synthesize different typologies of SERS substrates and the characteristics, which make them suitable for the biosensing applications (Chapter 2). In particular, the distinctive properties of the porous Si-based substrates decorated with silver nanoparticles were presented, discussing the used materials and the methods (Chapter 3).

The second section concentrates on the development of a microfluidic protocol with the aim to optimize the synthesis of Ag nanoparticles on the previously mentioned porous Si-based substrates, in order to understand the effect of each synthesis parameter on the morphologies of the obtained plasmonic metal-dielectric nanostructures. The SERS efficiency of the produced substrates was then tested, checking the potential correlation between the SERS signal intensity and the nanoparticles morphology, considering the size distribution (Chapter 4).

Finally, the third section focuses on the biological applications of the silver nanostructures (Chapter 5). Two different studies were carried out: the first one was dedicated to the selective detection of a microRNA sequence (miR222, Section 5.2), whereas the second was focused on the discrimination of bacterial strains (Section 5.3).

In Section 5.2 two different protocols of biofunctionalization were presented, both exploiting the hybridization between the target miRNA and a complementary

probe, labelled with a Raman reporter. Each step of the assays was carefully optimized to achieve the maximum amount of hybridized molecules avoiding non-specific binding of the miRNA with the surface. Moreover, the selectivity of the assays was tested. In order to furtherly decrease the detection limit of the selected miRNA, several positions of the reporter along the oligoprobe were investigated. Finally, the detection of miR222 was carried out in cancer cells extracts.

The last section deals with characterization of the vibrational features of two bacterial strains belonging to different categories, namely Gram-negative and Gram-positive. To this aim, *E. coli* and *S. epidermidis* were cultured and then analysed. These two strains display several differences in the molecular composition of the outer membranes as well as in the content of the biofilm matrix. Such characteristics yielded peculiar vibrational features of each strain, which could be potentially affected by the bacterial population growth. In order to investigate such issue, the evolution of the bacterial population analysed over time, collecting samples after 12, 24, and 48 hours of culturing.

.

Acknowledgment

I would like to thank Giuseppe Pezzotti, Elia Marin, Francesco Boschetto, Matteo Zanocco e Alfredo Rondinella for hosting and helping me, during my stay at Kyoto Institute of Technology, and the Kyoto Integrated Science and Technology Bio-Analysis Center (KIST-BIC) for the support provided for the SERS measurements.

To my family

Contents

List of Tables

List of Figures

Chapter 1

1 SERS spectroscopy

1.1 Introduction

Surface Enhanced Raman Scattering (SERS) has been proven as one of the most promising approaches to investigate different systems, with applications ranging from analytical chemistry to the characterization of biological environments, emerging as an ultra-sensitive and non-destructive technique. These characteristics arise from the huge amplification of the Raman scattering of the molecular species adsorbed onto a nanostructured surface with defined optical properties, that allows to overcome the very low sensitivity of Raman spectroscopy while retaining the rich structural information of the vibrational spectra. Despite being a quite well-known effect, SERS still is one of the most studied techniques, aiming to improve both the efficiency and the reproducibility of the nanostructures supporting the SERS enhancement, as well as to integrate the experimental setup into complex detection systems, such as microfluidic sensing platforms.

In this first chapter the mechanism of Raman spectroscopy will be provided, as well as the description of the SERS effect.

1.2 Raman spectroscopy

Raman spectroscopy is an optical technique that allows gathering information about the vibrational features of the analysed samples exploiting the inelastic scattering of photons hitting its surface. The scattering phenomenon arises from the oscillation of the electron cloud due to the irradiation of the sample with a monochromatic light: as a result, a radiating dipole moment is generated. Such scattered light features three different frequencies: the majority of the collected photons is elastically scattered, preserving the original frequency, while some of them can be inelastically scattered at lower or higher frequencies (Figure 1.1a). The former phenomenon is named Rayleigh scattering whereas the latter are named Raman Stokes and anti-Stokes scattering, respectively.

Concerning an anisotropic system, the Raman effect can be described as follows (according to a classical approach).

$$\bar{\mu} = \sum_{j} \alpha_{ij} \bar{E} \tag{1.1}$$

The induced dipole moment $\bar{\mu}$ depends on the incident electric filed strength $\bar{E}$, and on the polarizability, α_{ij}, which is related to the chemical and structural properties of the sample.

For a diatomic molecule, the periodical change in the distance between the nuclei can be used to the describe the molecular vibration. Hereby a time-dependent electric field which is oriented along the X axis of the molecule is considered. A Taylor series is usually employed to represent the related variation of the polarizability as a function of the inter-nuclear distance, q_v, as shown in the following equation:

$$\alpha = \alpha^0 + \left(\frac{d\alpha}{dq_v}\right)_0 q_v + \cdots \approx \alpha = \alpha^0 + \left(\frac{d\alpha}{dq_v}\right)_0 q_v^0 \cos(2\pi\nu_v t) \tag{1.2}$$

The expression for the incident field, $\bar{E} = E_X^0 \cos(2\pi\nu t)$, where ν is the frequency of the incident wave, and equation 1.2 can be substituted in 1.1, giving a description of the induced dipole moment, which takes into account the three components of the scattering phenomenon:

$$\begin{gathered} \bar{\mu} = \bar{E} = E_X^0 \alpha^0 \cos(2\pi\nu t) + E_X^0 \left(\frac{d\alpha}{dq_v}\right)_0 q_v^0 \cos 2\pi\nu_v t \cos(2\pi\nu t) \\ \bar{\mu} = \bar{E} = E_X^0 \alpha^0 \cos(2\pi\nu t) + \\ \frac{E_X^0}{2} \left(\frac{d\alpha}{dq_v}\right)_0 q_v^0 \{\cos[2\pi(\nu - \nu_v)t] + \cos[2\pi(\nu + \nu_v)t]\} \end{gathered} \tag{1.3}$$

The Rayleigh scattering accounts for the first component, whereas the second one is related to the Raman scattering. In this case the incident field frequency is modified by the vibrational frequency of the molecule. Since $\left(\frac{d\alpha}{dq_v}\right)_0 \neq 0$ is required to preserve the second term, the Raman scattering is possible only upon a polarizability variation induced by the vibration, as can be foreseen by equation 1.3.

A semi-classic approach is however often needed to describe the interaction between a quantized system and an electromagnetic wave. An incident photon is able to excite an electron from the ground state to a virtual energy state, laying between the original and the excited ones. Subsequently, the electron will decay often returning to the ground state. However, it is possible that the electron will decay into a higher or lower energy state, with respect to the original one. In this case an absorption or release of energy modifies the frequencies of the scattered photons. It is worth to notice that the anti-Stokes scattering is usually less intense with respect to the Stoke one, because of the lower population of the excited levels (Figure 1.1)

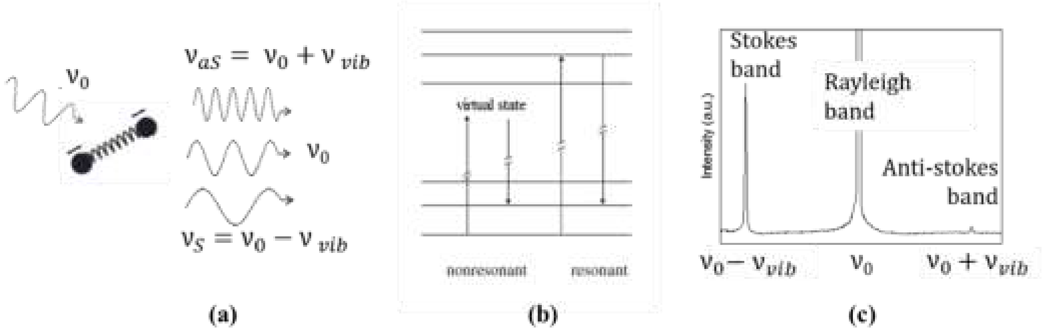

Figure 1.1 - a) Scheme of the Raman scattering effect b) energy levels involved in normal and resonant Raman (c) Raman spectrum displaying the Stokes, Rayleigh and anti-Stokes peaks

From the Figure 1.1b it can be inferred that the Raman cross section of a molecule can be increased if the incident light matches the energy gap between the ground and excited states, leading to an electronic resonance that causes an increased Raman signal of the recorded spectra.

Concerning a poly atomic molecule containing N atoms, 3N coordinates are required to describe the position of the involved atoms, while for simpler systems only the inter-nuclear distance is needed. Three of them, named translational coordinates, are needed to describe the centre of gravity of the molecule, whereas three more, named rotational coordinates, are required to define its orientation. At last, the vibrational conduct of the molecules requires 3N-6. coordinates Concerning linear molecules, only two degrees of freedom are available and therefore only 3N-5 coordinates are required. Usually the 3N-6 normal modes are employed to describe the vibrations of the system. Such modes are synchronous vibrations of groups of atoms, each one behaving as a harmonic oscillator with different energy levels. Characteristics such as the inter-atomic forces, the molecular geometry and lastly the atomic weight affect the frequencies of the normal modes, whose variation can be used to gain information about these properties.

Moreover, the normal modes can be classified, exploiting the group theory, based on their symmetry. Comparing it with the symmetry of the molecule in its the ground state, the selection rules for both the infrared (IR) and Raman activity can be determined. The law of mutual exclusion can be inferred from such analysis. This rule foresees that molecules displaying a centre of symmetry exhibit Raman active modes that are IR inactive, and vice versa. Concerning come complicated biomolecules, the correlation between IR and Raman spectroscopy persists.

1.3 Surface Enhanced Raman Scattering (SERS)

As for several scientific discoveries, also the first time that a Surface Enhanced Raman Scattering effect was observed it wasn’t recognized as such. In 1974 Fleischmann et al. studied the Raman scattering of the pyridine adsorbed onto a roughened silver electrode, but they ascribed the enhancement of the signal to the high surface area of the electrode [1]. A few years later a second team firstly recognized the huge enhancement of the pyridine Raman signal as a consequence of the enhanced electrical field thanks to the peculiar optical properties of the supporting materials [2]. In the following years the SERS effect was deeply studied in order to better understand its characteristics, leading to a strong improvement into the fabrication of the supporting materials, allowing to reach the single molecule detection limit.

Nowadays the enhancement explanation takes in account two different contributions:

- the electromagnetic enhancement (EM), based on the amplification of the electric field provided by nanostructures supporting Localized Surface Plasmons (LSP). This mechanism has been proven to be the most important, being responsible for the signal increase up to 10 orders of magnitude.
- the chemical enhancement (EC), due to charge transfers phenomena between the metal surface and the molecules.

Although with different impact both mechanism influence the Raman scattering intensity increase observed in SERS experiments. As can be seen in the following equation (1.4) the Raman scattering intensity, $P^{RS}(\nu)$, can be written as a function of the number of the excited molecules (N), the Raman scattering cross-section (σ_{free}^{R}) of the molecule, and the incident laser intensity $I(\nu_L)$:

$$P^{RS}(\nu) = N\,\sigma_{free}^{R}\,I(\nu_L) \tag{1.4}$$

If the local electrical field is instead enhanced, due to the adsorption of the involved molecules onto a nanostructured metallic surface, the previous equation has to be modified through the introduction of two more factors, $A(\nu_L)$ and , $A(\nu_{RS})$, related to the amplification of the EM field both of the incident laser and of the scattered light. Moreover, the exhibited Raman cross-section, σ_{ads} , can be larger due to the molecule-surface interactions, resulting in a modified expression for the SERS intensity:

$$P^{SERS}(\nu) = N'\,\sigma_{ads}\,|A(\nu_L)|^2|A(\nu_{RS})|^2 I(\nu_L) \tag{1.5}$$

where N' refers to the molecules involved in the SERS mechanism.

1.1.1 Electromagnetic enhancement

As stated in the previous section, the electromagnetic enhancement arises from the amplification of the electric field at the metallic surface. Such enhancement originates from the optical characteristics of the nanostructured material, and particularly from its ability to support Localized Surface Plasmons (LSP). Surface Plasmons are referred to as collective oscillations of the free electrons of a metal, which cause an oscillating electric field. Depending on the metal structure and the surrounding environment, these can propagate along the whole surface, as for metal /dielectric interfaces, or instead being highly localized, as for the case of metal nanoparticles in which the oscillation involves the valence band electrons that can be usually excited at certain frequencies. The next section will focus on the Localized Surface Plasmon Resonances and how they can affect the electromagnetic enhancement.

1.3.1.1 Localized Surface Plasmon Resonances

A metal nanoparticle with a radius smaller than the incident radiation wavelength can be considered subjected to a uniform EM field. Such EM field induces highly localized collective oscillations of the electron cloud, leading to the formation of a dipole charge density distribution at the surface and therefore to the production of an induced dipole moment. Given the oscillatory nature of the dipole is sign will periodically change. As a consequence, an EM field is produced by the oscillating electrons whose frequency matches the oscillating frequency of the electron themselves (Figure 1.2). The particle polarizability, which for a sphere is described by the equation 1.5, is responsible for the magnitude induced dipole [3],

$$\alpha = 4\pi\varepsilon_0(r)^2\frac{\varepsilon - \varepsilon_0}{\varepsilon + 2\varepsilon_0} \tag{1.5}$$

where ε_0 is the dielectric constant of the surrounding matrix, ε the one of the metal particles, and r is the particle radius. When $\varepsilon = -2\varepsilon_0$ the dipolar resonance is attained. If such condition is achieved, the polarizability (α) and consequently the amplitude of the field in the proximity of the nanoparticle are very high. SERS usually exploits such condition to increase the efficiency of the Raman scattering process.

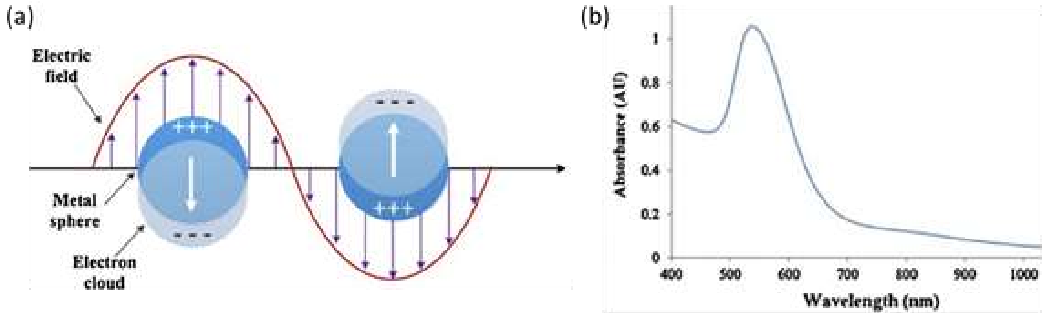

Figure 1.2 – (a) Scheme of charge separation induced by a homogeneous EM field surrounding metal particle with sub-wavelength dimensions (b) extinction spectrum of the related LSPR.

These conditions are well depicted in Figure 1.2, which shows the charge separation that takes place at the particle surface (left) as well as the corresponding extinction spectrum, which displays a single peak centred at the LSP resonance frequency. Two different contributions are convolved in this spectrum tough, originating from the adsorption and the scattering of the nanoparticle. Both of these contributions display a maximum at the resonance frequency, nevertheless the SERS enhancement arises only from the scattering phenomenon. The cross section of each of these mechanisms can vary, depending on the particle size and on the excitation wavelength (Figure 1.3). Indeed, for bigger particles the scattering mechanism is usually predominant, and therefore higher SERS enhancements are achieved.

After having introduced these basics concepts, a model for the electromagnetic enhancement concerning a metal nanoparticle with defined radius (r) and dielectric constant (ε), can be developed. Moreover, a supplementary term concerning the dielectric constant of the surrounding medium (ε_0) (Figure 1.5) has to be added. Therefore, if a molecule is located at a certain distance (d) from the nanoparticles, it will be exposed to an electromagnetic field, E_M, which is the sum of two different terms: the field scattered by the dipole induced in the nanoparticle, E_{SP} , and the incident field, E_0 .

As a result, the field enhancement factor can be expressed as in following equation.

$$(\nu) = \frac{E_M(\nu)}{E_0(\nu)} \sim \frac{\varepsilon - \varepsilon_0}{\varepsilon + 2\varepsilon_0} \left(\frac{r}{r+d}\right)^3 \tag{1.6}$$

A similar expression can be derived for the enhancement factor affecting the anti-Stokes and the Stoke. From the combination of these two factors a general enhancement of the Stoke signal can be derived, as shown in equation 1.7.

$$G(\nu) = |A(\nu_L)|^2 |A(\nu_S)|^2 \sim \left|\frac{\varepsilon(\nu_L) - \varepsilon_0}{\varepsilon(\nu_L) + 2\varepsilon_0}\right|^2 \left|\frac{\varepsilon(\nu_S) - \varepsilon_0}{\varepsilon(\nu_S) + 2\varepsilon_0}\right|^2 \left(\frac{r}{r+d}\right)^{12} \tag{1.7}$$

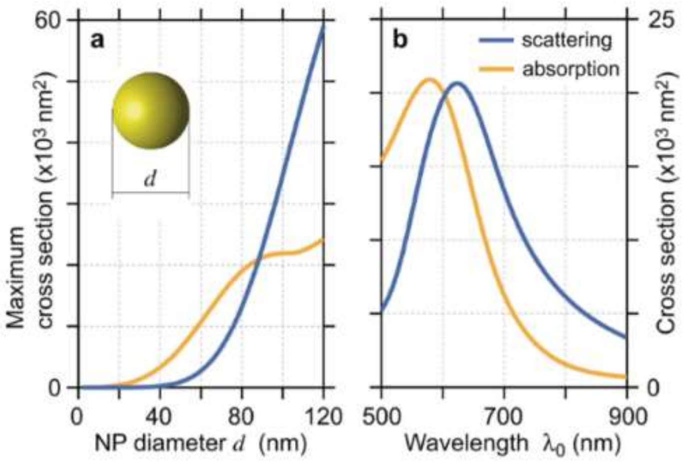

Figure 1.3 – (a) Evolution of the maximum absorption and scattering for increasing diameters of gold NPs. (b) Absorption and scattering cross section spectra for a gold nanosphere [4]

Even though a contact between the metal surface and the molecules is not required, $G(\nu)$ fades as $(1/d)^{12}$, and therefore only for limited distances a large EM enhancement can be expected. Moreover, an optimal enhancement occurs when the real part of the metal dielectric constant both at the laser and Raman scattering frequencies is close to -$2\varepsilon_0$. In order to maximize the enhancement, both the stokes scattered radiation and the frequency of the incident photons are required to match the plasmonic resonance frequency. This, as mentioned before, represents the dipolar resonance conditions of the particles. If such condition is exploited, the scattered enhancement is directly proportional to the fourth power of the local field [5], even though this can be considered realistic only for blue and green laser excitation.

Since the LSPRs excitation greatly influence the EM mechanism, a deep knowledge of their behaviour in a non-spherical and isolated system is important. The following sections deal with the influence on the LSPRs of differently shaped particles in a systems involving multiple interactions.

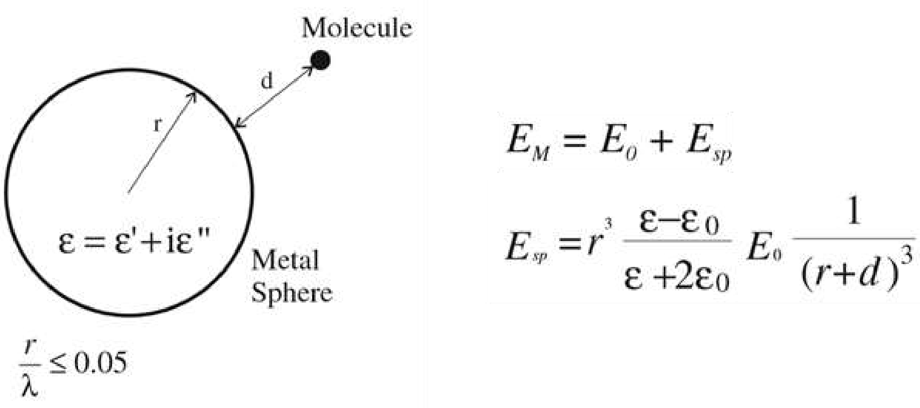

Figure 1.4 – Representation of the EM enhancement mechanism[6]

1.3.1.2 LSPRs in single particle systems: size and shape effect.

In the previous paragraph the generation of the LSPs has been explained taking advantage of the dipole approximation. However, this only applies to subwavelength nanoparticles. Dealing with larger nanoparticles implies the development of more complex models, that take into account the retardation effect of the electron cloud. A good prediction of the effect induced on the plasmonic features by the NP size is provided by the Mie theory, according to which a shift of the resonance wavelength towards lower energy is predicted as the particle diameter increases [7].

Moreover, the shape of the nanoparticles has to be taken into account since it could influence the LSRPs, causing the original plasmonic modes to split. Particularly concerning morphologies displaying sharp edges and corners which can promote the charge accumulation in such parts of the structures, therefore generating highly localized and strong electric field. Consequently, highly localized and strong electric field are generated and better SERS enhancement are attained.

Figure 1.5a shows the comparison between the calculated EM near-field distribution for spherical and pyramidal/cubic systems [8], while the corresponding spectra are shown in Figure 1.5b. Notably, the non-spherical geometries are characterized by shifts towards higher wavelengths of the maximum absorption as well as by the presence of multiple resonances, with respect to a spherical particle with the same volume. Instead, nanowires and nanorods are characterized by two discrete resonances, because of the oscillations of the electrons along the longitudinal and transversal axis. It is clearly noticeable that the splitting between these resonances increases as the aspect ratio of the rod rises (Figure 1.5c) [9].

1.3.1.3 LSPs in multiple particle systems

So far an isolated plasmonic system has been discussed. Indeed, this does not often applies in SERS spectroscopy, as since the first studies the strongest EM field enhancement has been proven to originate from particle dimers or trimers, revealing complex extinction spectra [10]. Thanks to near field microscopy hot-spots were localized within the inter-particle gaps [11] confirming that the special enhancement arises from near field inter-particle interactions. Since this discovery, the SERS substrate morphology was tuned in order to exploit the enhancement arising from hot-spots, therefore maximizing their spatial density. The LSPRs of an isolated particle can thus greatly vary in case of the interaction with another particle in close proximity. In fact, if the oscillating dipoles arising from close particles interact, new resonances are generated. This will eventually result in a consistent change in the charge distribution and EM field intensity and confinement, as well as in a shift of the resonance wavelength maximum.

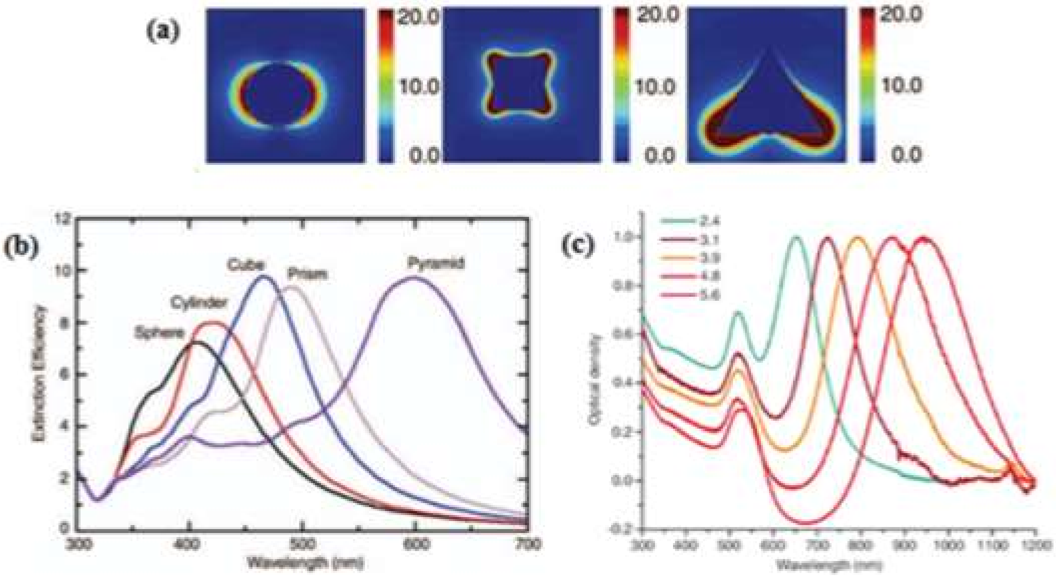

Figure 1.5 - LSPRs in non-spherical geometries: (a) $|E|^2$contours (E is the electric field) for sphere, cube and pyramid, plotted for wavelengths corresponding to the plasmon peak in Figure 1.5b; (b) Extinction efficiency of silver nanoparticles in vacuum having the shapes indicated in Figure 1.5a [8] **(c) Surface plasmon absorption spectra of gold nanorods of different aspect ratios, showing the sensitivity of the strong longitudinal band to the aspect ratios of the nanorods** [9]**.**

The plasmon hybridization model can be used to discuss the LSPRs in coupled nanoparticles. This model describes the plasmon modes of a complex nanostructure in terms of interactions between the plasmon resonances of its elementary components [12]. Considering a dimer of spherical particles excited with a polarized light along the interparticle axis, a split into the dipolar plasmonic modes of each nanoparticles occurs, similarly to the molecular orbital theory for a biatomic molecules: a low-energy bonding mode and a high-energy antibonding mode are thus generated (Figure 1.6a). A strong coupling to the far field as well as a large induced dipole are expected for the former mode, since it shows mutually aligned longitudinal dipoles, whereas an antialignment of the dipoles characterizes the higher energy mode. Due to the resulting absence of a net dipole moment, the antibonding mode is not able to couple to the far-field, being a so-called “dark” mode. A red shift of the resonance wavelength is therefore observed as a consequence of the different coupling of the two modes with respect to the incident light. Due to the increased complexity of multiple particle systems, a quantitative evaluation of the plasmonic properties change caused by a modification of the morphological characteristics is hard to obtain from the hybridization model, but general trends can be predicted.

In analogy to the case of LSPs in single nanoparticles, hot spots can be resonantly excited. Different electric field distributions around the particles can be revealed depending on the plasmonic modes excited by the incident wavelength. Figure 1.6b shows the calculation of the EM near field for a dimer of silica particles coated with a thin layer of Ag, excited with two different wavelengths [13]. A huge EM fields, localized in nanometric regions, is obtained due to the confinement of the radiation in a coupled plasmonic system.

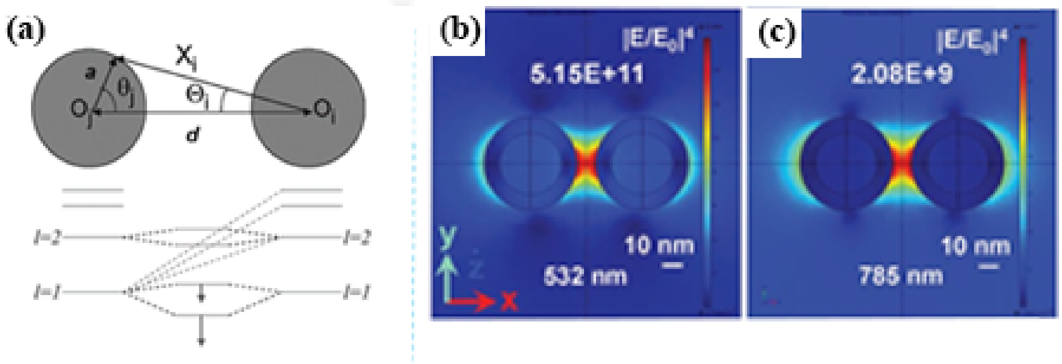

Figure 1.6 – a) Scheme of plasmon modes in a dimer as described by plasmon hybridization model. b-c) Calculated SERS enhancement distributions for silica nanoparticles (30 nm) with a thin silver layer (5 nm) at two excitation wavelength (532 nm and 785 nm) [13]**.**

As a consequence, the highest SERS enhancement can be attained for the smallest inter-particle distances [14]. The influence of the hot-spot geometrical parameters onto the SERS enhancement is shown in Figure 1.7. A decrease of the inter-particle gap, combined with an increase of the particle size, leads to an increment of the EM SERS effect by orders of magnitude, particularly concerning very small gap between NPs. Experimental proofs of such theoretical calculations have been provided by constantly varying the gap between dimers fabricated by lithographic technique [15] or by the assembly of core/shell SiO_2-silver nanocubes dimers with different thickness of the silica coating [16].

Finally, recent studies demonstrated that Raman scattering enhancement can include the contribution from dark plasmons, even though they cannot directly interact with light [17]. Even though the far-field optical response of a SERS substrate can be a useful tool to determine its plasmonic characteristics, the SERS response could show some deviations due to such non-radiative near-fields modes.

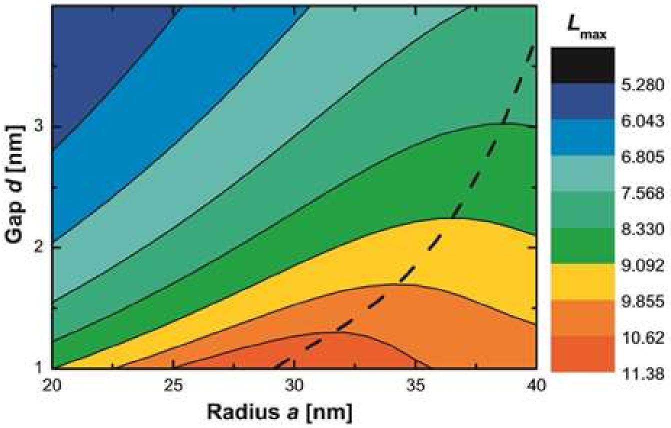

Figure 1.7 - Maximum SERS effect (F_{max}) on the surface in the gap of a dimer as function of geometrical parameters (radius and gap). $L = \log_{10}(F_{max})$ [14].

1.1.2 Chemical enhancement

The chemical mechanism of SERS enhancement generally refers to the contributions that are not related to the EM environment. Usually they are associated with an electron transfers between the metal surface and adsorbed molecules, and evidence of their presence is usually provided by the shift of the frequencies and the change in relative intensity of the vibrational modes of the adsorbed molecules [18]. Nevertheless, studies have demonstrated that not every adsorbed molecule experiences a chemical enhancement: such results corroborate the hypothesis of active sites at atomic scale in which the molecules can interact with the metal [19,20]. The chemical contribution is thus challenging to be described with a unified expression, and several models have been developed [20]. A first mechanism, called static charge transfer, takes into account a change in the polarizability in the metal-molecules complex. This can arise from the perturbation of the electron cloud of the adsorbed molecule interacting with the metal or from an electron transfer in the ground state, leading to an increased Raman cross section of the complex. [18,20]. Valley et al. [21] studied the static chemical enhancement for a set of differently substituted benzenethiols adsorbed on gold and silver substrates. Since the only differences were related to the substituents, the variation into the enhancement was entirely due to the chemical mechanism. Such enhancement was measured experimentally and calculated by means of time-dependant density functional theory (TDDFT). Results from both protocols showed a modest chemical enhancement, ranging from 1 to 100, but interestingly the theoretical calculations were in accordance with the experimental results only when a ligand-to-metal charge transfer from the highest occupied molecular orbital

(HOMO) to the metal lowest unoccupied molecular orbital (LUMO) was taken into account.

Another mechanism foresees the generation of new electronic states, due to charge transfer processes, enabling new resonances. Kneipp carried out a study using a set of polymethyne dyes on silver nanoparticles, in which the variation in the enhancement, which was of about one order of magnitude, was correlated to the ability of the specific dye to generate radicals. This result confirmed the charge transfer mechanism between the metal and the adsorbed molecules [20].

However, an accurate description of the chemical enhancement remains challenging, due to the overlapping of several resonant and non-resonant mechanisms, and moreover to the presence of the much larger enhancement due to the plasmonic resonance.

Chapter 2

2 SERS substrates

2.1 Introduction

In the previous chapter, basic concepts of plasmonics and SERS spectroscopy have been introduced. These fundamental notions are needed for the discussion about the development of an optimized SERS substrate. High density of the hot-spot and at least a plasmonic resonance that could match the excitation wavelength are indeed required. Additionally, other factors have to be considered for a real application. Good SERS substrates should in fact provide good reproducibility and uniformity, showing both low inter- and intra-substrate variability, together with low cost and an easy fabrication [22]. Moreover, in case of biological applications, the stability of the substrates plays a key role in order to prevent morphological modifications by potentially aggressive environments.

This chapter presents an overview of the main synthesis techniques of SERS substrates. Finally, the last section will briefly discuss the biological application of such substrates.

2.2 SERS substrates

The fabricated SERS substrates commonly belong to two main categories: solution-based systems (wet systems), which are usually colloidal solution of plasmonic nanoparticles, and solid systems, which can apply both to substrates produced by bottom up (for example the in situ growth of NPs) and top down techniques, such as nanolithography. Substrates produced by wet methods are usually easy to synthetize and display huge SERS enhancement, however some issues related to the reproducibility and to the stability of the colloids exist. On the contrary, solid substrates show very low spatial variability achieving very good SERS stability. Nevertheless, especially concerning nanolithographic techniques the main drawback is related to the high costs and complexity of the fabrication.

2.2.1 Colloidal systems

Colloidal substrates are suspensions of plasmonic nanoparticles usually produced by wet chemistry in which the nanoparticles are synthetized starting from a soluble metal salt precursor that is reduced to the zero-valent metallic element by a reducing agent, resulting in the precipitation of the particles. The NPs synthesis usually takes place in supersaturated conditions in which nuclei are generated, starting then to grow in clusters eventually leading to the formation of nanocrystals with increasingly larger size [23]. These clusters can usually assume different shapes driving the formation of different crystals: typically they may take a single-crystal, singly twinned or multiply twinned structure, each one being the precursor of different particle shapes [23].

The most widespread method to fabricate silver colloids is the Lee and Meisel synthesis, in which sodium citrate is exploited to reduce silver nitrate [24]. Citrate also plays the role of a stabilizing agent thanks to the formation of a negatively charged layer adsorbed onto the particles surface, which prevents them to aggregate due to the repulsion between the crystals. Other typical reducing agents are $NaBH_4$ and hydroxylamine. However, nanoparticles synthetized in such ways show a quite wide size distributions and mostly spherical geometries. To address this issue a two-step method have been developed, separating the nucleation and the growth phase [25]. This could be accomplished by first producing the metal seeds and afterwards adding them to a growth solution or through a fine tuning of the synthesis condition, such as temperature, reagent concentration and in particular the presence of additives [26]. Furthermore, to better control the final shape of the nanoparticle, a capping agent can be used to selectively adsorb onto a specific crystal facet, leading to the production of nanoparticles with a defined geometry [27]. This is the case of the polyol synthesis, particularly used in the preparation of silver NPs, which exploits the presence of a reducing agent and a capping agent, such as poly-vinyl pirrolidone (PVP) [28]. Finally, it is also reported in literature that different geometries of NPs can be obtained by merely varying the temperature, the salt precursor and its concentration [29].

Despite the wide range of obtainable shapes, most of the colloidal substrates do not show a huge SERS enhancement in a well-dispersed form, with the only exception of those composed by NPs rich in sharp edges and corners, like nanostars, nanodendrites and nanorods [30]. However such structures are usually achieved using non-conventional reactants, as for example protoporphyrin IX [30]. In order to boost the SERS efficiency, colloids have to be aggregated in clusters to exploit the formation of hot-spots: this is usually obtained by the addition of salts, such as NaCl, $MgSO_4$ or $NaNO_3$, whose metallic cations can act as a counter ion for the negatively charged particle surface, screening them and reducing the repulsion between nanoparticles [31,32].

Colloidal suspensions are mainly used as SERS substrates due to their good enhancement and versatility, but their lack in reproducibility and stability over time raises some concerns about the consistency of the results [33]. In recent years some effort has been made in order to address these issues developing new strategies for the controlled aggregation of colloids, through the functionalization of the surface with different linkers, such as DNA strands or thiols (Cysteamine [34]), or by simply varying the storage conditions to avoid the coagulation of the particles.

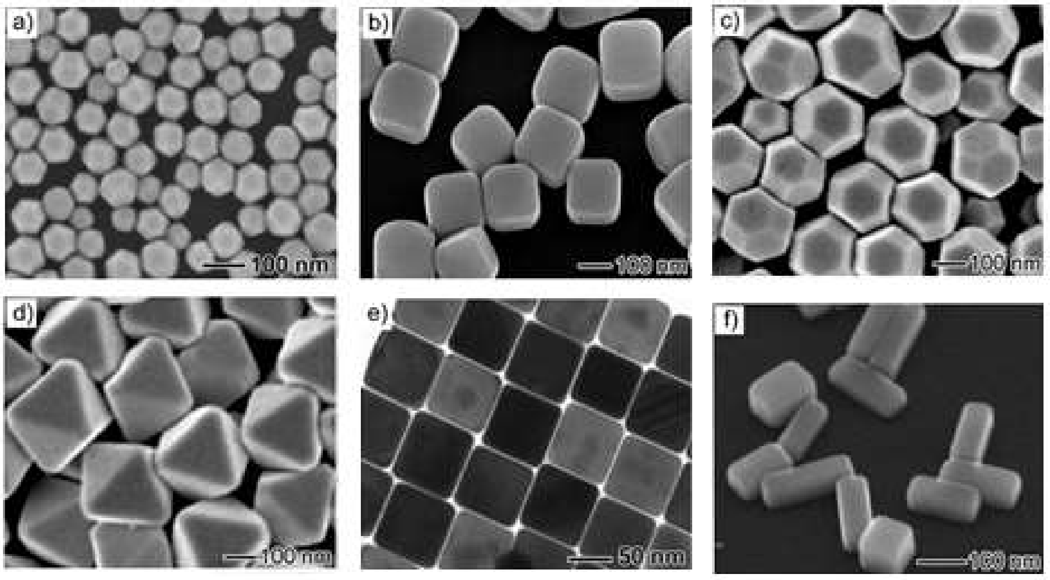

Figure 2.1 - Electron microscopy images of single-crystal Ag nanoparticles: a) cuboctahedrons prepared in ethylene glycol with PVP as a capping agent; b) nanocubes prepared in ethylene glycol with PVP as a capping agent; c) truncated octahedrons prepared in 1,5-pentanediol in the presence of PVP and Cu^{2+} ions; d) octahedrons prepared in 1,5- pentanediol in the presence of PVP and Cu^{2+} ions; e) nanocubes prepared by a modified silver mirror reaction in the presence of Br^- with glucose as a reducing agent; f) nanobars prepared in ethylene glycol in the presence of PVP and Br^-. [23]

2.2.2 Solid systems

The second typology of SERS substrates in literature consists in solid platforms, which are usually exploited due to their high reproducibility. At present, a large variety of techniques is available for the synthesis of such platforms, but they are usually divided in three main categories: nanolithographic techniques, template-based techniques and nanoparticles immobilized on a substrate [35].

Among these methods, nanolithography is well known to provide nanomaterials with a highly reproducible morphology, allowing to achieve a fine control on the produced structures [36]. The most widespread nanolithograpic technique is indeed Electron Beam Lithography (EBL) by means of which it is possible to produce nanostructures with specific shapes, size and inter-particle gap [35]. A polymeric resist, that can be positive or negative, is at first casted on a substrate allowing to protect it from the successive modifications, and then exposed to an electron beam. The resist, often polymethylmetacrilate (PMMA), is then developed and subsequently the pattern is transferred on the substrates. This last step, concerning the metal deposition, can follow two pathways: in the first case the metal can be directly deposited on the obtained structure, followed by the removal of the mask, or, as second option, Reactive Ion Etching (RIE) can be performed before lifting off the mask and depositing the metal obtaining a 3D structured substrate. Both techniques can be exploited to produce nanostructured substrates with geometric features below 10 nm [37]. Similar techniques involving the patterning of a resist can exploit UV-laser irradiation or Focused Ion Beam (FIB). Even though such approaches are cheaper, the resolution is lower with respect to the EBL.

The development of these techniques guarantees the production of nanoarrays with finely-tuned inter-particle spacing [38] and gap geometry [15], allowing to study their effect on the SERS enhancement [15,38,39].

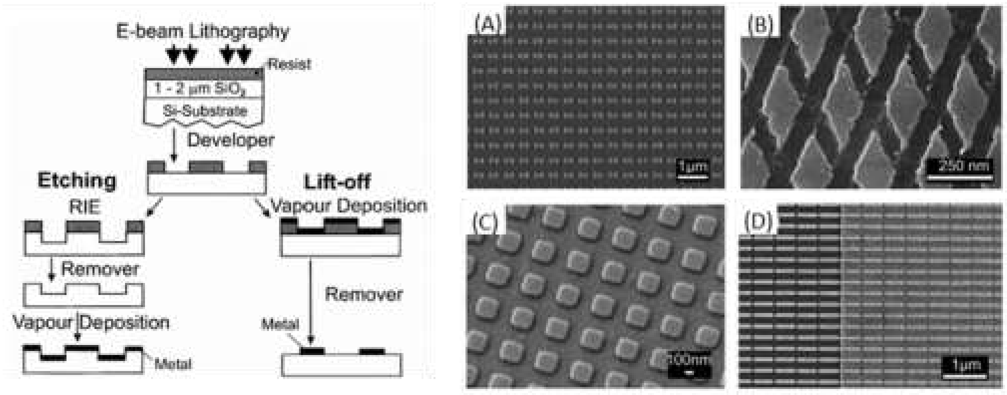

(a) **(b)**

Figure 2.2 - a) Schemes of etching and lift-off methods of substrate fabrication by e-beam lithography on oxidised silicon substrates. [40] **(b) Examples of plasmonic nanostructures obtained by EBL: (A) Bowtie nanoantennas; (B) gold nanorhombs produced by means of EBL and RIE; (C) silver nanosquares; (D) SEIRA nanostructures fabricated by lift-off EBL** [37]**.**

A different and cheaper approach to fabricate structured systems exploits a template with a defined geometry in which the metal is deposited. Nanosphere lithography (NSL) and Anodic Alumina Oxide (AAO) techniques belong to this category. The former method employs a bi-dimensional self-assembled monolayer of colloidal nanoparticles as template for the following metal deposition. Depending on the use of different deposition technique and on the thickness of the metal layer three different structures can be obtained [41], as shown in Figure 2.3. Metal films with a spherical geometry (M-FON) are prepared through physical vapour deposition [41]. If the polymeric nanoparticles are removed, triangular-shaped nanostructures are left in correspondence of the interstices between the spheres. Finally, regular arrays of segmented spheres voids (SSV) displaying a hexagonal geometry can be obtained by electrodeposition of the metal followed by the lift-off of the nanosphere monolayer [41].

Multi-layered masks or the variation of the deposition angle can be exploited to further control the nanoparticle structure tuning. These approaches allow to finely control the geometric properties, such as inter-particle gap and size distribution, fabricating nanostructures with dimensions ranging from 20 nm to 1000 nm. Such characteristic has been exploited to study the size-dependent plasmonic properties of the silver nanoparticles [42].

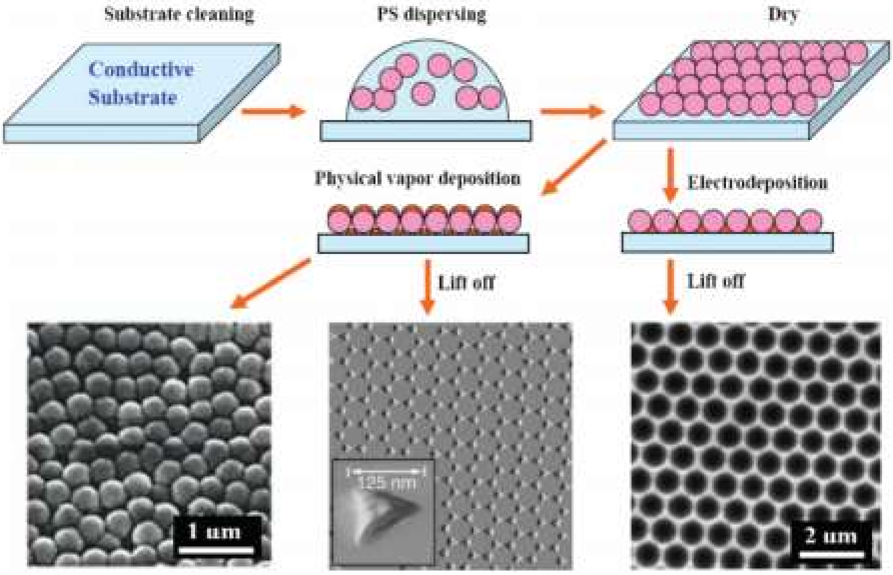

Figure 2.3 – S Schematic diagram of template methods using nanosphere lithography to fabricate ordered nanostructured SERS-active substrates. From left to right: metal films over nanospheres (M-FON), nanoprisms array, segment sphere voids (SSV) array [41].

For the case of AAO, the templates are produced by means of electrochemical etching of alumina in acid conditions displaying a tight pore distribution with diameters ranging from 10 nm to 400 nm [43]. The metal can then be deposited into the pores thanks to electroplating or vapour deposition techniques. Nano-wire or nanotubes arrays are finally obtained by partially dissolving the templates with phosphoric acids (Figure 2.4) [44]. Despite the simplicity and low cost of the process, which allows a fine tuning of the morphological features of the final nanostructures, some issues concerning the spacing between nanowire remains, which can be hardly obtained with a size lower than 5 nm.

A totally different approach focuses on the development of colloidal-based systems. As stated in the previous section the main drawbacks concerning such substrates is due to their poor reproducibility and stability. In order to overcome this issue, different strategies have been developed, such as, among the other, the immobilization of the

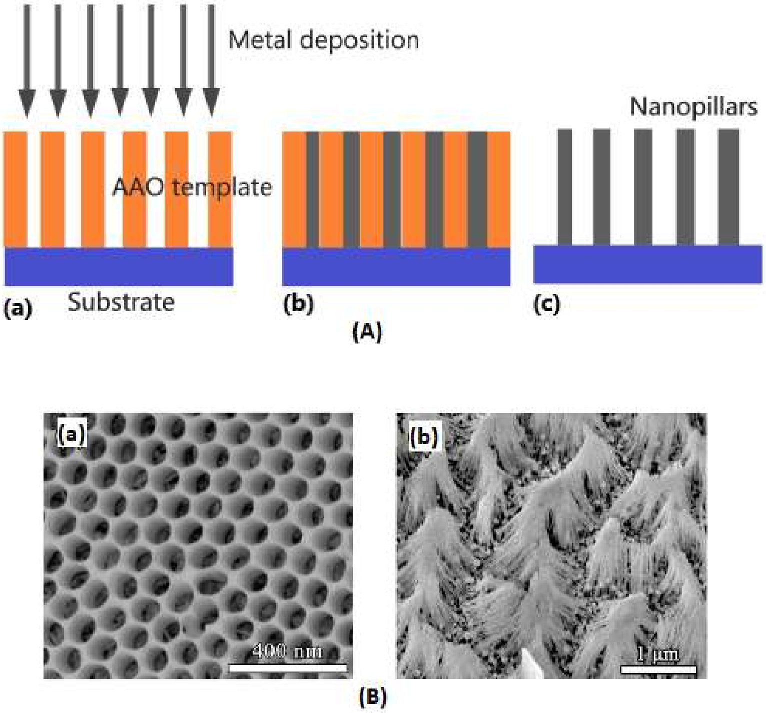

Figure 2.4 - Figure (A). Scheme of AAO template-based procedure for nanopillars fabrication: metal deposition by electroplating or vapor deposition (a-b), AAO template electrochemical etching (c). Figure (B). SEM images: AAO template (a) and bundles of nanowires (b) [43].

nanoparticles on the surface of a solid substrate. This can be achieved following two different methods involving chemical or electrostatic mechanisms.

Concerning the chemical approach, the NPs are bonded to the substrates using bi-functional ligands. At first, the employed molecules are anchored to the surface, exploiting one of the functional groups, while the second one (i.e. thiol or amine group) is left exposed to bind the metal NPs. Concurrently, the spacing between the nanoparticles can be tuned using linkers with different length. Even ordered 3D structures can be produced by means of this approach, adding successive layers and providing higher SERS enhancement with respect to the 2D platforms. In the second approach, an electrostatic interaction between the metal NPs and polymers [45] or biomolecules is exploited, such as for negative DNA networks that can be employed to adsorb CTAB capped silver nanoparticles that are positively charged, achieving ordered SERS substrates [46]. Capillary forces can also be exploited to drive the formation of a self-assembled monolayer of NPs contained in a droplet, after being capped with a surfactant to prevent their aggregation [47].

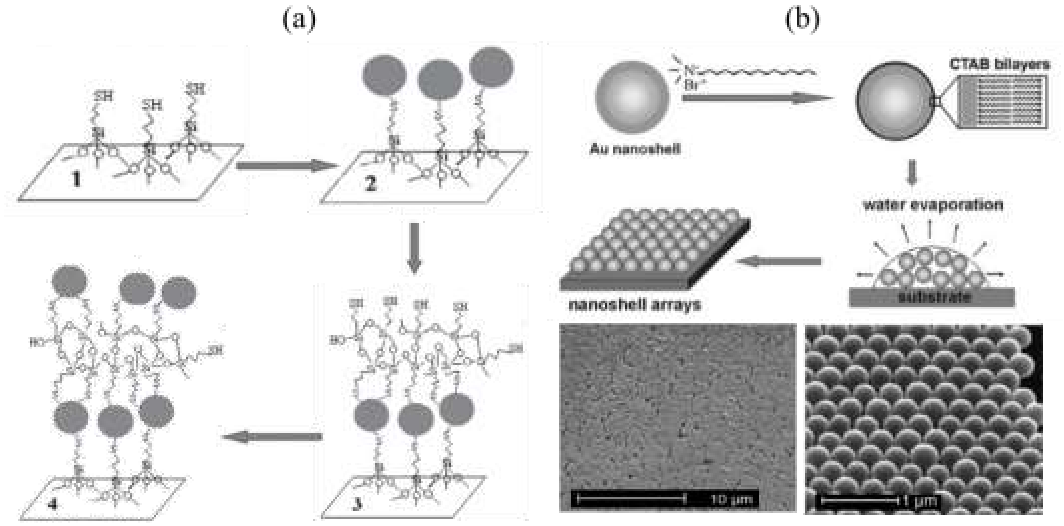

Figure 2.5 - a) Fabrication of SERS substrates. Step 1: The surface of a clean glass slide is modified with MPTMS to expose thiol groups; Step 2: The modified glass slide is immersed in a solution of Ag NPs (grey circles), which will adhere to the surface by interacting with the thiol groups; Step 3: The slide is dipped in a sol–gel of MPTMS to add more thiol functionalities to the surface; Step 4: The substrate is immersed again in a solution of Ag NPs to receive an additional layer of Ag NPs[48] **(b) Fabrication of Au nanoshell arrays fabricated using CTAB as capping agent and SEM images of the array deposited on a silicon substrate** [47]**.**

Finally, the direct growth of the nanoparticles on a solid substrate, in which the metallic seeds are previously anchored to a surface and then enlarged, has also been exploited. Furthermore, the NPs can be produced by adding a reducing agent to a metal precursor solution [49,50] or exploiting the intrinsic reactivity of a surface.

Porous silicon based SERS substrates are produced thanks to this last method, in which the reducing properties of the surface are exploited to synthetize gold, silver, and copper nanoparticles [51]. Especially porous silicon substrates decorated with silver nanoparticles have been proven to be highly efficient, easy to prepare, and versatile. The potentiality and the characteristics of such substrates, which represent the starting point of this thesis, are presented in the next section.

2.2.3 Porous silicon SERS substrates

Discovered for the first time in 1956 by Ulhir et al [52], porous silicon has been exploited in numerous field of application thanks to its chemical, optical, electrical, and morphological properties. Over the years different techniques have been developed for porous silicon manufacturing, but among these, the electrochemical etching of a doped silicon wafers in HF solution is the most widely employed. This anodization is usually carried out in a HF resistant cell (i.e. Teflon), in which a portion of the Si wafer is exposed to the electrolyte. A constant current density is then applied between the silicon itself, which plays the role of the working electrode, and the counter electrode, which consists in a platinum foil, driving the electrochemical reaction at the silicon/electrolyte interface.

The proposed mechanism involves two steps [53]:

$$Si + 2F^- + 2h^+ \rightarrow [SiF_2]$$

$$SiF_2 + 4F^- + 2H^+ \rightarrow SiF_6^{2-} + H_2$$

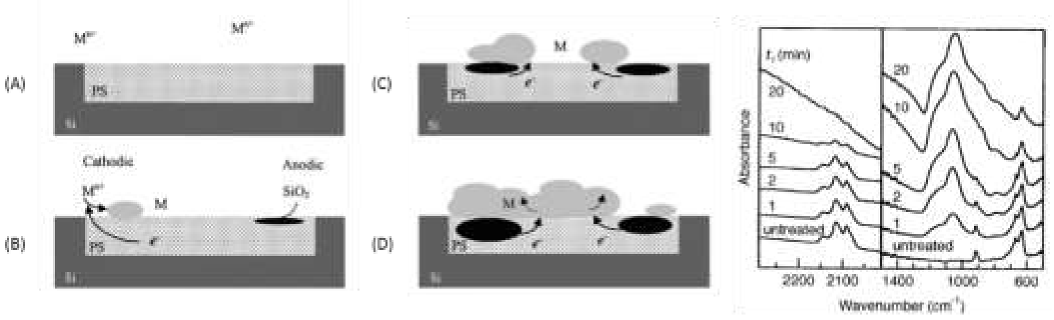

(a) **(b)**

Figure 2.6 - (a) Schematic representation of the mechanism of metal deposition onto pSi substrate during the immersion plating.[51] **(b) Transmission FTIR spectra for untreated pSi and pSi after immersion in 10^{-2} M $CuCl_2$. t_i denotes the immersion time.** [54].

In the first step, the holes present in the Si valence band are attracted towards the surface, causing the Si oxidation to Si (II) state and forming SiF_2. Subsequently, SiF_2 further react with the water protons leading to the further oxidation of Si to its (IV) state[53]. The electrochemical etching causes the formation of a porous layer, where the pores preferentially grow along the <100> direction of the wafers. Different pore morphologies can be achieved depending on the reaction conditions and on the initial doping of the wafers, as reported in the literature [55]. Moreover, the final porosity and thickness of the porous layer can be customized modifying the electrochemical etching conditions [56].

As a consequence of the etching in HF solution, the surface chemistry of fresh pSi is dominated by the presence of silicon hydride species, where Si can be bonded up to three hydrogen atoms (SiH_x, x=1, 2, 3). These species are responsible for the unique reactivity displayed by such substrates, especially concerning the spontaneous surface deposition of noble metals through the reduction to the metallic state of a salt precursor [54]. Such method, called immersion plating, was first explained by Ogata et al, according to the following reaction, in which the metallic deposition is driven by the oxidation of the superficial SiH_x species [51].

$$SiH_{surf} + 2H_2O + (4+x)AgNO_3 \rightarrow SiO_2 + (4+x)HNO_3 + (4+x)Ag$$

Figure 2.6 (a)A, B illustrates the deposition of the first highly reactive nuclei. These isolated nuclei, according to a local cell mechanism [57] can act as local cathodes where the Ag^+ cations are reduced, thanks to the electrons provided by the oxidation of the porous silicon (Figure 2.6(a)B, C). Under certain conditions the produced NPs can aggregate to form a metallic film on the silicon surface (Figure 2.6(a)D). A further proof of the proposed reaction mechanism is obtained by the FT-IR transmission spectra, shown in Figure 2.6b, that highlight the reduction of the SiH_x stretching related band at 2100 cm^{-1} as an increasingly stronger Si-O-Si band appears at 1100 cm^{-1}.

From a SERS point of view, the production of silver NPs is by far the most interesting, due to the higher enhancement provided. The first study demonstrating the fabrication of a silver-coated pSi substrates has been developed by Chan et al, in 2003 [58]. After just one year, Sailor et al. reported the production of SERS substrates consisting in silver plated pSi. Since then, such protocol has become one of the most widespread methods of fabrication for porous silicon SERS substrates [59]. Figure 2.7 shows the wide range of nanostructures that can be obtained by immersion plating thanks to the large variety of parameters that can be modified. Characteristic such as pore morphology, thickness, reaction parameters and silicon doping greatly affect the NPs morphology.

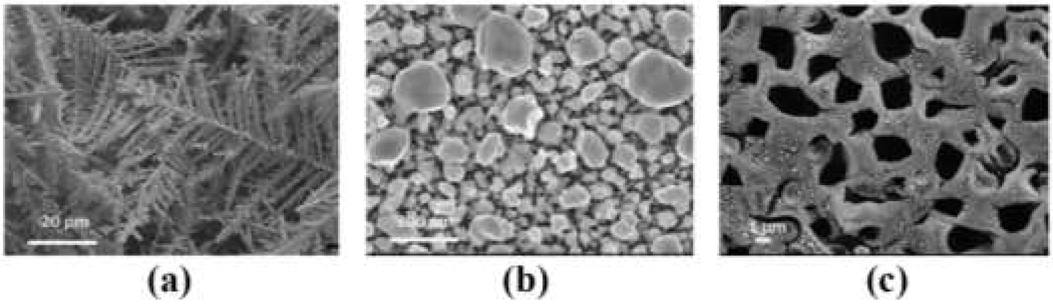

Figure 2.7 - SEM images of pSi coated with silver nanoparticles. Several morphologies can be attained: (a) Ag-dendrites [60], **(b) highly packed small Ag NPs** [61] **and (c) Ag NPs grown on a porous silicon template** [62].

In particular, the optimization of the Ag-coated pSi substrates was carried on in recent years, analysing the effects of variables, such as temperature, silver precursor concentration, dipping time and the addition of a capping agent, on the final morphology of the silver NPs [63]. It was noticed that the reaction outcome is mainly influenced by temperature and $AgNO_3$ concentration, leading to the production of bigger NPs in a shorter time. On the contrary, if the concentration is fixed, longer dipping times will result in bigger particles. Nevertheless, this approach has a major drawback because longer dipping times result in higher polydispersity, due the nucleation of several NPs families [57].

Concerning the SERS efficiency of such substrates, the detection of different dyes, such as Cyanine 3 and Rhodamine 6G in single molecule regime has been reported [62,63]. The reproducibility of the SERS signal was also taken into account, as Bandarenka et al [64] reported an intra-substrate standard deviation of 20%. Such value could be due to a poorly uniform distribution of the dopant within the silicon wafers. Once addressed this issue the RSD was reduced to 7%.

2.2.4 Dynamic flow synthesis

In the previous sections the synthesis of a wide range of nanomaterials through different techniques has been presented and discussed. However, especially concerning the fabrication of colloidal substrates, batch synthesis suffers from several disadvantages, due to the poor inter and intra-batch reproducibility. To break down such difficulties a microfluidic approach has been recently taken into account for the fabrication of the desired substrates. Continuous flow microreactors, integrated with heaters and fluid control systems have been developed, achieving a better control over a wide range of synthesis parameters, such as temperature and residence time, as well as enhancing heat and mass transfer due to higher surface-to-area ratio with respect to the macroscopic scale [65].

A microreactor is a vessel, in which a chemical reaction takes place, designed to optimize the reaction performance and achieving higher yields towards the targeted outcome [66]. The most widespread material for the manufacture of such microreactors is polydimethylsyloxane (PDMS), thanks to its low cost and ease of fabrication. However, some drawbacks due to the limits of operating at high temperature and pressure as well as using organic solvents, restrict its usability range.[66,67]

The flow synthesis methods can be classified in different categories depending on the geometry and the size of the designed reactors [68]. At first, these methods can be divided into chip-based or tubular-based systems, while a second classification further divides them into millifluidic, microfluidic, and nanofluidic devices. Finally a single or multiple phase flow can be exploited (Figure 2.8) [33]. The single-phase approach focuses on the fluid properties and the flow conditions, whereas for the multiple-phase approach the synthesis parameters depend also on the channels reactor geometry (T-junction, flow-focusing, and co-flowing [65]). This latter protocol offers several advantages thanks to the reduction of the mass transfer limitations, increasing the mixing efficiency and the interfacial area, as well as reducing the transfer distance [69].

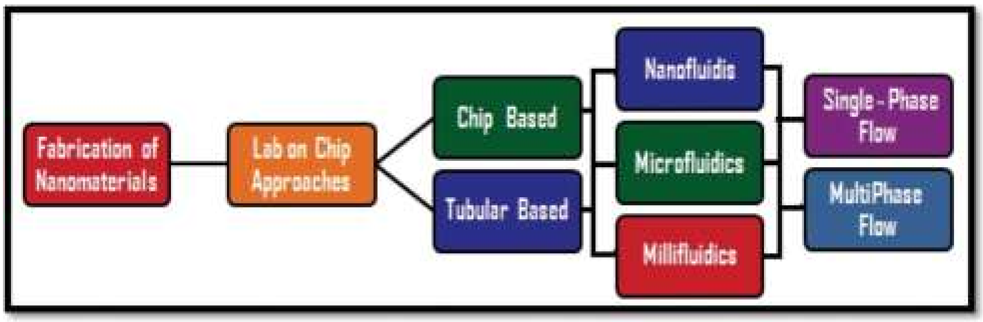

Figure 2.8 – Different methods for the flow synthesis of nanomaterial [33].

In recent years, metallic NPs have attracted major interest thanks to their optical properties: particularly in plasmonic field silver and gold particles are widely used. In this framework, the microfluidic approach could allow the synthesis of NPs with finely tuned morphological properties, achieving the desired plasmonic properties.

As extensively reported in literature microfluidic single-phase reactors have been exploited to tune the size and the shape of colloidal NPs by varying the reactants concentrations, the temperature, and the solution flow rate [33,70–73]. Usually the easiest way to produce a colloidal SERS-active substrate is via chemical reduction of a metallic salt precursor and therefore is the most widespread approach [74].

Lawastiend et al. [72] developed a two-steps on-chip dynamic synthesis protocol taking advantage of the production of AgCl sacrificial templates starting from a silver diamino precursor ($Ag(NH_3)_2^+$). These templates were then further reduced to the zero valent Ag using different reducing agent, retaining the original morphology of the AgCl templates. The results show that the geometry of the chlorinated templates can be defined by simply tuning the concentrations of the reactants, achieving a wide range of morphology. Moreover, once fixed the reactant concentrations, the increment of the flow velocity, led to an increased nucleation rate, resulting in the rapid formation of more nuclei, and consequently to the production of smaller particles. Finally, the SERS efficiency of each particle morphology was tested. The results show a correlation between the increased SERS signal and the geometries, displaying sharp edges and corners.

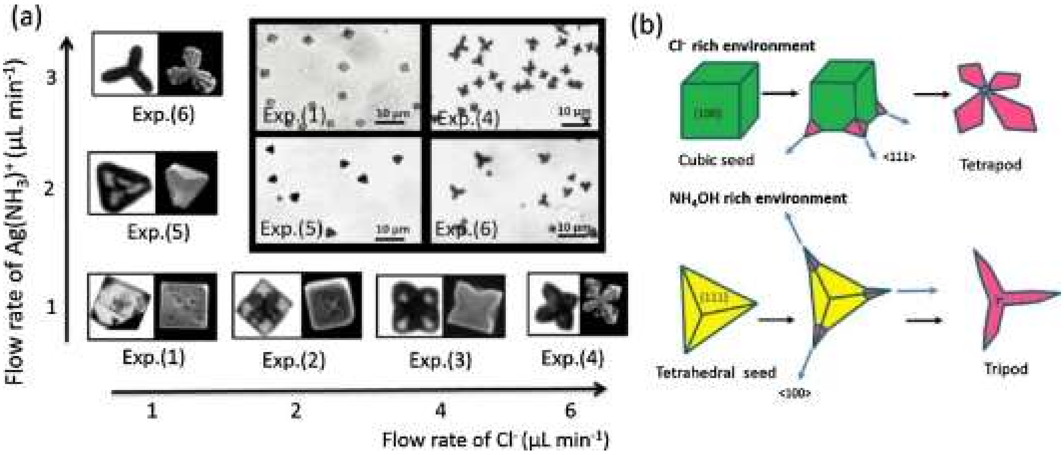

Figure 2.9 - Microscope and SEM images of AgCl microstructures transforming from cubic (Exp. (1)) to tetrapod (Exp. (4)) when increasing flow rate of Cl^- and from cubic (Exp. (1)) to tetrahedron (Exp. (5)) and to tripod (Exp. (6)) when increasing flow rate of $Ag(NH_3)_2^+$. (b) The proposed AgCl growth mechanisms in Cl^- rich and NH_4OH rich environments [72].

The effect of the temperature was also studied, combined with the flow rate and the precursor concentration variation [73]. The results show that an increased synthesis temperature leads to the production of bigger particles. Moreover, it has been found that a too high flow rate not only causes the formation of smaller particles but can even hinder the formation of the nuclei themselves.

The *in-situ* fabrication of plasmonic nanostructures has been extensively studied in literature [74–77]. Hereby, a simple study of polyol-based synthesis of a silver patterned surface developed by Leem et al is reported [76]. In this protocol ethylene glycol was employed as a solvent as well as the reducing agent, and the crystalline structure of the NPs was tuned adding PVP to the silver nitrate precursor solution. A thin film of Ag NPs is obtained along the channel walls of the device, that is composed by a PDMS channel attached on a silicon wafer. (Figure 2.10a). Moreover, different samples were prepared varying the duration of the synthesis, resulting in the production of bigger Ag NPs as the reaction time increased (Figure 2.10b). Finally, the SERS efficiency of the nanostructures was evaluated. Thanks to the particular design of the microfluidic platform, real-time measurements were performed injecting different solutions of adenosine in a concentration range between 5 mM and 500 nM (Figure 2.10c). It is clearly noticeable that the SERS signal decreases as the adenosine concentration is lowered.

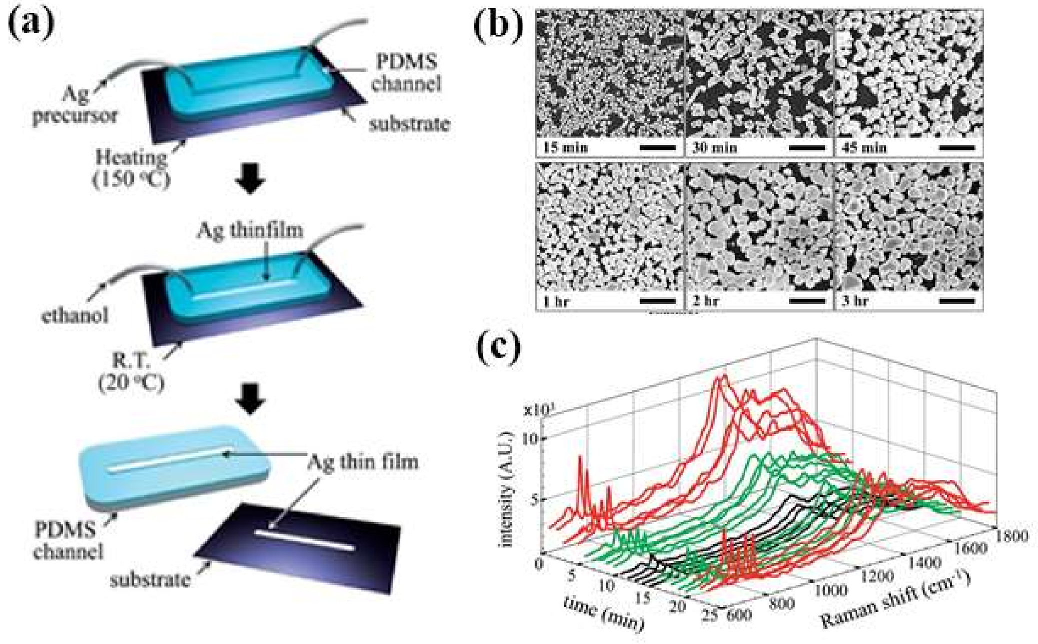

Figure 2.10 – a) Schematic diagram of the microfluidic synthesis of Ag coatings in the channel. (b) SEM images showing the variation in the morphologies of the Ag thin films with fabrication durations of 15 min, 30 min, 45 min, 1 h, 2 h, and 3 h. The scale bar is 2 mm (c) Raman spectra of adenosine obtained in situ: 5 mM, 50 µM, 500 nM, 50 µM, and 5 mM [76].

Even though the *in situ* synthesis of metallic NPs can open to new applications thank to the easier integration in a sensing system or to the chance to perform on-site and real-time measurements, it yet has to deal with few challenges, such as the weak analyte-particle interaction and the cross-contamination [74]. Especially concerning the development of strategies to overcome this last issue a multiple phase approaches with segmented flow have been exploited [68,78,79]. Such segments can be easily formed merging two immiscible liquids, allowing a precise control over their characteristics through the variations of the fluidic pressure [78]. Droplet-based microfluidic chip are the most widely used segmented flow microfluidic devices [74]. The so generated droplet can be considered as an isolated reaction site confined in a small volume [80], therefore limiting the cross contamination. Moreover, the strong convective flow inside the droplet allows an enhanced mixing between the analyte and the NPs. One of the major drawback, though, is related to the complexity of the microplatform architecture, that involves multiple injectors to generate the droplets and to introduce the analyte in the microchannel [74].

Once achieved a fine control over the NPs shape and distribution, the focus has was directed towards the improvement of substrates SERS efficiency [74]. Inside a microfluidic channel the interactions between the target analyte and the colloidal nanoparticles are driven by diffusion processes, often resulting in a high signal variability [74]. To address such issue, a first concentration step is often required to raise the amount of analyte-target duplex.

Yadzi et al proposed an approach based on a 3D nanofluidic network packed with nanoporous silica microspheres (Figure 2.11a), for the detection of DNA sequences. This protocol exploits a sandwich hybridization between the target DNA strand and a complementary probe immobilized on the silica nanosphere beads. More in detail, the assay foresees a previous hybridization of the probe with a Raman labelled DNA strand. However, this is designed to bind the probe with a lower affinity compared to the target DNA sequence. Once the analyte flows into the chip, the Raman label is displaced (Figure 2.11b) and proceed downstream the microfluidic channel where it is adsorbed on colloidal Ag NPs. The final section of the 3D network (SERS detection zone) is once again constituted by a silica nanosphere layer, allowing to trap the DNA-NPs aggregate, and therefore greatly improving the SERS performances if compared with an open microfluidic channel. Furthermore, this assay allowed the multiplex detection of different analyte as proved by the simultaneous and yet selective detection of tetramethyl rhodamine (TAMRA) and Rhodamine 6G [81].

In this framework the formation of hot-spots through the aggregation of colloidal nanoparticles is essential to further improve the SERS detection. To this aim Zhou et al proposed an interesting approach: a PDMS microfluidic chip with a pneumatic valve positioned at the end of the microchannel was designed (Figure 2.11c). The opening and the closing of the valve regulates the trapping of the Au nanoparticles while the solvent can flow through. To perform a reliable measurement, 10-15 minutes are required to complete the aggregate formation. As the pressure is released the valve open and the aggregates can be flushed away [82].

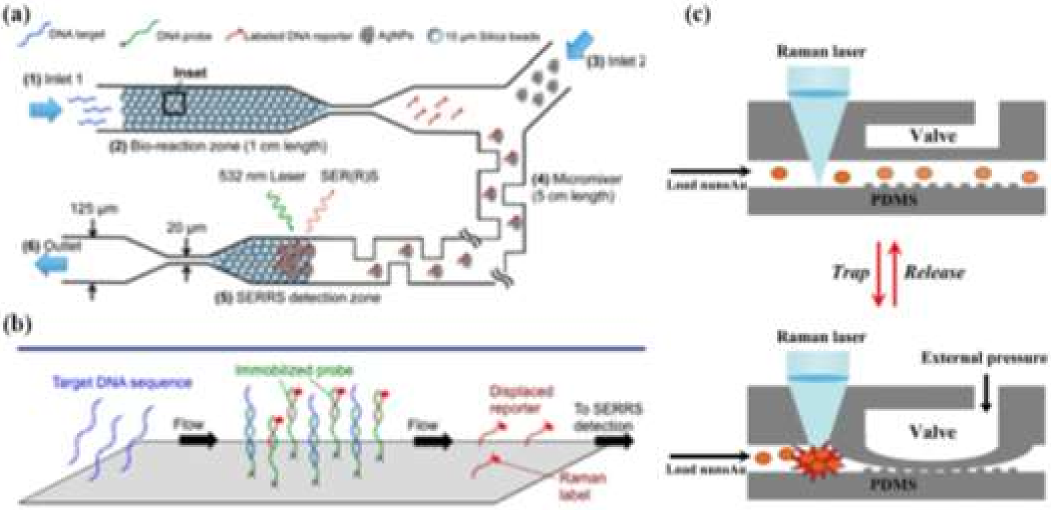

Figure 2.11 - a) Microfluidic SERRS microsystem with integrated competitive displacement for DNA sequence detection. b) Competitive displacement assay concept [81]**. c) Schematics of the trapping and releasing of gold nanoparticles using a pneumatic microvalve for SERS detection** [82]

Particularly concerning the fabrication of SERS substrates, the microfluidic approach could be exploited to overcome the poor inter and intra-substrates reproducibility, mostly related to the colloidal systems, achieving the fabrication of NPs with finely-tuned size and geometries.

2.3 SERS substrates for biosensing application

In recent years SERS spectroscopy has attracted significant interest in the investigation of biological samples. Thanks to its non-destructive and ultra-sensitive features, it has gradually emerged as one of the prominent approaches among the vibrational spectroscopies to investigate a wide spectrum of biological environments, ranging from biomolecules such as proteins, DNA, and RNA [83–86], to bacteria [87–91] and viruses [92–94].

Generally speaking, two major approaches are usually employed for SERS bioapplications, namely the label-free protocols and the indirect protocols using specific probes conjugated with a Raman reporters [95]. In the former approach the target analyte is directly adsorbed on the substrate surface without requiring a functionalization step. Indeed, the unique SERS vibrational pattern arising from the direct interaction of the target with the surface can be exploited for a selective detection [96]. This represents the simplest approach in the SERS-based biosensing area. Nevertheless, it has to deal with some issues concerning the interference that may arise from the competitive adsorption of other molecules. The detection efficiency could thus be reduced, and moreover the vibrational pattern of the interfering molecules could overlap with the target fingerprint, making the data difficult to analyse [97]. For these reasons, the label-free approach is usually less suitable for the detection of analytes in a complex matrix. On the other hand, the use of specific probes can greatly improve the selectivity and the resilience of an assay [98]. Moreover, Raman reporters, molecules with a strong Raman fingerprint, can be conjugated to the probe or the target to boost the sensitivity. In this last scenario, a potentially complicated chemical step is required [95].

In the following section, the employment of SERS spectroscopy for different bio-sensing applications will be reviewed.

2.3.1 Proteins detection

Proteins are complex biomolecules made of linear chains of amino acids, folded into various 3D supramolecular structures. The label-free detection of such structures can be very important, since specific peptides are often involved in cancer diseases or neurodegenerative pathologies [99]. However, the majority of the proteins displays a lower Raman cross section, if compared to other components of the biomolecules, thus resulting in a weaker SERS signal that can easily be overwhelmed by the vibrational features of interfering species [22,97]. A purification step is therefore usually performed. Moreover, the SERS spectra of the same protein can show differences due to the different interaction with the plasmonic nanostructures [22,100]. For such reasons, the direct detection of proteins can still be quite challenging. Several approaches have been proposed to address these issues.

In an effort to solve the problems related to the low SERS signal of proteins, a multi-marker approach has been proposed [101]. Such method is based onto the simultaneous detection of several protein biomarkers involved in lung cancer, exploiting an antibody-antigen-antibody sandwich configuration [101]. The developed protocol foresees a first interaction of the target antigen with the corresponding antibody adsorbed on a layer of chitosan-stabilized Au NPs. Then, a further antigen-antibodies interaction takes place with a second antibody immobilized on Au microspheres labelled with a Raman reporter (Figure 2.12a, b) [101]. This configuration allows a multiplex detection of different antigens exploiting the selective interactions with their antibodies. Another approach, proposed by the Matteini's group [86], exploits the corner sites of Ag nanocubes, that are responsible for the 80% of the total signal of the target, for the direct SERS detection of proteins (Figure 2.12c). The presence of a thin layer of PVP coating causes the peptides to preferentially adsorb on the edges of the plasmonic nanostructures, rather than along the cube faces. In this way, the signal fluctuations caused by the different orientations of the protein on the surface of the nanostructures are prevented.

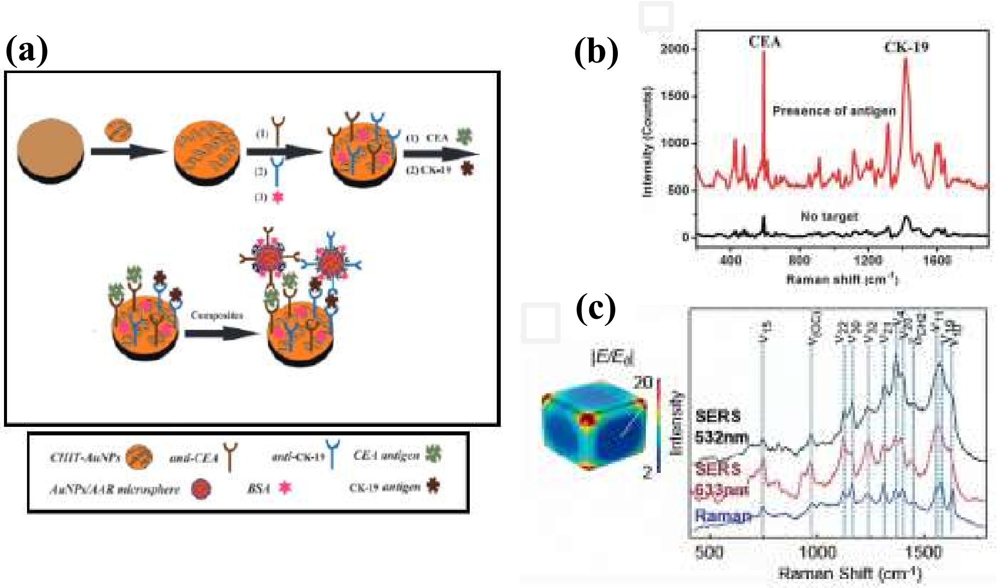

Figure 2.12 – a) Schematic illustration of the sandwiched structure due to the interaction of the electrode coated with the first antibodies and the Au NPs coated with the second ones [101] **b) Representative 785 nm excited SERS spectra of the immunosensors for blank control (black line) and a mixture of 20 ng/mL CEA and 20 ng/mL CK-19 solutions** [101] **c) FEM simulation of the electric field distribution of a 50 nm nanocube and SERS spectra of 0.1 M solution of cytochrome c obtained on Ag nanocubes by using 532 nm (black) and 638 nm (red) excitation wavelengths.** [86].

2.3.2 Nucleic acid detection

In addition to the above mentioned challenges for the protein identification, the SERS detection of DNA displays additional difficulties because of its composition. Indeed, such molecules are made of four different bases whose relative content characterizes each sequence. The selective recognition could therefore be troublesome, in particular when the content of the different bases is similar. On the other hand, the quite high Raman cross-section of the bases could be combined with the boosted sensitivity granted by SERS, achieving low detection limits. The first approaches concerned the analysis of the DNA components, thymine (T) (uracil

(U) in RNA), guanine (G), adenine (A), and cytosine (C) [102,103], and afterwards the focus was gradually shifted towards longer sequences, up to DNA and RNA [104,105]. The building block of the nucleic acid polymeric chains are the nucleotides. Every nucleotide, that correspond to the monomer of the polymeric chain, is composed by a nitrogeneous bases which is bonded in position 1' to a 3'-phosphorylated deoxyribose ring. Each monomer is then connected to another one through a link taking place between the C5' of the nucleotide sugar and the phosphate group of the successive one (Figure 2.13a). The resulting DNA chain is thus characterized by a specific direction. Moreover, in physiological conditions it displays a negatively charged backbone, which affects the interactions between the chains. The double stranded DNA configuration, in which specific bases are paired (A-T, C-G), is kept together thanks to the hydrogen bonds between the heterocycles (Figure 2.13b, and c) [106]. Such pairing between bases takes places also for oligo, such as DNA-DNA complexes and hetero-nucleotides, like RNA-DNA duplex, and is called hybridization. This interaction is highly specific and therefore is largely employed in biosensing. Depending on the pairing between the bases and on the oligonucleotide sequence length, different binding energies are obtained, allowing to define the melting temperature of the hybridized complex [107]. This value refers to the temperature at which 50% of the double-stranded DNA has denaturated to single-strand DNA.

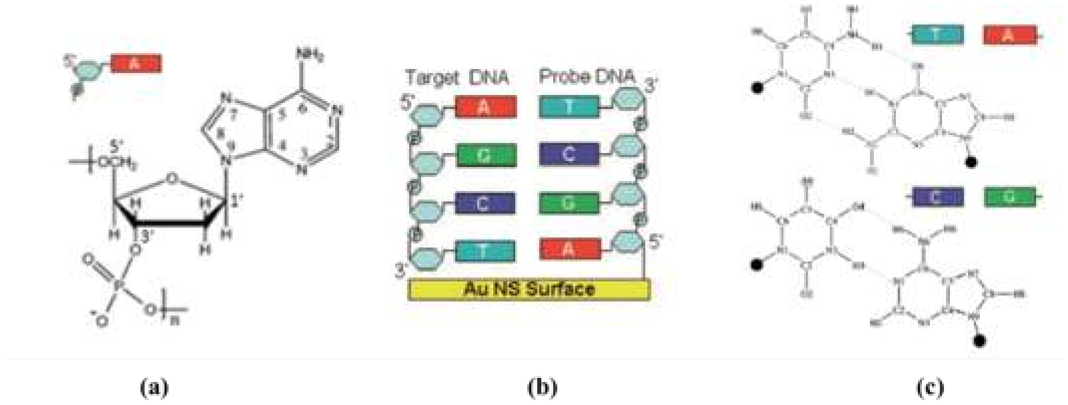

Figure 2.13 - a) Adenosine monophosphate nucleotide; (b) hybridization between an immobilized probe and a free target oligonucleotide. (c) Hydrogen bonding that take place between thymine and adenine, at the top, and cytosine and guanine, at the bottom [107].

The SERS detection of nucleic acids is often based on sandwich hybridization with complementary probes [22]. The use of a Raman label is often required due the close similarity of Raman fingerprints of the probe and the target oligonucleotide. However, some attempts of a label-free detection of DNA have been made. The Halas group developed a protocol exploiting an adenine-free DNA probe, substituting each adenine with 2-aminopurine, thus preserving the hybridization efficiency while presenting a different spectrum. The amount of DNA hybridized was measured by the adenine: 2-aminopurine band intensity ratio [108].

An alternative approach was employed by the Alvarez-Puebla group, who exploited positively charged spermine coated Ag NPs to detect nucleic acids. Stable duplexes were obtained, thanks to interaction between the negatively charged DNA and the positively charged NPs, allowing to obtain reproducible SERS spectra of probe/DNA complex [109].

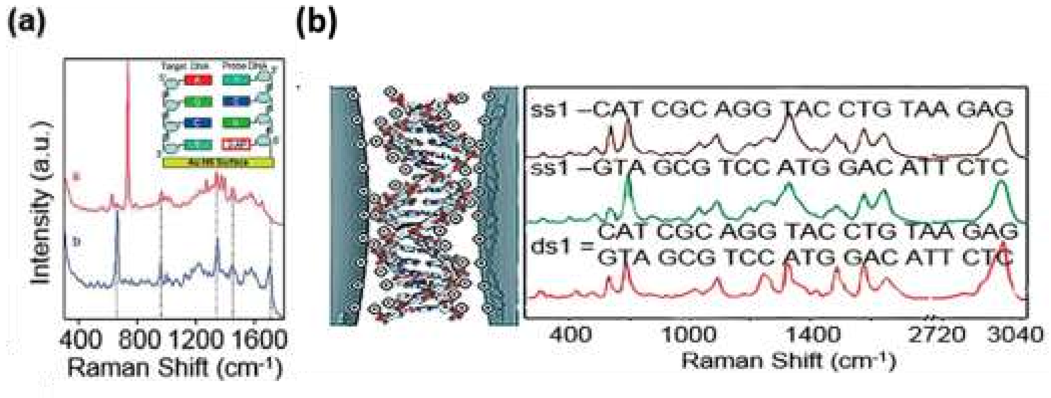

Figure 2.14 - Schematic diagram of different label-free approaches to DNA detection. a) SERS detection by hybridization with adenine-free DNA sequences [108]**. b) Spermine-modified Ag NPs for DNA detection.** [109]

2.3.3 Micro-RNAs detection

MicroRNAs are small non-coding RNA strands, composed by ~ 22 nucleotides, that can be found in several plants, animals and viruses [110]. Their function within the cell nucleus is to carry out a post transcriptional regulation function on gene expression, acting on the protein synthetic pathway. More in detail, they interact with the mRNA that carries out the transcript of the information contained in the genes that are required for the ribosomes to assemble the aminoacids. This interaction, occurring in the cell cytoplasm, is mediated by the RNA Silencing Complex (RSIC) [111], which binds the mature miRNA and drives its hybridization to the target mRNA [112]. Moreover, the regulation of a single gene expression can be carried out by multiple miRNA. As a consequence of the miRNA involvement in almost all biological processes, ranging from the cellular development and differentiation to the alteration of the normal immune system functions, they have been extensively studied [107], and, to this date, over 1000 miRNAs have been identified in humans [113]. In the organism, miRNAs are found both as intracellular and extracellular species. In the extracellular environment, they can be found inside vesicles, such as exosomes, or associated with RNA binding proteins, in order to prevent their degradation from endogenous RNAases [114]. Their presence in plasma is strictly regulated, and an alteration in miRNAs concentration has been correlated to several diseases and cancer pathologies [107]. Circulating miRNAs have therefore been suggested as biomarkers for such pathologies, particularly due to their key role in cancer development and proliferation [115]. Moreover, the use of circulating miRNA could improve the present strategies towards the development of a non-invasive approach for the diagnosis of cancer diseases [95]. To this end, a monitoring platform is strongly needed.

However, the detection of miRNAs presents some issues due to their low abundance, small size and sequence similarity. Indeed, the miRNA population represents only a small fraction of the total cellular RNA (i.e. 0.01%) [107]. To detect such low concentration a very specific and highly sensitive assay is required, which nevertheless can be influenced by the sequence homology among miRNAs belonging to the same families [22]. Moreover, the miRNAs population greatly varies among each cell and the parallel analysis of different sequences is often required to provide a diagnosis [57]. The developed assay should thus provide a wide dynamic range of detection and multiplexing capability [107]. A popular approach exploits the hybridization between a labelled probe and the target miRNA, even though the low melting temperature could greatly reduce the hybridization efficiency and the sensitivity of the assay. The same issue affects the polymer chain reaction (PCR)-based methods due to the low primer/miRNA hybridization efficiency [107].

So far, the golden standard for the miRNA detection is the electrophoresis-based Northern Blotting, even though it requires complex sample treatments and does not provide a good sensitivity [116]. Another popular approach to profile large numbers of miRNAs is the microarray-based detection. This technique takes advantage of a microarray hybridization between miRNAs and an array of different complementary fluorescent labelled DNA probes. However, the selectivity is poor, due to the short miRNA sequence and their similarity, and a further validation step is usually needed [117]. In addition, such protocols are usually expensive.

In this framework, SERS spectroscopy could provide a sensitive and yet reliable method for the miRNA detection and discrimination [22].

Generally speaking, the SERS analysis of miRNAs can be achieved by directly adsorbing the target on the substrates (label-free approach) or taking advantage of a complementary probe, previously immobilized on the surface.

The first reported attempt for the SERS detection of miRNA was performed by Driskell et al., who analysed different miRNAs directly adsorbed on a silver nanorod array fabricated by oblique angle vapour deposition (OAD) [118]. More recently, hybridization-based assays for the SERS detection and discrimination of miRNAs have been deployed, exploiting different nanostructures functionalised with oligonucleotide probes labelled with a SERS reporter [83,84,119–123]. Especially concerning the analysis of complex matrixes, like blood or serum, this approach could provide a robust protocol for a sensitive detection of the targets [95]. Moreover, as for the label-free method, complex chemistry processes for the labelling of the analyte are not required. Hereby few examples of miRNAs detection using a hybridization-based platforms are reported.

Wang et al. developed an inverse molecular sentinel (iMS) label-free protocol, exploiting the distance variation between a Raman reporter bonded to a loop DNA probe and the nanostructures. Figure 2.15 shows a schematic representation of the OFF-to-ON iMS mechanism. A thiolated stem-loop probe, with a Raman label at its end, is anchored to the NPs and coupled with a complementary sequence (placeholder). In the absence of the target the SERS signal is very low, due to the distance between the reporter and the surface. Upon exposure to the miRNA, the placeholder catches the target and separates from the probe, allowing the stem to close its loop and bring the label close to the surface, therefore resulting in a stronger SERS signal [85].

Kim et al. reported instead the multiplex detection of miR-10b, miR-21, and miR-373, taking advantage of a sandwich hybridization assay using head-flocked gold nanopillars. As stated before, solid SERS substrates fabrication techniques usually allow a more precise control over the structural characteristic of the plasmonic structure. In this study a Si nanopillar mold was fabricated using a maskless RIE, followed by the gold deposition via an electron beam evaporation process. Nanopillars of 800 nm of height and 200 nm of width were thus synthetized. Moreover, upon exposure to liquid samples, these nanopillars lean towards each other, due to capillary forces that drive the self-clusterization of nanopillars heads. This phenomenon, named head-flocking effect, greatly reduces the gap between nanopillars and therefore a strong signal enhancement is attained [124–126]. Indeed, taking advantage of such configurations, quite low limits of detection were obtained, ranging from 3.53 fM, to 2.17 fM and 2.16 fM form miR-10b, miR-21, and miR373, respectively [84].

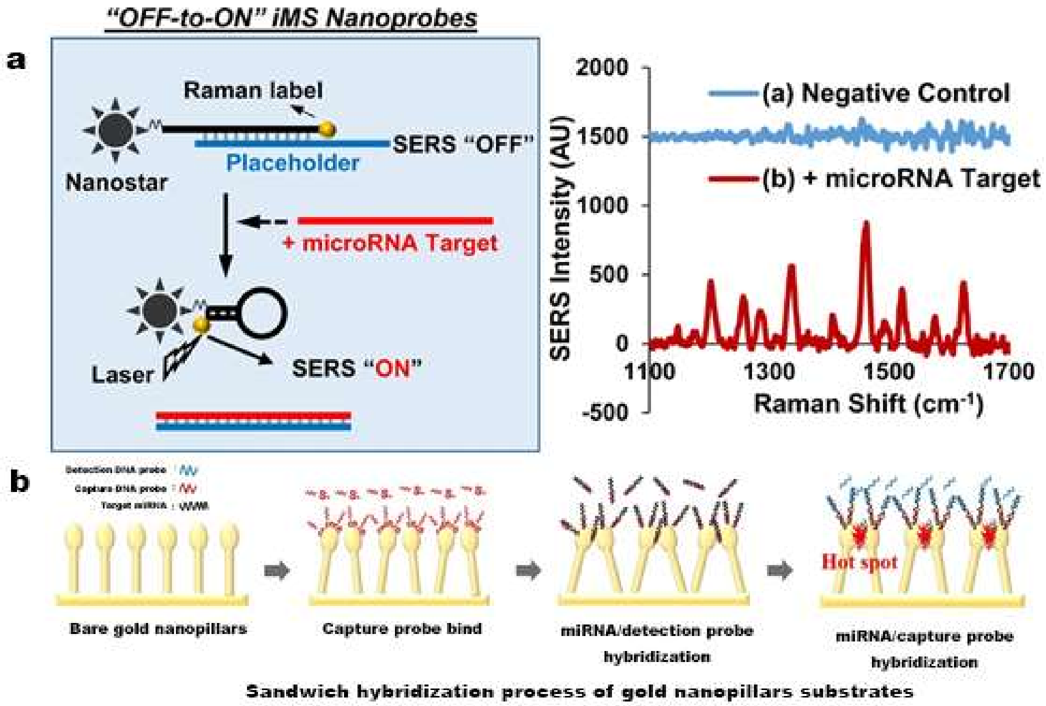

Figure 2.15 – a) Left: operating principle for the iMS detection approach (left side). Right: SERS spectra related to the OFF configuration (a) and to the On configuration (b) [85]. **b) Sandwich hybridization based assay for the multiplexing detection of miRNAs using head-flocked gold nanopillars** [84].

Hybridization-based assays have been also proved to be suitable for the microfluidic integration [83,127]. This configuration can be exploited to address issues related to a non-uniform molecular distribution along the substrate surface, and moreover, it enables the development of portable platforms for real time detection [74,127]. A microfluidic multiplex detection of DNA sequences, performed by Yazdi et al [81], has already been presented in the previous paragraphs (2.2.4). The obtained detection limit for the target sequence was 100 pM.

Wang et al. reported a microfluidic approach for miR-21 detection using a molecular beacon (MB) labelled with 6-carboxyfluorescein (6-FAM) and adsorbed on Ag nanoparticles [128]. MB are single-stranded DNA molecules displaying a stem-loop structure. The loop portion is a probe for a complementary target sequence, while the stem is made by the annealing of two complementary sequences located on either sides of the probe [129]. In fluorescence-based assay, these two terminals are usually labelled with a quencher and a fluorophore, respectively. Therefore, in a non-hybridized configuration the quencher and the fluorophore are closed to each other, and a weak fluorescence signal is observed. Upon exposure to the target analyte the loop opens, increasing the distance between the fluorophore and the quencher, and therefore a fluorescence signal raise is detected [129]. In this study a combination of fluorescence and SERS spectroscopy is exploited, using 6-FAM both as fluorophore and Raman reporter. If 6-FAM is close to the surface a strong SERS signal as well as a weak fluorescence signal are expected, whereas after the hybridization with miR-21 the loop unfolds resulting in a weak SERS signal and a strong fluorescence one. Finally, the microfluidic approach was exploited to drive the injection of different concentrations of miR-21, down to 10^{-9} M.

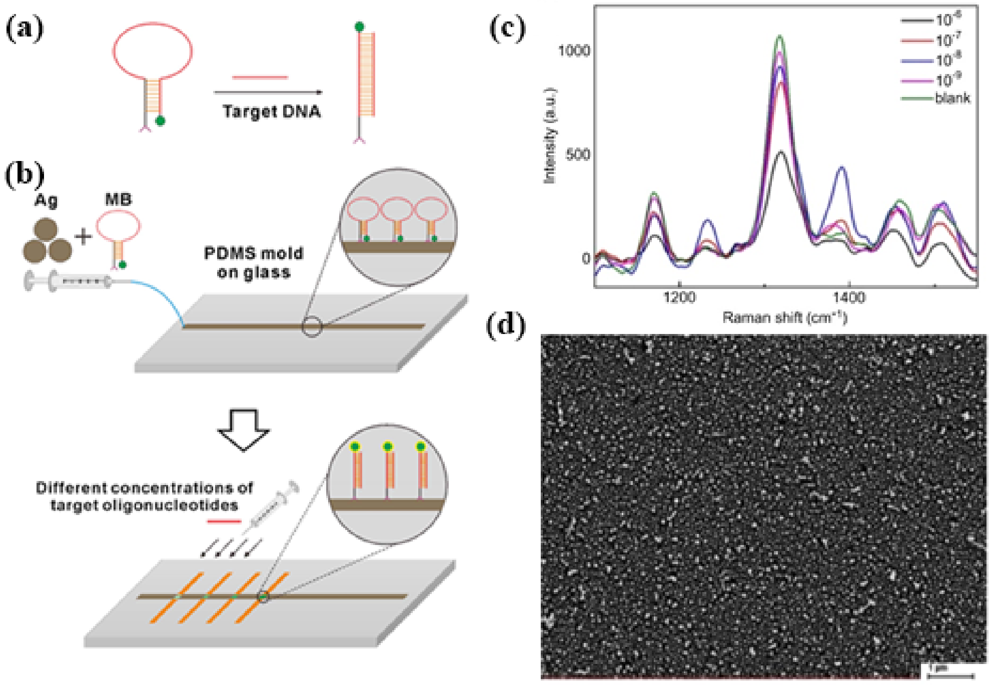

Figure 2.16 – a) The working mechanism of the designed molecular beacon. Once encountering the target DNAs, the hairpin shape MB opens up as a double stranded DNA. b) Schematic diagram of the microfluidic assay of the target oligonucleotides. c) The SERS spectra of the MB probes with different concentrations of target DNAs. d) SEM image of silver film substrates [128].

As reported in this section, SERS spectroscopy has been proven to be suitable for the miRNAs detection. A wide range of configurations can be exploited in order to maximize the SERS signal enhancement of the target analyte, and moreover the microfluidic integration opens new avenues for the instrument-related cost reduction and real time detection.

2.3.4 Bacteria detection

Nowadays, there is a need for an affordable and sensitive method to detect pathogenic microorganisms in different areas of our everyday life, ranging from biomedical applications to water and food safety [83,130–132]. Recently the vibrational spectroscopies, as infrared and Raman spectroscopies, have attracted significant interest in the investigation of bacterial populations and more widely, in the characterization of biological environments [133,134].

Bacteria are prokaryotic microorganisms, meaning that they do not display any nucleus inside the cytoplasm liquid but instead the genetic material is dispersed in such intracellular matrix [133]. A first envelope, namely the cytoplasmatic membrane, is designed to contain the cytoplasm and furthermore the presence of a second layer, surrounding the first one, completes the bacterial cell wall. The composition of this outer membrane can vary from each bacterial strains and the most diffused characterization technique of the bacterial species, the Gram staining method, takes advantage of its architecture [135]. Indeed, thanks to this procedure each bacterium has been assigned to two separated macro-categories, Gram-positive and Gram-negative. The Gram staining differentiates bacterial strains detecting a specific component of the outer layer, the peptidoglycan [133,135,136], a polymer composed by linear chains of amino sugars whose major components are N-acetyl glucosamine (NAG) and N-acetyl muramic acid (NAM) [87,89]. As shown in Figure 2.17a, the cell wall of Gram-negative bacteria is made of an interior cytoplasmatic sheet and a multilayer outer membrane, composed by a phospholipidic region in which several other components, such as lipids and transmembrane proteins, (mainly porins) are embedded [133,137]. A thin layer of peptidoglycan, namely the periplasmic space, lies into the space between these two membranes. Gram-positive bacteria, instead, display an outer membrane, mostly composed of peptidoglycan (Figure 2.17), producing a thick polymeric layer, in which a small amount of lipoteichoic acids are embedded [89,133].

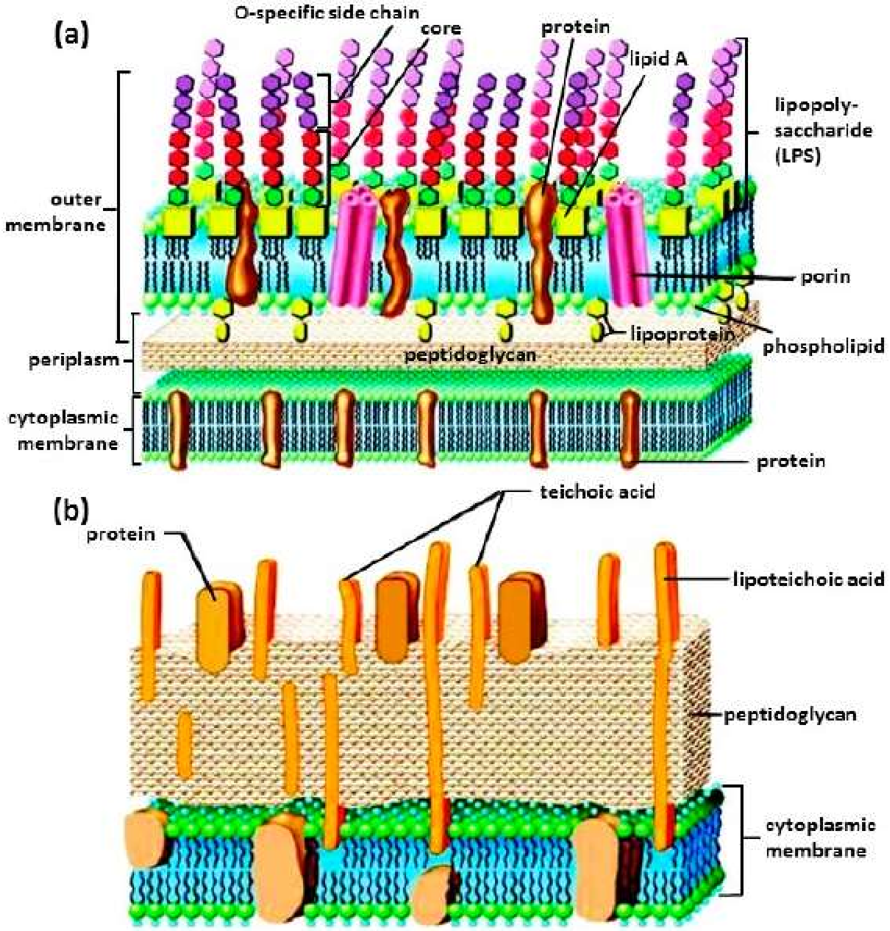

Figure 2.17 - a) Gram-negative bacterium; and (b) Gram-positive bacterium. The membranes of Gram-negative bacteria are composed of two layers: the outer membrane rich in lipopolysaccharide (LPS) and the inner membrane rich in anionic phosphatidylglycerols (PG). Gram-positive bacteria have a cell wall consisting of lipoteichoic acid and peptidoglycan and a cytoplasmic membrane [133]

These differences not only lead to a different colour of the bacterial colonies as a results of the Gram staining test, but they strongly affect the Raman vibrational pattern too, allowing to selectively distinguish between species.

Usually, microorganisms do not live as single cells but they show a tendency to aggregate, producing a biofilm in which the bacterial cells are plunged [138,139]. The generated extracellular matrix is composed by several biopolymers, named Extracellular Polymeric Substances (EPS), and its composition drives the architecture of the biofilm itself. The biofilm matrix plays a key role into the evolution of the bacteria providing a safer environment for the growth of the microorganisms [138,140]. Several functions of the EPS have been determined ranging from the immobilization of the cells allowing for an intracellular communication to the retention of water and water soluble nutrients. It can host several biological components such as enzymes, proteins, lipids, that could be useful for the bacteria, and extracellular DNA (eDNA), that promotes the exchange of genetic information between cells [140,141]. Finally, it protects the bacterial cells from several factors that could harm them, such as oxidation, ultraviolet radiation and some antibiotics [138].

In this field of application, one of the most prominent techniques that has emerged as promising approach is SERS, that combines an ultra-high sensitivity with non-destructive characteristics [142–145].

A first approach is to coat the bacteria cells with colloidal silver or gold NPs, achieving the formation of a thin metallic film entirely or partially covering the cells [91,146,147]. The most widespread method consists in soaking the bacterial cells in a sodium borohydride solution, and then resuspending them in a silver nitrate or chloroauric acid solution for the in-situ reduction of the noble metal cations. [90,91,146,148]. However, the NPs synthetized using such method were shown to accumulate near adenine containing compounds due to the preferential interactions between silver ions and adenine [133].

A second approach concerning the use of colloidal SERS substrates is to synthetize the NPs inside the bacteria, but the resulting SERS spectra are generally weaker with respect to the ones collected using external colloidal NPs [133].

Finally, a mixture of bacterial suspensions and colloidal NPs can be exploited to collect the SERS spectra. Furthermore, using capped or uncapped NPs led to different SERS spectra due to the ability of capped particle to bind the cell membrane [133]. Particle capping is usually performed using citrate, due to it weak electrostatic interactions with noble metals (i.e. Au, Ag) enabling its displacement by ligands with stronger affinity.

Lemma et al. performed the discrimination between Gram-positive and Gram-negative bacteria (*Lactobacillus rhamnosus* and *Escherichia coli*, respectively) using Ag nanoaggregates and measuring both intracellular components (lysed cells) and the cell surface (non-treated cells) [88]. The comparison of the collected spectra shown in Figure 2.18 highlights several differences due to the distinct above mentioned characteristics; in the case of Gram-positive cells, the outer lipid membrane is missing and therefore the cell wall (peptidoglycan) is directly accessible from outside the cell. In contrast, in Gram-negative cells the peptidoglycan is shielded from the surrounding environment by an outer cell membrane. Therefore, the chemical composition of the outermost layer of the cell differs significantly.

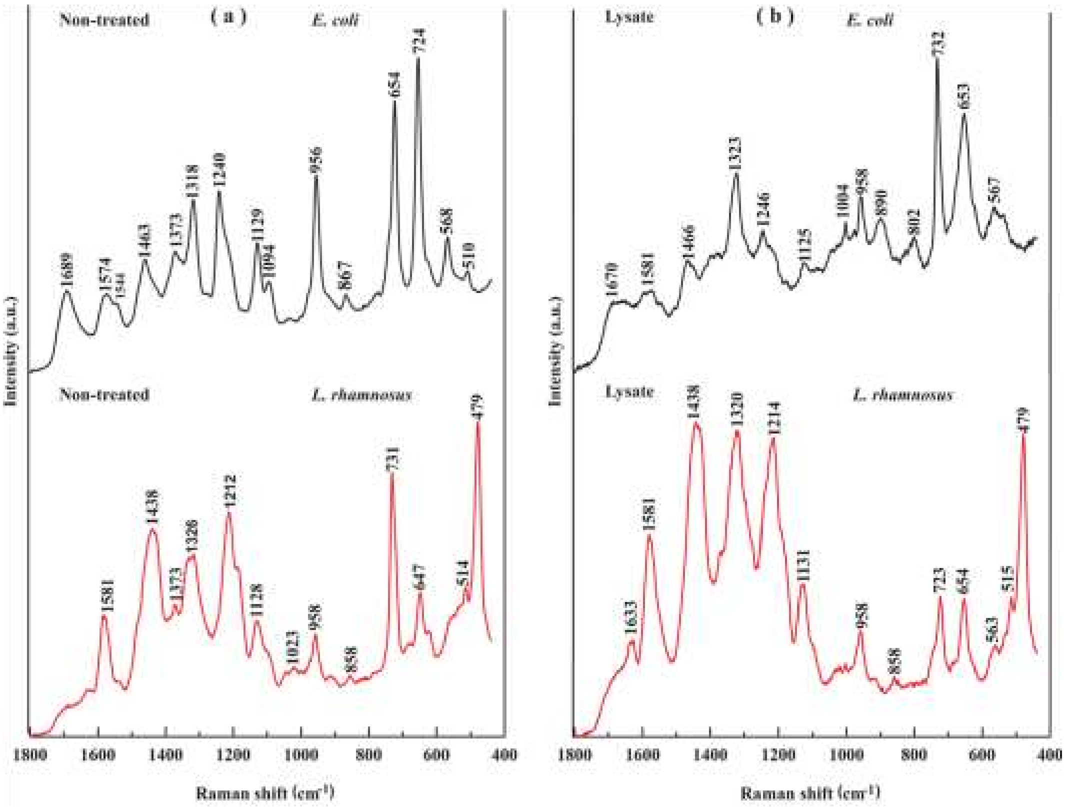

Figure 2.18 - SERS spectra of: (a) non-treated cells and (b) lysate of *E. coli* and *L. rhamnosus* [88].

An interesting approach was exploited by Neugerbauer et al [89], using Tip-Enhanced Raman Spectroscopy (TERS), a technique that combines the scanning probe microscopy (SPM) with the plasmon enhanced Raman spectroscopy, allowing high resolution chemical imaging. A complete characterization of the vibrational pattern of *Staphilococcus epidermidis* was carried out. The spectral variations are justified by the heterogeneity and complexity of the bacterial cell surface. Gram-negative bacteria biofilm matrix is largely composed by N-acetyl glucosamine, as component of the surface itself and of the polymeric chain of polysaccharide intercellular adhesin (PIA). A TERS spectrum of the pure substance is shown on the top of Figure 2.19. Several bands show a very good agreement with the Raman bands of the *S. epidermidis* membrane, confirming the rich abundance of this sugar on the cell surface. Furthermore, a spectrum using a confocal Raman spectrometer is shown at the bottom of the graphs to highlight the richer vibrational information provided by the TERS approach.

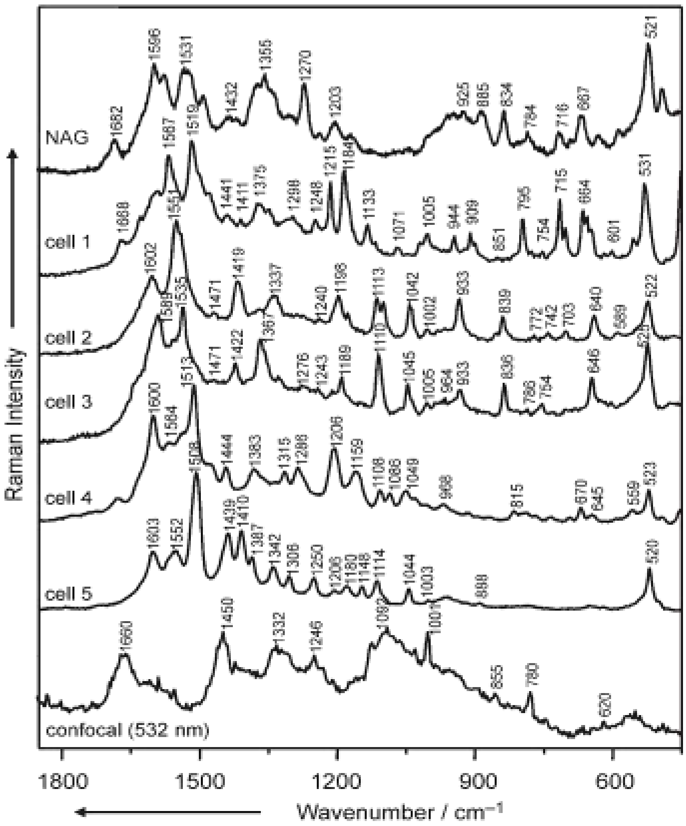

Figure 2.19 - Tip-enhanced Raman spectra of *S. epidermidis* ATCC 35984 (cell 1–5) and N-actetylglucosamine (upper spectrum). For comparison, a confocal Raman spectrum of a single *S. epidermidis* cell is shown as well at the bottom (exc. 532 nm) [89].

Chapter 3

3 Experimentals

3.1 Porous silicon electrochemical etching

Porous silicon was obtained through the electrochemical etching of boron doped silicon wafers (34–40 mW-cm resistivity) in a 20:20:60 hydrofluoric acid (HF)/water/ethanol solution. The anodization took place in a Teflon cell applying a current density of 102 mA/cm^2 for 35 seconds to produce a single porous layer with 68% porosity a 1.8 µm of thickness. For the dynamic flow synthesis protocol the anodization time was reduced to 7 seconds, aiming to produce thinner pSi layers and therefore allowing a greater transmittance of the UV-Vis radiation. In order to detach this porous silicon mono-layer (pSi) from the silicon substrate a second electrochemical attack was performed with a current density of 3.4 mA/cm^2 for 40 seconds in a low concentrated HF ethanol solution. Then the pSi layer was transferred onto a PDMS slice, obtained by polymerization of a mixture of PDMS oligomer and curing agent with a 10:1 ratio, cross-linked at 60 °C for 30 minutes. The whole procedure took place in a temperature-controlled environment at 20 °C.

In order to obtain the desired thickness and porosity of the porous silicon layer, a specular reflectance spectrum in the 200 – 3000 nm range was collected, using a Cary 5000 UV-Vis-NIR spectrophotometer. Then, the SCOUT 2.3 software was employed for the simulations of the specular reflectance spectra, setting the porosity and the thickness as fit parameters

3.2 Silver nanoparticles synthesis

3.2.1 Immersion plating

Silver nanoparticles were synthetized starting from a 10 mL 10^{-2} M aqueous silver nitrate solution, supplemented with 8 uL of $1{,}7\text{x}10^{-3}$ M HF solution, exploiting the reactivity of the pSi layer. A pre-treatment of the pSi/PDMS substrate in a 5% aqueous HF solution was required to dissolve oxidized silicon formed during the detachment, followed by a washing step in ethanol, before dipping it into the silver nitrate solution for 15 seconds at 20 °C. To end the reaction, the substrate was immersed in water and dried in nitrogen stream.

3.2.2 Microfluidic integration of the pSi-PMDS membranes

The detection of miR222 was carried out using pSi-based samples integrated in a microfluidic chip. The detailed fabrication of the chip and the following integration of the pSi membranes was developed and is described in previous works [119,127].

3.2.3 Dynamic flow synthesis

In order to investigate the effect of the synthesis parameters variation on the final size and distribution of the Ag NPs, an in-flow synthesis protocol was designed. A syringe pump was used to drive the injection of the $AgNO_3$ solution into a microfluidic chamber, hosting a pSi membrane with a diameter of 1 cm. The flow rate was varied in a range between 0 and 3 mL/min. The temperature of the precursor solution was controlled using a Julabo Corio CD thermostatic bath (20-60 °C). The growth of the NPs was monitored in situ via UV-Vis transmittance spectroscopy using a Cary 5000 UV-Vis-NIR spectrophotometer. A scan between 300 nm and 700 nm was performed every single minute, monitoring the evolution of the plasmonic dip. The nanoparticle growth was quenched by injecting water into the microfluidic chamber after 15 minutes, when a saturation regime was reached.

3.2.4 Image analysis

The morphology of a SERS substrate, especially concerning the NPs size and the inter-particle gap, plays a key role in determining its SERS efficiency. To characterize such features a MATLAB routine for the FESEM image analysis, previously developed by Novara et al [149], was employed. The script was then modified to remove the background noise, adjust contrast, separate NPs aggregates and to correct artefacts, allowing to distinguish between dense and spread particles. In order to obtain the size distribution of the NPs, each one was assimilated to a circular disk having the same area, whereas to calculate the gaps between NPs, a MATLAB operator was employed to measure the distance between each NPs and the closest one. Finally, the mode of the NPs gap was exploited in order to the better represent the dimension distribution.

3.3 Bioassay

3.3.1 One step and two-step bioassay optimization

SERS detection of miR222 (5’-AGCUACAUCUGGCUACUGGGU-3’)was based on a previously developed ELISA-like assay refined for metal-dielectric nanostructures [119]. In particular, two different approaches, based on different probes, were developed. The first one concerns the detection of the target miRNA using a one-step hybridization with a complementary 22-nucleotide-long thiolated DNA probe (probe222, 5’-C6SH-ACCCAGTAGCCAGATGTAGCT-3’) previously immobilized on the samples surface. The second approach, instead, deals with the detection of the target miRNA through a two-step assay. Indeed, the probe is divided in two halves, namely half1 (5’-C6SH-ACCCAGTAGC-3’) and half2-X (5’-CAGATGTAGCT-Cy3/Cy5-3’). The first half is immobilized on the surface and allows the selective bindings of the target miRNA, whereas the second half, which is modified with a Raman label, enables the detection in two hybridization steps. Both the probes were reduced with DL-Dithiothreitol (98.0% DTT), desalted (Illustra MicroSpin G-25 columns) and their quantification was carried out quantified before the immobilization on Ag-PSD samples, by overnight incubation in TE-NaCl (TE, 1M NaCl, pH 7.5). The detailed process can be found elsewhere [119]. The optimal surface probe density for the two protocols was estimated incubating different concentration of probes (1-50 μM) and/or of NaCl (0-2 M) in TE buffer. Negative controls were as well incubated overnight in TE-NaCl without the probe (no-probe control). A nonspecific binding removal step was performed by washing the samples three times in TE-t (TE, 0.05% tween, pH 7.5), after overnight incubation. A further blocking step with 1% BSA in TE was then performed. Different conditions were used concerning the miRNA hybridization step. In the one-step bioassay, after the BSA pre-treatment, the samples were incubated for 1 hour with 25 μL of miRNA at different concentration in SSC (saline sodium citrate) 4x-SDS (sodium dodecyl sulfate) (0.01% SDS, pH 7.5), and then washed three times with SSC 1x-SDS (0.01% SDS, pH 7.5). The same immobilization protocol was used for the two-step bioassay, with the addition that, after the BSA pre-treatment, the miRNA was incubated in SSC 5x-SDS (0.01% SDS, pH 7.5) and then the samples were washed in SSC 4x-t (0.05% tween, pH 7.5). Subsequently, the substrates were incubated with 25 μL of 1 μM half2 in SSC 5x-BSA-t (0.05% tween, 1% BSA, pH 7.5) for 1 hour and washed three times with SSC 4x-BSA-t (0.05% tween, 1% BSA, pH 7.5). A specificity test using different mixtures of miR222 and miR16 (5'-UAGCAGCACGUAAAUAUUGGCG-3'), at different concentrations, was performed to confirm the selectivity of the two-step bioassay.

3.3.2 Elisa-like protocol

The ELISA-like protocol was employed as a reference technique for the Raman results. The same protocol reported above was applied on the SERS substrates. In this assay a 5'-biotinylated miR222 (5'-biotin-AGCUACAUCUGGCUACUGGGU-3') and a 3'-biotinylated half2 (5'-CAGATGTAGCT-biotin-3') were used, as substitute of the cyanine labelled miRNA/half2, for the one-step and two-step hybridization bioassays, respectively. After the last incubation and washing steps, the samples were incubated with 25 μL of 0.5 μg/mL Str-HRP in SSC 4x-SDS for the one-step protocol, or in SSC 4x-BSA-t for the two-step protocol. A washing step was performed three times using a buffer solution with the same composition as the one employed for the incubation step, and afterwards the samples were developed. The addition of TMB led to the start of the colorimetric reaction, that was then stopped after two minutes by adding H_2SO_4 (0.5 M), with a 1:1 TMB:H_2SO_4 ratio. A 2100-C microplate reader (ivymen Optic System) was employed to suddenly measure the solution OD, performing the measurements at 450 nm and 630 nm. The amount of immobilized probe was calculated by means of an in-liquid titration curve of Str-HRP diluted in Milli-Q™: their OD was measured after the reaction with TMB. Comparing the normalized

OD obtained for different samples, with the titration curve, the surface density (molecules/cm^2) was calculated. A factor of 50, as Str/probe surface ratio, was used. Several replicates were analysed each one related to different experimental conditions, allowing to calculate the standard deviations of the measurements (SD), as reported by the errors bars in the ELISA-like measurement graphs.

3.3.3 Detection of miR222 in cell extracts.

The RNA cell extracts were obtained from Human NSCLCC H460 and miR222-transfected H460 cells, grown in RPMI 1640 (Roswell Park Memorial Institute medium) supplemented with 10% heat-inactivated fetal bovine serum, 2 mM L-glutamine and 100 U/mL penicillin-streptomycin. All transfections were performed using the serum-free Opti-MEM and Lipofectamine 2000 (Life Technologies, Milan, IT) reagent according to the manufacturer’s protocol. H460 cells were transfected with 100 nM of the miR222 precursor for 48 hours. TRiFAst kit (Euroclone, Milan, IT) and mirVana miRNA isolation kit (Life Technologies, Milan, IT) were respectively used to extract the total RNA samples and the small RNA- enriched samples. Afterwards, the two-step hybridization protocol was exploited to detect the miR222 in cell extracts. Once the half1 was immobilized, the samples were incubated with the cell extracts diluted 1:2 in SSC 10x to a final concentration of 5x. A subsequent incubation step with the labelled half2 (-CyX or -biotin for SERS or ELISA-like assay, respectively) was then performed. Reverse Transcription quantitative Polymerase Chain Reaction was employed to obtain the miR222 expression levels in all the tested RNA cell extracts (RTqPCR). For Real-time PCR, 500 ng of RNA was reverse transcribed with miScript Reverse Transcription kit, then amplified by using the miScript-SYBR Green PCR Kit and specific miScript Primer Assay. U6 RNA was used as a housekeeping control gene. miRNA expression was measured using Ct (threshold cycle) and the ΔΔCt method for relative quantitation of gene expression. The threshold cycle (Ct) value is usually referred to as the number of cycle required for the fluorescence signal to exceed the background level or threshold. For what concerns the quantitation of the gene expression, the ΔΔCt method can be used to obtain a normalised relative expression of a target gene with respect to a reference gene. More in details, a first normalized value (ΔCt) is calculated for each sample in which the Ct value for the target gene is normalized to the one of a reference gene, namely housekeeping gene. Afterwards, in order to compare the expression of the target gene in different samples, and possibly in different conditions, a second normalization is performed using as reference the ΔCt value of a selected sample, obtaining the ΔΔCt.

3.3.4 Bacterial culture

S. epidermidis (14990 ®ATCCTM) and *E. coli* (25922 ®ATCCTM) bacterial cells were both cultured at the Kyoto Prefectural University of Medicine on a brain heart infusion (BHI) agar medium (Nissui, Tokyo, Japan). Optical density (OD) measurements carried out at 650 nm were exploited to estimate the initial concentration of bacteria, using a E-MAX microplate reader (Molecular Devices, Tokyo, Japan). A phosphate buffer solution (PBS) was employed to diluted the bacterial suspension to 1.0 × 10^8 CFU/mL, u. Finally, 100 µL of bacteria solutions were plated onto a petri dish containing BHI agar. The plates were incubated at 37 °C under aerobic conditions for 12, 24, and 48 hours. In order to evaluate the microbial viability, the Microbial Viability Assay Kit-WST8 (Dojindo Laboratories Co., Ltd., Kumamoto, Japan) was used, following the manufacturer technical manual. The biofilm grown on agar plates was resuspended in PBS and the concentration of bacteria was estimated by measuring the OD at 650 nm. The suspension was eventually diluted to 1.0 × 10^8 CFU/mL, and then 190 µL were incubated with the WST8 reagent (2-(2-methoxy-4-nitrophenyl)-3-(4-nitrophenyl)-5-(2,4-disulfophenyl)-2H-tetrazolium) for 30 min at 37 °C. Afterwards, the OD at 490 nm was measured with the E-MAX microplate reader. The mean value and its standard deviation, that is represented by the error bars, have been calculated performing three replicas of the experiment.

3.4 Optical characterization

3.4.1 UV-Vis Spectroscopy

In order to evaluate the porosity and the thickness of the pSi layer, specular reflectance spectra were recorded in a spectral range from 200 nm to 3000 nm as reported in the section 3.1.

The dynamic in-flow synthesis of Ag NPs was in-situ monitored performing a transmittance scan in a range between 300 nm to 700 nm (section 3.2.3).

3.4.2 Field Emission Scanning Electron Microscopy (FESEM)

Morphological characterization was performed using a SUPRA 40 FESEM system. pSi/PDMS membranes decorated with Ag-NPs were covered with a copper grid, connected to the FESEM stub, aimed to mitigate the electron charge-up process. Typical imaging parameters were an acceleration tension between 2.5-5 kV, a working distance of 3.5 mm and an aperture size of 20 µm. For each sample, at least a 50 kx and a 100 kx magnification images were taken (other magnifications were used when required). The morphological characterization was performed via Field Emission Scanning Electron Microscopy (FESEM) using a SUPRA 40 system.

3.4.3 Raman analysis

3.4.3.1 4-mercaptobenzoic acid

4-mercaptobenzoic acid (4-MBA) was exploited as a probe to investigate the efficiency of the synthetized substrates. Each sample was incubated in 1 mL of 1 µM 4-MBA ethanolic solution for 30 minutes, and afterwards gently rinsed with 1 mL of ethanol for three times. After removing the ethanol, the samples were dried in air. A Renishaw InVia Qontor Raman Microscope was used for the Raman measurements using a 532 nm laser excitation wavelength. A streamline configuration was exploited to map the whole surface: in this particular configuration each imaged point of the sample traverses a laser line once. In this configuration the laser spot is modified to a line of several microns under which the sample is scanned. The correlation of the acquired signal to specific sample coordinates is possible thanks to the synchronization of the stage motion and the change in the illuminated area of the CCD. A 10x objective was used to perform the Raman measurement using 4 s as exposure time, with a laser power of 1%. An average of 1600 collected spectra were acquired on a 2000 µm x 2000 µm area, using a 50 µm step along the Raman maps.

3.4.3.2 Rhodamine 6G

Rhodamine 6G was dissolved in ethanol and then diluted in order to prepare different solutions with concentrations from 10^{-6} M to 10^{-14} M. Afterwards, 5 µL of the selected solutions were spotted on the substrate surface, over a 0.07 mm^2 area, and the SERS spectra were recorded, after drying. To collect the spectrum a 514.5 nm laser excitation line was exploited using a 50x objective.

3.4.3.3 Bioassay for miRNA detection

The samples were analysed, after each functionalization step of the one/two-step protocol, using a Renishaw InVia Reflex micro-Raman spectrometer (Renishaw plc, Wotton-under-Edge, UK) with a 514.5 nm laser excitation in backscattering light collection under a long working distance 100x objective. The surface of each samples were mapped over an area of 40 µm x 50 µm, with a 5 µm step, using a laser power of 0.05%. The collected spectra were then analysed by means of the hyperspec package in R (R 2017, Foundation for Statistical Computing, Vienna, Austria. https://www.R-project.org/). A curve fit routine of the Renishaw software Wire 3.4 was instead exploited for the analysis of the spectra used for the calibration curves. The LODs were calculated using the mean value of the blank samples plus three times their SD, considering the linear range of the calibration curves (Raman signal intensity vs. miRNA concentration) for each protocol.

3.4.3.4 Bacteria detection

In order to avoid the presence of competitive microorganism a UV sterilization process was performed on the SERS for 24 h (15 W). The bacteria were than directly transferred from the agar plate on the substrates, promptly before the SERS measurements. A confocal Raman microscope LabRAM HR800; Horiba/Jobin-Yvon, Kyoto, Japan) equipped with 633 nm excitation wavelength and a 100x objective with a laser spot of 1 µm was used to collect the spectra. Ten different replicas performed on different spots of the samples were used to calculate the average spectra. Assuming an average dimensions of the bacterial cells of about 1 µm, we can estimate that each replica is performed on a minimum amount of one cell, if the spot is perfectly centred on the cell, and on a maximum amount of three cells. All of the spectra were normalized and processed using a commercial software (LabSpec 5.0, Horiba/Jobin-Yvon, Kyoto, Japan and Origin 8.5, OriginLab Co., Northampton, MA, USA).

Aim of the work

This work of thesis is devoted to depict and to investigate the potentiality of the pSi-based SERS substrates for biological applications. To this aim, the experimental work has been divided in two main section. A first part is dedicated to a more precise understanding of the synthesis process of the Ag decorated pSi substrates, and how it can be affected by the variation of the synthesis parameters. To achieve a better control over those parameters a microfluidic approach was exploited. The second section is devoted to the biological application of the SERS substrates, and in particular the focus was shifted towards the selective detection of miRNAs, and in particular miR222, and the discrimination of different bacterial strains, namely *Escherichia coli* and *Staphylococcus epidermidis.* Concerning the miRNA detection, two different protocols were designed taking advantage of the selective hybridization of the target miRNA with a complementary DNA probe. The first assay exploited the selective recognition of a miRNA labelled with a Raman reporter, thanks to its hybridization with a complementary thiol-capped probe previously immobilized onto the substrates surface. Instead, the second assay concerned the split of the probe in two halves. The first half of the probe is in fact immobilized on the substrate surface, ensuring the capture of the target miRNA, followed by the hybridization of the second half, labelled with a Raman reporter, of the probe with the selected miRNA.

The bacteria detection and discrimination was carried out designing a simple protocol for an *in-situ* and label-free analysis, that minimally affected the bacterial environment. *E. coli* and *S epidermidis* were selected as representative strains of Gram-negative and Gram-positive bacteria, respectively.

Chapter 4

4 Dynamic flow synthesis

4.1 Introduction

In section 1 the noticeable advantages of a dynamic flow synthesis, compared to the static one, have been presented and discussed. In this section, a microfluidic approach for the synthesis of pSi-based SERS substrates was exploited. To this aim, a pSi membrane was integrated in a microfluidic chamber in which the silver precursor solution was injected. The synthesis parameters variation was then investigated in order to understand the effect of each synthesis parameter on the final morphology of the silver NPs. Moreover, the existence of a correlation between each substrate morphology and the related SERS efficiency and reproducibility has been investigated.

4.2 Morphological characterization

Porous silicon platforms were prepared as stated in the section 3.1. An ultrathin porous silicon layer was produced to maximize the transparency of the final device, reducing the anodization time to 7 seconds to obtain a membrane with a thickness of 300 nm. This membrane was then integrated in the microfluidic chip, by following the fabrication protocol previously developed in our research group [150], which was subsequently sealed in order to prevent leaks concerning liquid analytes. The active area in the microfluidic chamber, corresponding to the area of the pSi surface, is 0.785 cm^2. A motorized syringe was used to drive the injection of the Ag precursor solution in to the microfluidic chamber. The temperature of the precursor solution was controlled using a thermostatic bath. The experimental setup is shown in Figure 4.1.

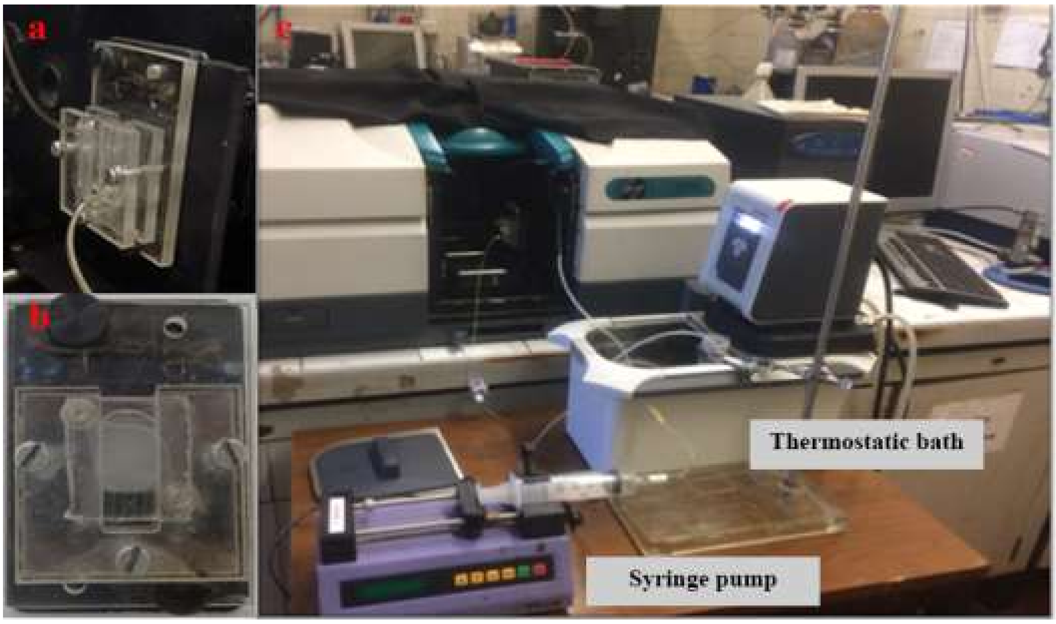

Figure 4.1 Experimental setup for the dynamic synthesis. a, b) microfluidic chamber hosting the ultrathin pSi layer. c) A syringe pump drives the injection of the silver precursor solution into the microfluidic chamber located inside the UV-Vis spectrophotometer. The temperature of the precursor solution is controlled by means of a thermostatic bath

The growth of the NPs was monitored in situ via UV-Vis transmittance spectroscopy. Figure 4.2 shows the transmittance spectrum of the microfluidic chip filled with water, as a reference (Figure 4.2a). As the silver nitrate solution is injected in the microfluidic chamber, promoting the NP synthesis, a clear spectral dip located at around 400-450 nm is noticed, becoming more evident as the reaction proceeds (Figure 4.2b, and c). The appearance and the evolution of such spectral feature is due to the rise of the LSRPs, witnessing the formation of the silver NPs. Furthermore, a shift towards higher wavelength as well as a broadening of the dip are observed for longer times, both due to the bigger size and an increasing density of the NPs. The reaction reaches a saturation regime after 15 minutes.

Hereby we studied the effect of the variation of each parameter (in the ranges reported in Table 1), like temperature, flow rate, and concentration of the precursor solution, influencing the growth kinetic, aiming to determine which synthesis conditions could lead to the fabrication of reliable and performing SERS substrates.

Table 1 – Synthesis parameters along with the corresponding tested range

Synthesis parameters	Range
[$AgNO_3$]	10 – 100 mM
Temperature	20 – 60 °C
Flow Rate	0 – 3 mL/min

The morphological characterization of the obtained samples was achieved through FESEM, allowing to acquire images of the samples surface. Furthermore, an image analysis experiment was performed on each acquired image in order to obtain the size and inter-particle distance distribution of the synthetized NPs.

Finally, the uniformity and the intensity of the SERS signal was evaluated using 4-mercaptobenzoic acid as molecular probe.

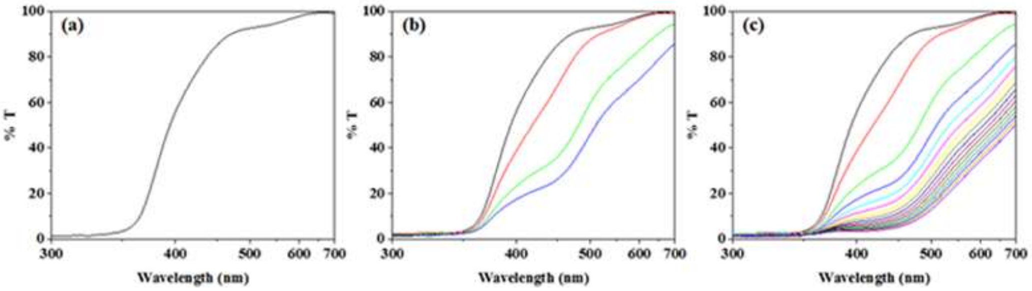

Figure 4.2 - UV-Vis transmittance spectra of the chip showing the plasmonic dip evolution at a) 0 min, b) 3 min, and c) 15 min, using a 10 mM $AgNO_3$ solution at 20 °C with a flow rate of 1 mL/min. Each spectrum has been collected every single minute.

In order to understand the effect of each synthesis condition on the kinetic of growth of the NPs, only one synthesis parameter at a time has been varied, highlighting his influence on the synthesis outcome. Furthermore, an open porous silicon membrane was attached to a plastic cuvette and subsequently covered with a silver nitrate solution, whose concentration and temperature has been also varied as listed in Table 1, to obtain a comparison between the static and the dynamic synthesis protocol.

Figure 4.3 shows the UV-Vis transmittance spectrum obtained from the synthesis in static conditions using a 10 mM (Figure 4.3a) and a 100 mM (Figure 4.3b) silver precursor solution, compared with the results obtained from the dynamic protocol using the same concentration of $AgNO_3$ and a volumetric flow rate of 1 mL/min (Figure 4.3c, and d). Both the static and the dynamic synthesis were performed at 20 °C. It is easily noticeable that increasing the silver nitrate solution concentration leads to an increased reaction rate, meaning that the saturation regime is reached faster, particularly concerning the dynamic synthesis performed with a 100 mM $AgNO_3$ solution. This behaviour is clearly represented by the evolution of the plasmonic dips in each spectrum. Concerning the dynamic protocol, the decrement of the transmittance over time appears more homogenous (Figure 4.3c, d), if compared to the static conditions (Figure 4.3a, b). This distribution is directly affected by the kinetic of the reaction and can be used to gain information about the growth of the nanoparticles.

As can be noticed in Figure 4.3, once the saturation regime is reached, the transmittance of the samples fabricated using higher $AgNO_3$ concentration in dynamic conditions appears to be strongly reduced, if compared to the ones synthetized using different reaction parameters. This suggests that the silver coverage of such substrates is higher, probably due to the formation of Ag NPs inside the pSi layer pores.

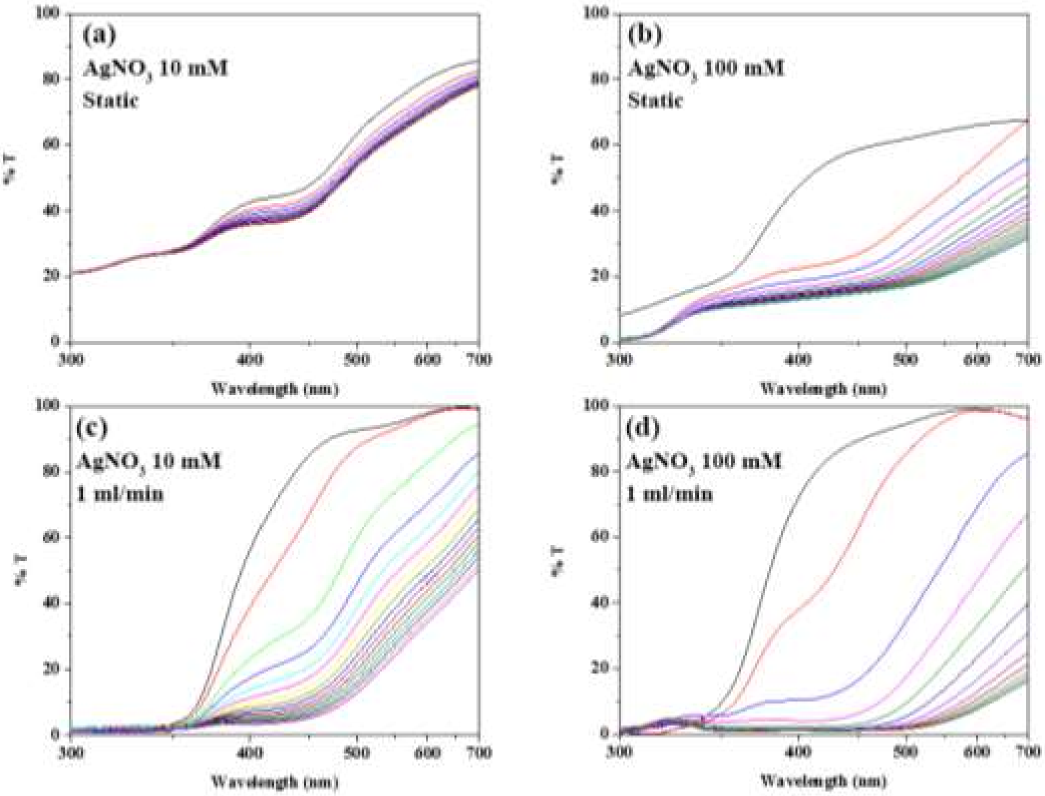

Figure 4.3 – UV-Vis transmittance spectra of the chip showing the plasmonic dip evolution for different synthesis conditions: a) static synthesis using a 10 mM $AgNO_3$ solution at 20 °C. b) static synthesis using a 100 mM $AgNO_3$ solution at 20 °C. c) dynamic synthesis using 10 mM $AgNO_3$ solution at 20 °C with a flow rate of 1 mL/min. d) dynamic synthesis using 100 mM $AgNO_3$ solution at 20 °C with a flow rate of 1 mL/min.

Indeed a key role is played by the mass transfer [72] of $AgNO_3$ from the solution bulk to the active surface of the pSi layer, where the formation of the Ag nuclei starts. This strongly affects the nanoparticles growth rate particularly in static conditions where the rate of the transfer is regulated by the diffusion of the silver nitrate towards the pSi layer, due to the concentration gradient, resulting in a low growth rate and a heterogeneous distribution of the nanoparticles nuclei. On the contrary, this problem is overcome in dynamic conditions, in which the mass transfer of silver nitrate is controlled by the flow rate of the solution, that can be easily tuned to produce the desired NPs [72]. The FESEM images collected from each sample (Figure 4.4), confirm such hypothesis, highlighting the role of the flow rate concerning both the NPs dimension and size distribution, whereas the $AgNO_3$ concentration only affects the particle size. Although the smaller NPs cannot be distinguished, due to the instrumental limits of the FESEM microscope in the analysis of poorly conductive samples, the pattern discussed before can be foreseen. Comparing the samples obtained by static synthesis (Figure 4.4b), the effect of an increment in the $AgNO_3$ concentration is displayed by the bigger size of the NPs obtained using a 100 mM $AgNO_3$ solution, whereas the use of a ten-time lower concentration lead to the production of very small silver particles. It is worth to notice that, in static conditions, the concentration raise causes a broader distribution of the diameters of the NPs. Concerning the samples obtained in dynamic conditions (Figure 4.4c, d), the only differences were related to the silver precursor concentration, while temperature and flow rate were fixed. Indeed, an increment in the particle size is observed in the samples obtained using a 100 mM silver nitrate solution, even though the increase is not as clear as for the static conditions. This difference could be due to the effect of the flow rate that has been proven to affect the particle size inducing the synthesis of smaller particle as the flow rate increase [73].

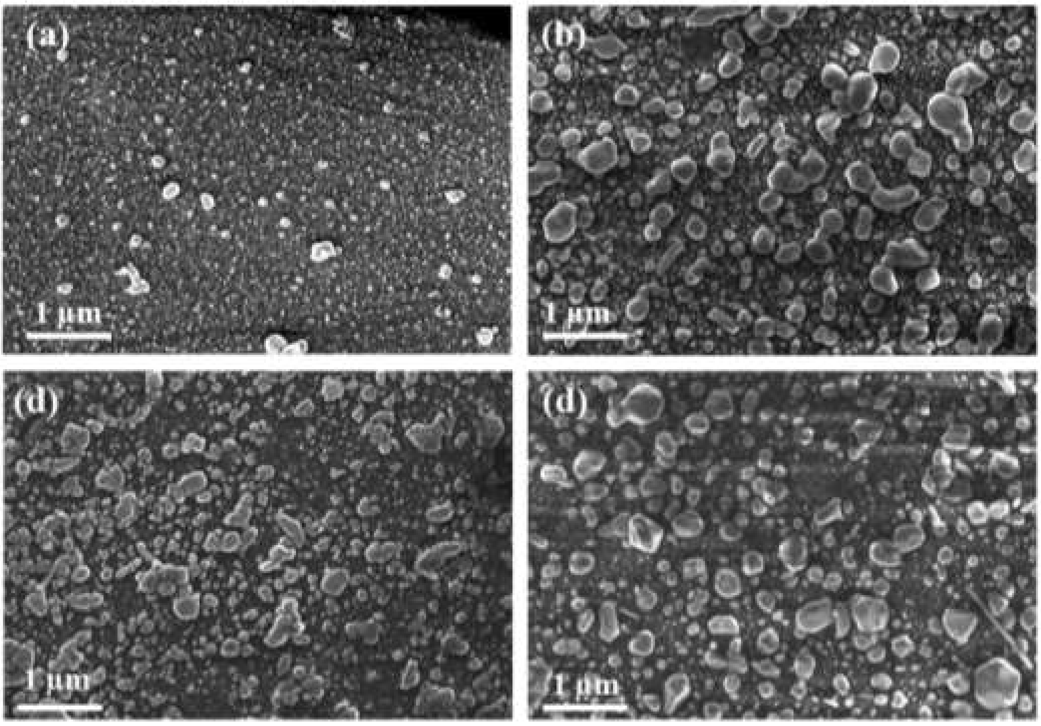

Figure 4.4 – FESEM micrographs of samples fabricated using different synthesis conditions: a) static synthesis using a 10 mM $AgNO_3$ solution at 20 °C. b) static synthesis using a 100 mM $AgNO_3$ solution at 20 °C. c) dynamic synthesis using 10 mM $AgNO_3$ solution at 20 °C with a flow rate of 1 mL/min. d) dynamic synthesis using 100 mM $AgNO_3$ solution at 20 °C with a flow rate of 1 mL/min

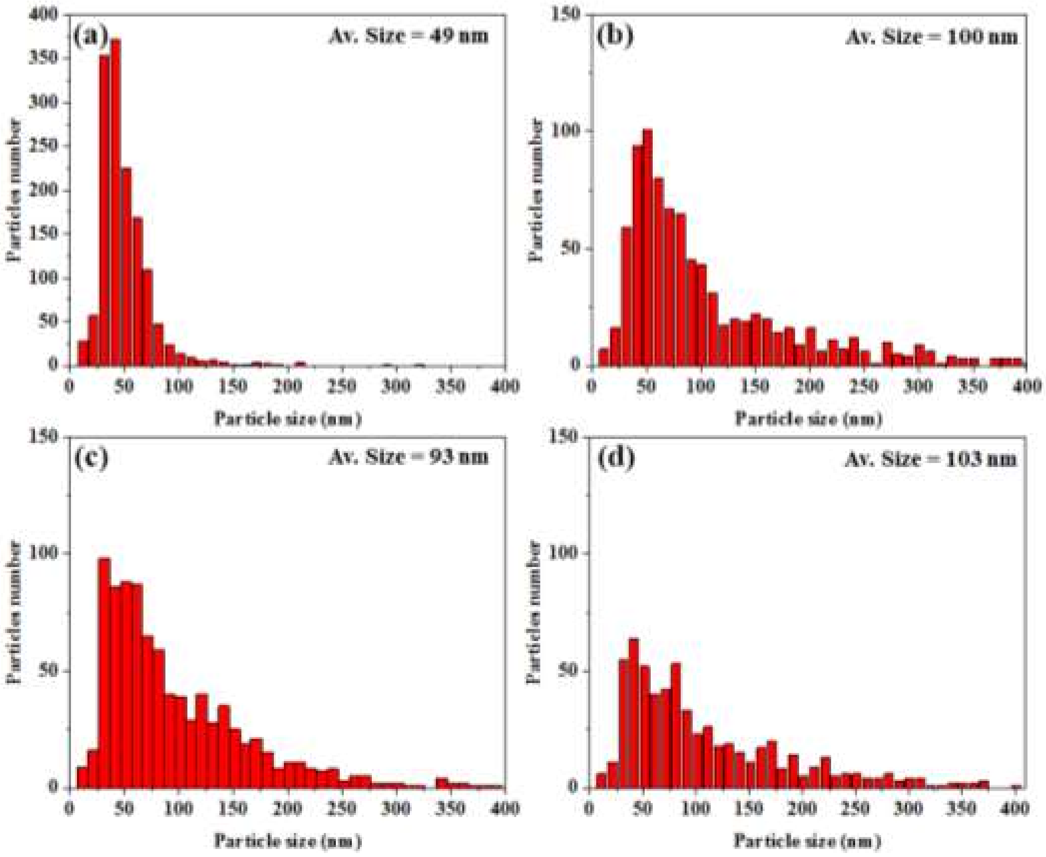

Figure 4.5 – Particle size distribution of samples fabricated using different synthesis conditions: a) static synthesis using a 10 mM $AgNO_3$ solution at 20 °C. b) static synthesis using a 100 mM $AgNO_3$ solution at 20 °C. c) dynamic synthesis using 10 mM $AgNO_3$ solution at 20 °C with a flow rate of 1 ml/min. Ld) dynamic synthesis using 100 mM $AgNO_3$ solution at 20 °C with a flow rate of 1 mL/min. The data were obtained by means of the MATLAB routine.

Additional data can be obtained from the results of the image analysis performed on the FESEM micrograph, displayed in Figure 4.5. The analysis shows that the narrowest size distribution and the smallest average dimension is attained the static conditions using a 10 mM $AgNO_3$ solution (Figure 4.5a). Concerning the dimensions of the NPs, the precursor concentration increment caused the production of Ag particles with larger diameters Finally, an analogous diameter distribution can be observed in the substrates obtained by dynamic synthesis.

In order to further investigate the effect of varying the synthesis conditions by using a static approach, a series of experiments applying a gradually higher temperature were performed and combined with the increase of the concentration of silver nitrate.

Figure 4.6 shows the results obtained for the synthesis carried out using a 10 mM $AgNO_3$ solution at 20 °C (a), 40 °C (b), and 60 °C (c). The most noticeable effect of a temperature increment is indeed a broader and slightly red-shifted plasmonic dip as the temperature is raised, meaning that the fabricated particles are bigger and more heterogeneous. Such results are confirmed by the FESEM micrographs which show the production of bigger NPs for the sample synthetized at 60 °C with respect to the ones obtained at 20 °C.

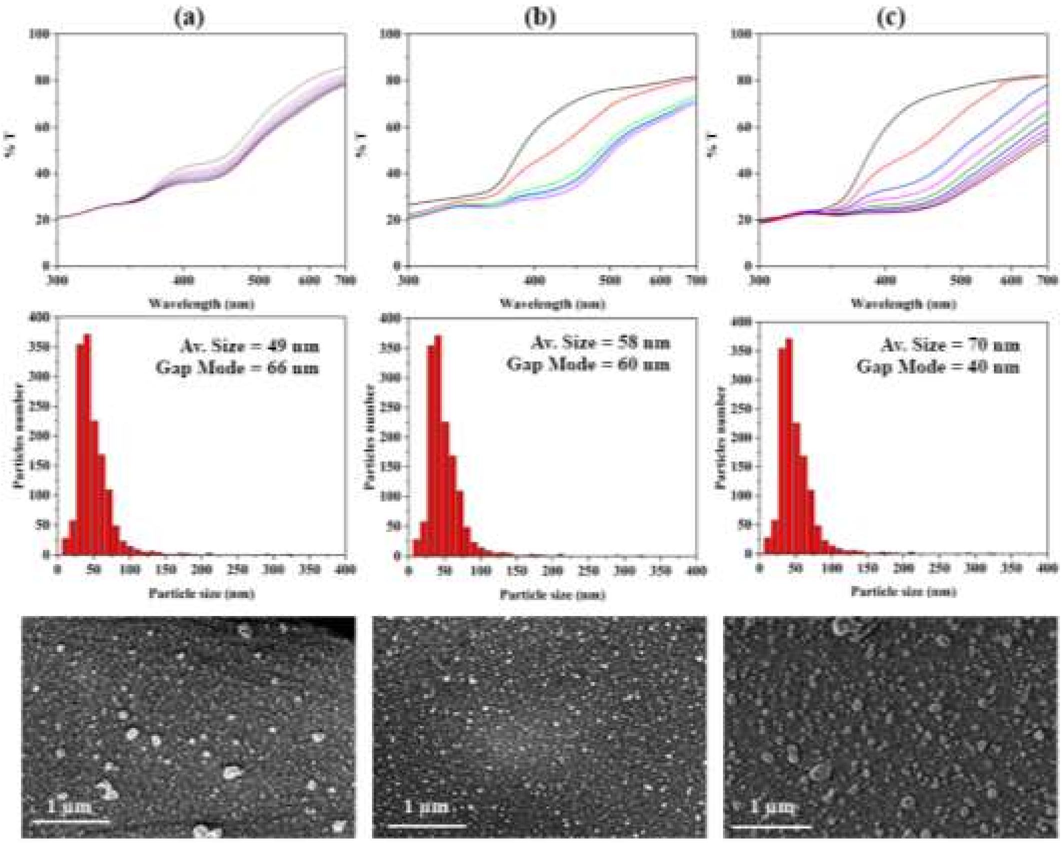

Figure 4.6 - UV-Vis transmittance spectra, particle size distribution, and FESEM micrographs for the samples synthetized in static conditions using a 10 mM $AgNO_3$ at a) 20 °C b) 40 °C and c) 60 °C.

Since using a dynamic approach, compared to the steady one, led to a more homogeneous distribution of the silver particle size, the effect of the flow rate has been investigated in order to better understand its role on the final shape and dimension of the NPs. Two additional experiments were performed, starting from a flow rate of 1 mL/min (Figure 4.7a) and increasing it respectively two (Figure 4.7b) and three times (Figure 4.7c). At a first glance increasing the flow rate seemingly reduces the reaction rate, despite a strong acceleration in the very first minute, as the transmittance decrement over time looks less homogeneous. Moreover, the plasmonic dip looks narrower in the samples synthetized with higher flow rate, meaning that more homogeneous nanoparticles should be expected. Indeed, the FESEM micrographs show a trend in the NP size, as it decreases as the flow rate increases, displaying a more homogenous distribution for higher flow rate and avoiding the formation of big aggregates. A further confirm is provided by the image analysis that reveals a smaller average size as the flow rate increases, as well as a more uniform particle size distribution.

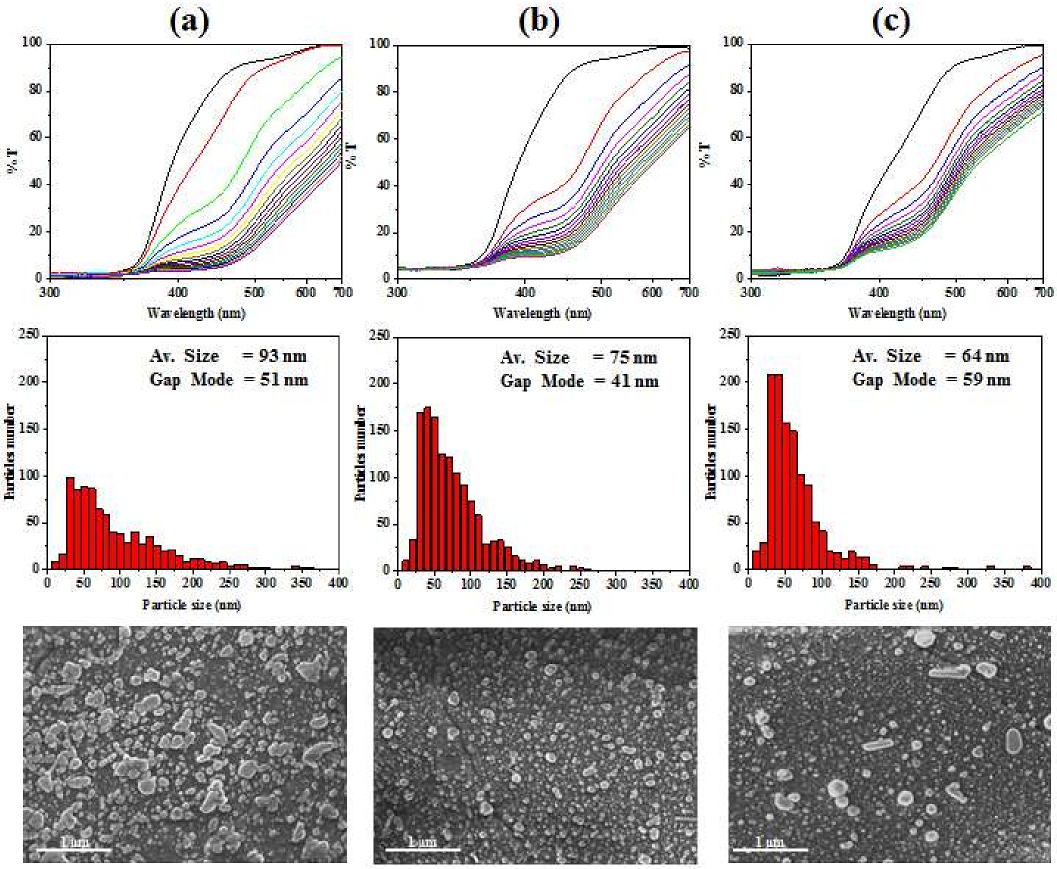

Figure 4.7 – UV-Vis transmittance spectra, particle size distribution, and FESEM micrographs for the samples synthetized in dynamic conditions using a 10 mM $AgNO_3$ at 20 °C employing a flow rate of a) 1 mL/min b) 2 mL/min c) 3 mL/min.

Once depicted the role of the flow rate the concentration of the silver nitrate solution was increased up to 100 mM, in order to understand its effect on the final NPs shape and dimension. Moreover, this rise of concentration was combined with a flow rate variation to comprehend the dependency on this two variables and their combined effect onto the final output, as shown in Figure 4.8.

As stated before, the increase of the silver nitrate concentration leads to an increased reaction rate as, especially in the first couple of minutes, the UV-Vis spectra are spectrally very different. Therefore, the saturation regime is reached faster. Since the plasmonic dip of each sample appears to be much broader and red-shifted compared to the ones belonging to the samples fabricated using a 10 mM silver nitrate solution, NPs with larger diameters and higher polydispersity are expected. Similarly, to the previous experiments, the hypotheses were confirmed thanks to the acquisition of FESEM micrographs. As a matter of fact, bigger silver particles are shown in the acquired images, underlining the main role of the silver precursor concentration as one of the main factor that lead to the fabrication of larger NPs. Instead, the effect of the flow rate variation is not as evident as in the previous series of samples. In fact, the average diameter of the NPs does not show a decrease as the flow rate increases, indeed its value remains fixed at around 100 nm. Nevertheless, a slight effect on the distribution of the particles is indeed observed since the sample fabricated using a 3 mL/min flow rate (Figure 4.8c) appears to be more homogeneous compared to the one synthetized applying a 1 mL/min flow rate (Figure 4.8a).

This set of experiments clearly showed the influence of both synthesis parameters on the final product and also highlighted their relative importance, as it has been observed that the effect the increase of the flow rate increase is largely overcome by a raise in the silver nitrate concentration

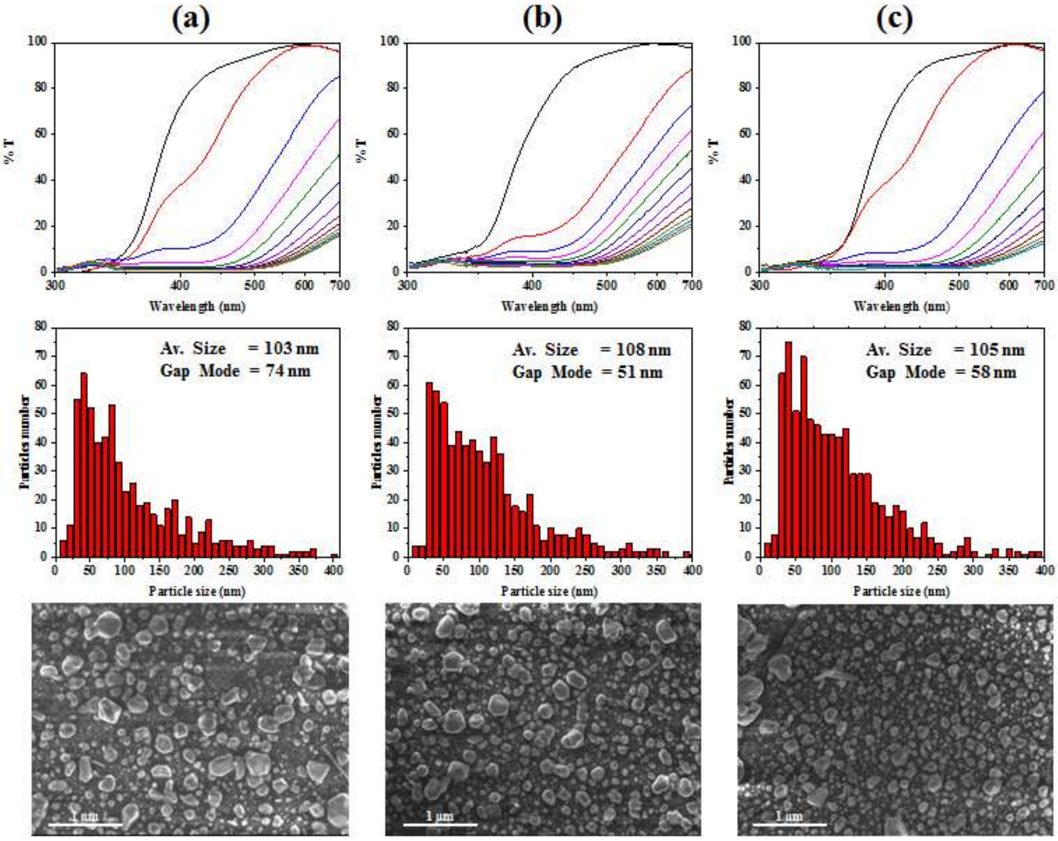

Figure 4.8 – UV-Vis transmittance spectra, particle size distribution, and FESEM micrographs for the samples synthetized in dynamic conditions using a 100 mM $AgNO_3$ at 20 °C employing a flow rate of a) 1 mL/min b) 2 mL/min c) 3 mL/min.

As last variable, the influence of temperature was studied ranging from 20 °C to 60 °C, combined with a variation of $AgNO_3$ concentration and flow rate variation. The obtained results show that the temperature is the main factor affecting the reaction kinetics, as a dramatic increase in the reaction rate is observed for both the samples fabricated with a 10 mM and 100 mM silver nitrate solution. Moreover, the temperature increase affects also the NPs growth, allowing the synthesis of bigger particles. Suh results are well highlighted by the comparison of the samples synthetized using a 10 mM $AgNO_3$ solution with a flow rate of 3 mL/min at different temperatures (Figure 4.9). Also in this case, it is clearly shown the increase of the NPs size as the temperature is raised. As drawback, the final distribution is more heterogeneous compared to the samples produced using lower temperature: this is probably due to the noticeable increase of the reaction rate, which inhibits a uniform distribution of the particles.

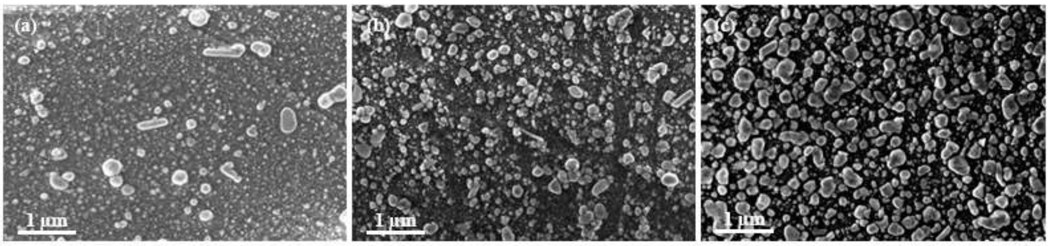

Figure 4.9 – FESEM micrographs of the samples synthetized using a 10 mM $AgNO_3$ solution with a flow rate of 3 mL/min and a temperature of a) 20 °C b) 40 °C c) 60 °C

Figure 4.10 and Figure 4.11 show the results obtained from two different sets of experiments, carried out using 10 mM and 100 mM $AgNO_3$ solution respectively at 60 °C, while the flow rate was varied, ranging from 1 mL/min to 3 mL/min. It can be observed that in both sets the reaction rate is strongly increased with respect to the equivalent synthesis performed at 20 °C (Figure 4.7 and Figure 4.8). Concerning the NPs size, the biggest differences are related to the samples in Figure 4.10 (10 mM $AgNO_3$). It is also interesting to notice that the average size is similar for both batches, as it varies from 101 nm to 145 nm, for substrates synthetized using a 10 mM $AgNO_3$ solution, and from 110 nm to 130 nm, for the samples produced using a ten time more concentrated solution of the silver precursor.

As a drawback the size distribution of the NPs it is not homogeneous as the samples previously displayed, as it is clearly noticeable from both the results of the image analysis and from the FESEM images themselves. Unfortunately, the effect of a flow rate variation that could have reduced the size dispersion is once more overpowered by the combined effect of the increased concentration and especially by the brutal impact of the temperature raise.

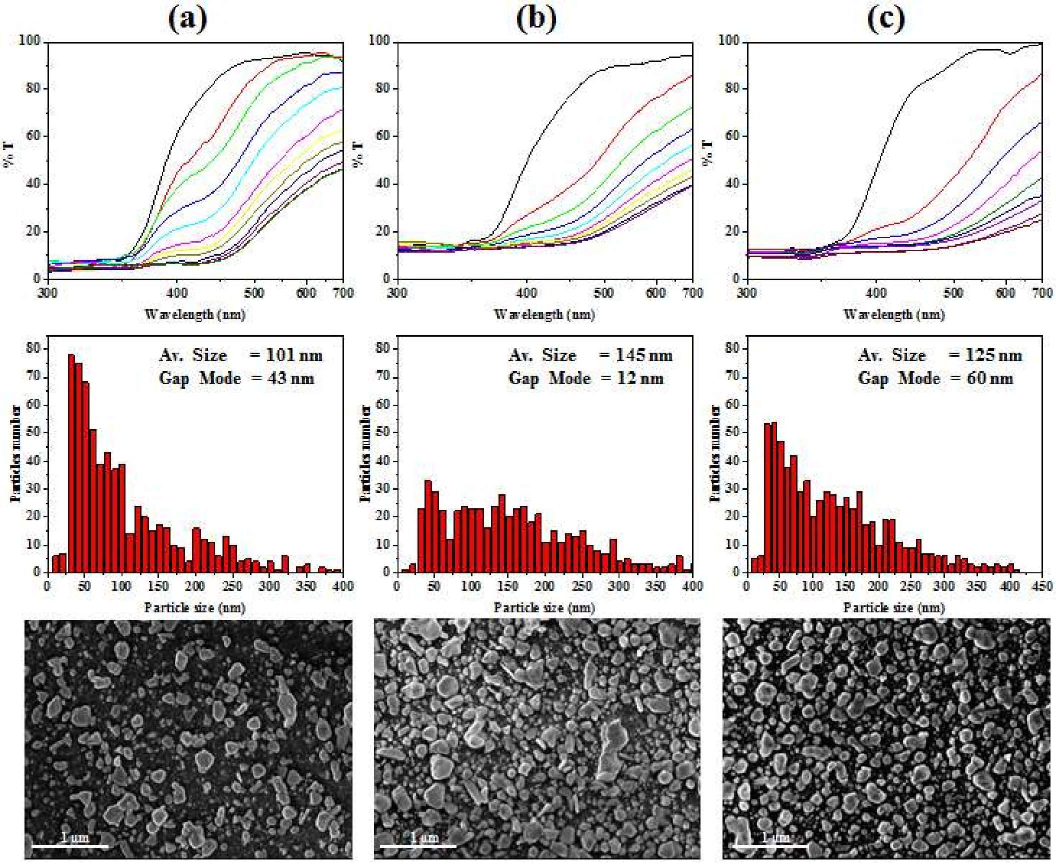

Figure 4.10 – UV-Vis transmittance spectra, particle size distribution, and FESEM micrographs for the samples synthetized in dynamic conditions using a 10 mM $AgNO_3$ at 60 °C employing a flow rate of a) 1 mL/min b) 2 mL/min c) 3 mL/min.

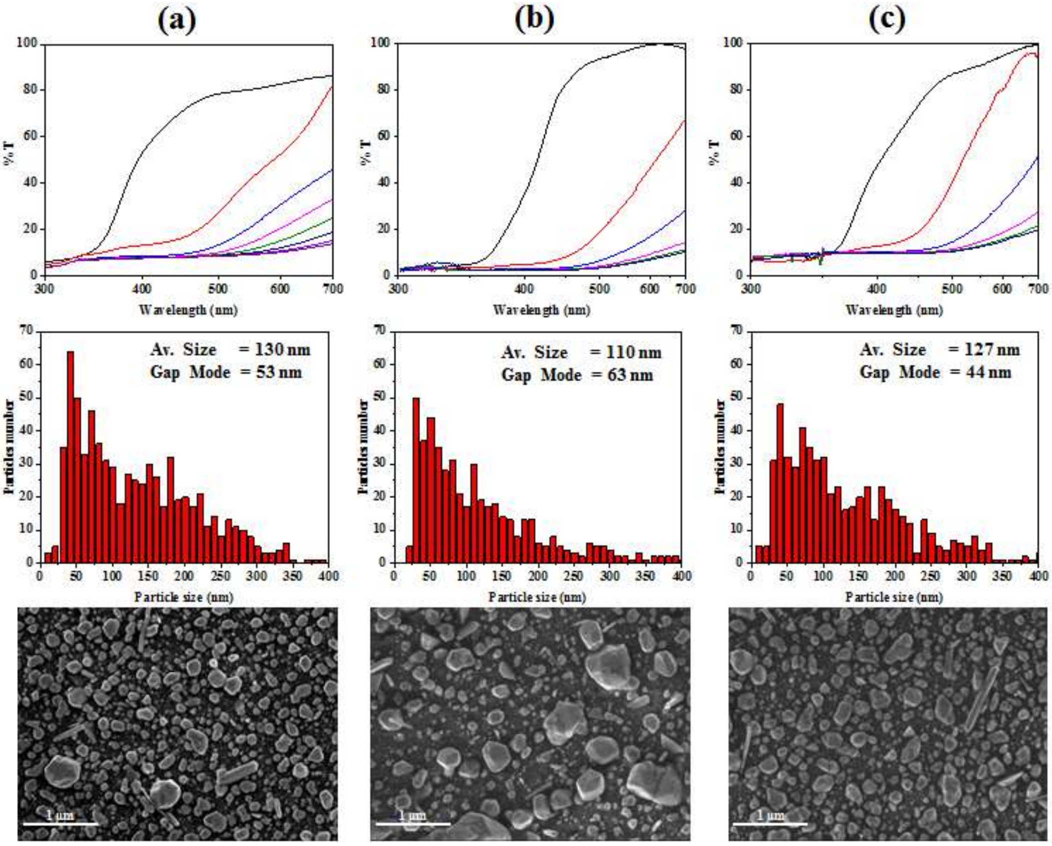

Figure 4.11 – UV-Vis transmittance spectra, particle size distribution, and FESEM micrographs for the samples synthetized in dynamic conditions using a 100 mM $AgNO_3$ at 60 °C employing a flow rate of a) 1 mL/min b) 2 mL/min c) 3 mL/min

4.3 SERS analysis

After having determined the effect of the main synthesis conditions on the NPs morphology, the SERS performances of each sample produced by the different combination of variables were tested. The goal was both to understand how the synthesis parameters could affect the SERS response of the substrates and to reveal if there is a correlation between a certain NPs morphology, their size distribution and the SERS response. To this aim, 4-mercaptobenzoic acid was chosen as probe in order to exploit the strong bond between its thiol group and the metal surface. Such characteristic allowed to rinse the samples after the incubation to prevent the formation of molecular aggregates that could affect the reproducibility of the SERS measurement. The SERS spectrum of 4-MBA is dominated by two main spectral components located at 1077 cm^{-1} and at 1584 cm^{-1}, both arising from the vibration of the aromatic ring [127,151], which could have been suitable for the SERS efficiency evaluation. In order to avoid any possible interference of other spectral components related to surface contaminants during the data analysis process, we choose to focus only on the peak at 1077 cm^{-1} (Figure 4.12). Indeed, the majority of the contaminants are carbon-based compounds whose SERS signals are mostly located in the 1300 – 1700 cm^{-1} range. Table 2 reports the labelling of the main spectral features of 4-MBA. The whole surface of each sample was analysed exploiting the streamline configuration of the Raman spectrometer, in order to maximize the information concerning both the SERS efficiency and the reproducibility of the samples, using a 1400 points grid-map.

Table 2 – SERS assignments of the 4-mercaptobenzoic acid (4-MBA)

Raman shift (cm^{-1})	**Assignment**	**References**
1077	ring breathing (ν 12, a1) + ν C-S	[151]
1137	δC-H (ν_{15}, b_2)	[152]
1180	δC-H (ν_9, b_1)	[152]
1380	COO^- stretching	[151]
1584	ring breathing (ν 8a, a1)	[151]

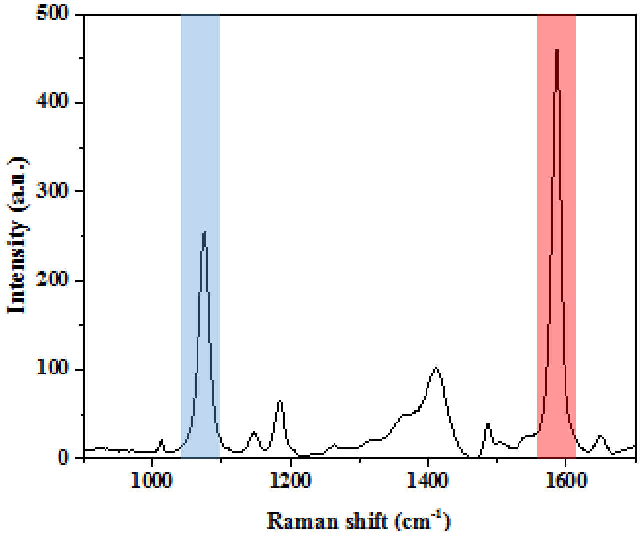

Figure 4.12 - SERS spectrum of a 1 µM 4-MBA. The spectrum is dominated by the highlighted bands at 1077 cm^{-1} and 1584 cm^{-1}, both related to ring breathing vibrations.

Since the enhancement of the Raman signal is related to both the nanoparticles size and, in particular, to the inter-particle gap, the last parameter (average gap) and its distribution can be a valuable issue for discussing the SERS efficiency of a specific substrate. In detail, the inter-particle gap size was calculated thanks to the image analysis protocol of the FESEM micrographs, as it has been previously done for the particle size distribution. Unfortunately, the results do not show a normal distribution of the gap size, as in Figure 4.13, causing the average gap size to be shifted towards higher value due to the contributions of bigger gap dimensions. This could cause a misrepresentation of the data because if is it true that bigger nanoparticles contribute more to the increase SERS signal, is indeed well known that the bigger SERS enhancement are achieved for the smallest inter-particle distance [14]. In order to obtain a more realistic information, the mode of the inter-particle size distribution was calculated instead of the average, which shows the most represented gap size in the distribution and allows a better comprehension of the Raman analysis result.

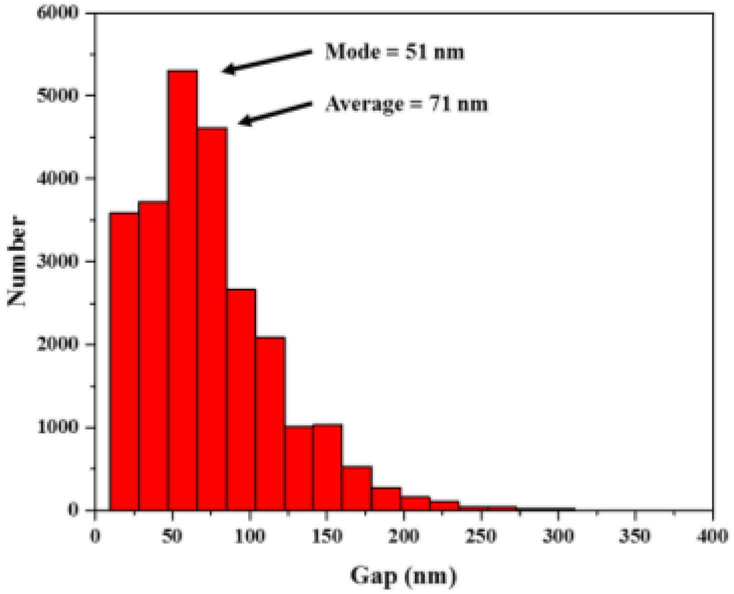

Figure 4.13 – Dimensions distribution of the inter-particle gap.

As mentioned before, the variation of the synthesis condition, especially concerning the combination of the variables that cause to an increase reaction rate, could lead to a certain heterogeneity in the distribution of the NPs on the porous silicon surface. This strongly affects the reproducibility of the SERS signal enhancement. Figure 4.14 shows the false colour map of the integrated area of the 1077 cm^{-1} peak of two different samples fabricated using the same $AgNO_3$ concentration (100 mM) and temperature (20 °C), but different flow rate, 1 mL/min (Figure 4.14a) and 2 mL/min (Figure 4.14b) respectively. Indeed, the strong heterogeneity of the sample manufactured using a lower flow rate is well represented by the %RSD value, whereas by increasing the flow velocity a more homogeneous distribution of the SERS signal intensity is reached. According to literature, the fluctuations of the SERS signal intensity in the range of 10-20% are usually considered a good result [122,153].

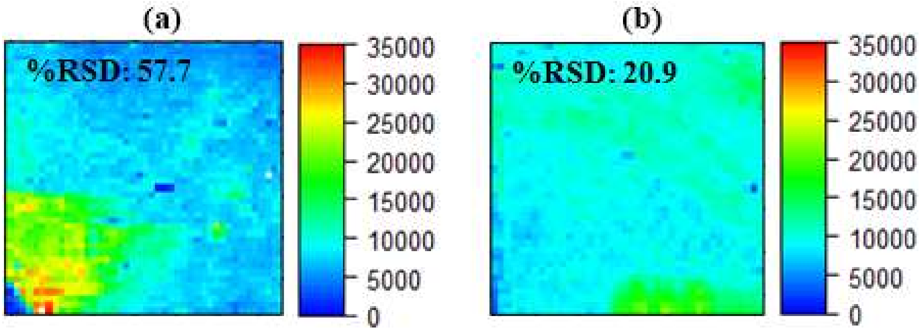

Figure 4.14 – False colour map of the integrated area of the 1077 cm^{-1} peak of samples produced using a $AgNO_3$ 100 mM solutions at 20 °C and a flow rate of a) 1 mL/min b) 2 mL/min.

Since specific synthesis conditions can cause deep differences concerning the nucleation and the growth of the silver seeds, leading to a wide range of particle and inter-particle distance distributions, a large spectrum of intensity and %RSD values should be expected.

Table 3 summarizes the results obtained from both the Raman analysis and the morphological characterization, while Figure 4.15 shows the intensity of the SERS signal vs its %RSD for each samples.

Table 3 – Summary of the SERS efficiency evaluation and of the image analysis results, obtained varying the synthesis parameters.

Number #	*[AgNO$_3$] (mM)*	*T (°C)*	*Flow Rate (mL/min)*	*Area (1077cm^{-1})*	*%RSD*	*Size (nm)*	*Gap (nm)*
1	10	20	0	7938	50.44	49.03	66.04
2	10	40	0	8073	30.80	68.76	59.97
3	10	60	0	8698	57.80	70.23	40.27
4	100	20	0	8362	21.15	100.37	44.31
5	100	40	0	6315	32.07	101.56	45.50
6	100	60	0	3167	37.55	71.69	48.65
7	10	20	1	6902	25.48	93.98	51.26
8	10	20	2	6996	34.28	70.62	40.78
9	10	20	3	1765	26.83	64.89	59.38
10	10	40	1	17576	40.45	86.82	43.85
11	10	40	2	18687	22.47	108.46	49.62
12	10	40	3	26321	43.34	94.06	39.35
13	10	60	1	12058	30.58	101.76	43.77
14	10	60	2	8844	15.70	145.26	12.66
15	10	60	3	8985	32.19	125.38	60.73
16	100	20	1	12163	57.56	103.82	74.32
17	100	20	2	12304	20.95	108.25	51.11
18	100	20	3	3482	22.40	104.69	57.70
19	100	40	1	4425	17.02	84.40	80.84
20	100	40	2	8690	28.86	116.73	42.27
21	100	40	3	7836	14.52	91.15	65.55
22	100	60	1	16972	20.10	130.49	53.59
23	100	60	2	7940	22.57	110.07	62.93
24	100	60	3	5039	32.30	127.25	43.84

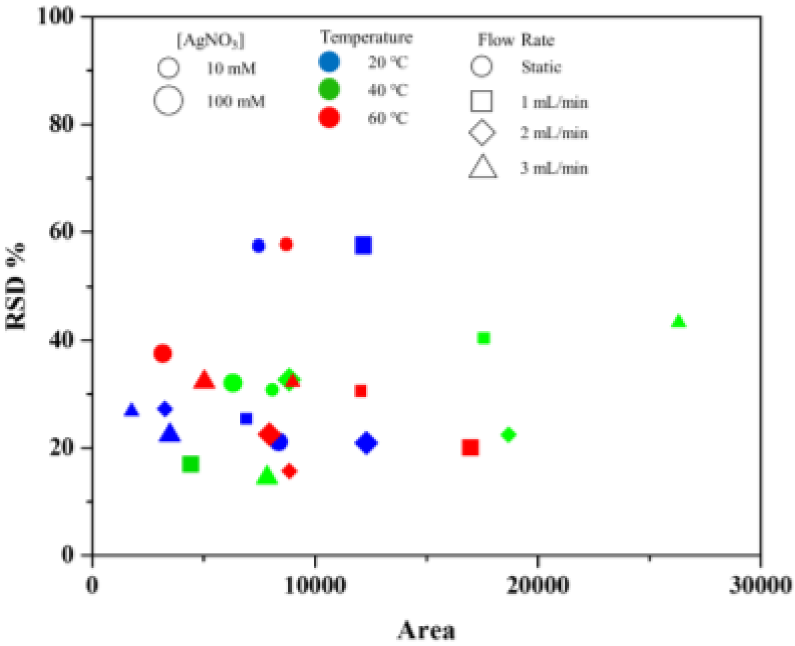

Figure 4.15 – SERS efficiency and reproducibility evaluation. The integrated area of the peak at 1077 cm^{-1} is plotted vs. the %RSD of the signal.

Even though at first glance the obtained data seems to be scattered among a wide range, without showing any correlation, a careful analysis of the effect of each variables can reveal specific trends in the data distribution. It can be noticed that, as stated before, the effect of a change in the flow rate is substantial only when other parameters that have a greater influence on the reaction, such as temperature and $AgNO_3$ concentration, are varied. Nevertheless, its role is easier to distinguish with respect to the morphological analysis. Concerning the substrates fabricated using a 10 mM $AgNO_3$ solution, a small increase in the flow rate seems to soften the effect of the temperature rise, which cause a faster reaction and the production of bigger but less homogeneous particles. With the only exception of the samples #8, a first increment of the velocity induces a decrease of the %RSD, meaning that the reaction proceeds in a more regulated way. A further increment though overturns the precedent effect and the %RSD of the SERS signal starts to increase again. A similar pattern can be observed for the temperature variation, where a first increment, from 20 °C to 40 °C, cause a huge increase in the intensity of the signal providing the most efficient samples in the whole series, while rising the temperature to 60 °C leads to a dramatic decrease of the efficiency. This behaviour can allegedly be ascribed to the increment of the reaction rate, especially as a consequence of the increased synthesis temperature, which could be responsible for the production of less uniform and less efficient samples.

This pattern is well highlighted by the data obtained from the series prepared at 40 °C, in which the combined role of the flow rate and the temperature is clearly noticeable on the SERS analysis outcome. The integrated area of the 4-MBA peak is much higher compared to the samples synthetized both at 20 °C and 60 °C and the reproducibility of these values varied as the flow rate increase, showing a first decrease as the velocity is doubled and a subsequent net increase when the velocity reaches the highest value (Figure 4.16). These data seem to be in agreement with the information provided by the analysis of FESEM micrographs (Figure A.2) which shows a less homogeneous particles distribution for both samples #10 and #12. Moreover, the SERS efficiency has to be related to the size of the silver NPs and to the presence of small inter-particle gap. Particularly concerning these last samples (i.e. 10 mM $AgNO_3$, 40 °C), the mode of the gap size distribution is centred around 40 nm whereas the average particle size ranges from 86 nm to 108 nm (Table 3). It is worth to notice that the highest particle size-gap ratio (S/G) belongs to the sample synthetized using the highest flow rate (Figure 4.16c), which is the most efficient samples of the batch, while the remaining samples display similar intensity and S/G values, suggesting a positive correlation between these two parameters.

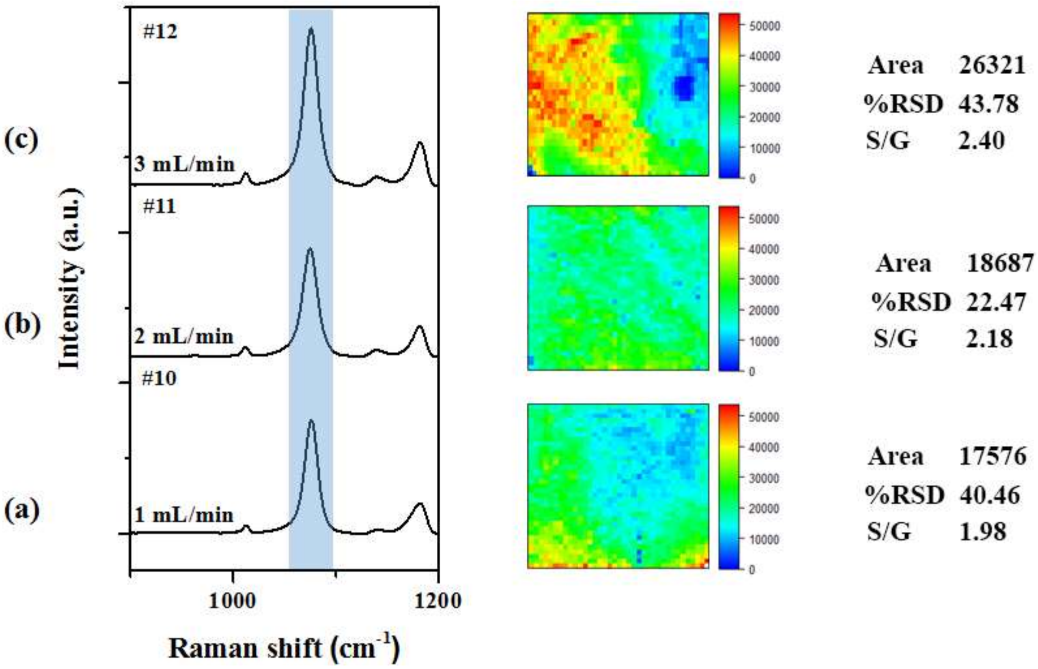

Figure 4.16 – SERS efficiency and reproducibility evaluation for the samples synthetized using a 10 mM $AgNO_3$ at 40 °C with a flow rate of a) 1 mL/min b) 2 mL/min and c) 3 mL/min. SERS spectrum and the related false colour maps of the integrated area of the 1077 cm^{-1} peak are reported on the left and in the centre, respectively. On the right side, the numerical value of the integrated area of the highlighted band and its %RSD along with the size-gap ratio obtained by the FESEM images, are reported.

Unfortunately, the substrates synthetized using an increased concentration of the silver precursor solution (100 mM) do not show such defined trend. The effect of a variation of the temperature does not seem to affect neither the intensity nor the reproducibility of the signal, whereas the rise of the flow rate shows conflicting results, as its effect is different for each temperature value. Samples fabricated at 20 °C display a huge decrease in the %RSD as the flow rate increases from 1 mL/min to 2 mL/min, while the subsequent increment doesn’t affect the reproducibility of the samples. On the contrary, the intensity of the signal is not affected using low or medium flow rate, while a dramatic decrease is observed for high flow velocity. These effects are probably related to the production of smaller NPs. Concerning the image analysis results the average size of the silver nanoparticles is bigger if compared to the ones produced using a 10 mM $AgNO_3$ solution.

Rising the temperature to 40 °C, the data do not display any trend that could match the previous findings, as doubling the flow rate leads to an increased SERS signal intensity as well as an increased %RSD value, whereas a further raise of the velocity seemingly softens the heterogeneity of the NPs size. A possible explanation for the low efficiency of the substrates could be related to the bigger size of the inter-particle gap, especially concerning samples #19 and #21, leading to higher S/G ratios.

The combined effect of both the temperature and the flow rate seems to show a dependency in the synthesis carried out at 60 °C (Figure 4.17), displaying a comparable trend with respect to the substrates synthetized using a $AgNO_3$ solution ten times less concentrated. It can be noticed that the rise of the flow rate causes a decrease in the intensity of the SERS signal together with an increment of the relative standard deviation. Using a high silver precursor concentration as well as high temperature and flow rate leads to a dramatic increase of the reaction rate causing a chaotic formation and evolution of the silver nanoparticle nuclei. The resulting samples show indeed bigger nanoparticles, with diameters ranging from 110 nm to 130 nm but the distribution is quite broad and the inter-particle size is difficult to estimate (Figure 4.11). The S/G ratio also shows conflicting results as the highest value is coupled to the lowest SERS signal (Figure 4.17c), even though there is probably a good correlation concerning the samples #22 (Figure 4.17a). These differences are due to the limits of the image analysis technique that is more likely to give a qualitative information rather than a quantitative one. Particularly concerning samples displaying several families of NPs with different dimensions, the optimization of the image analysis parameters can be challenging.

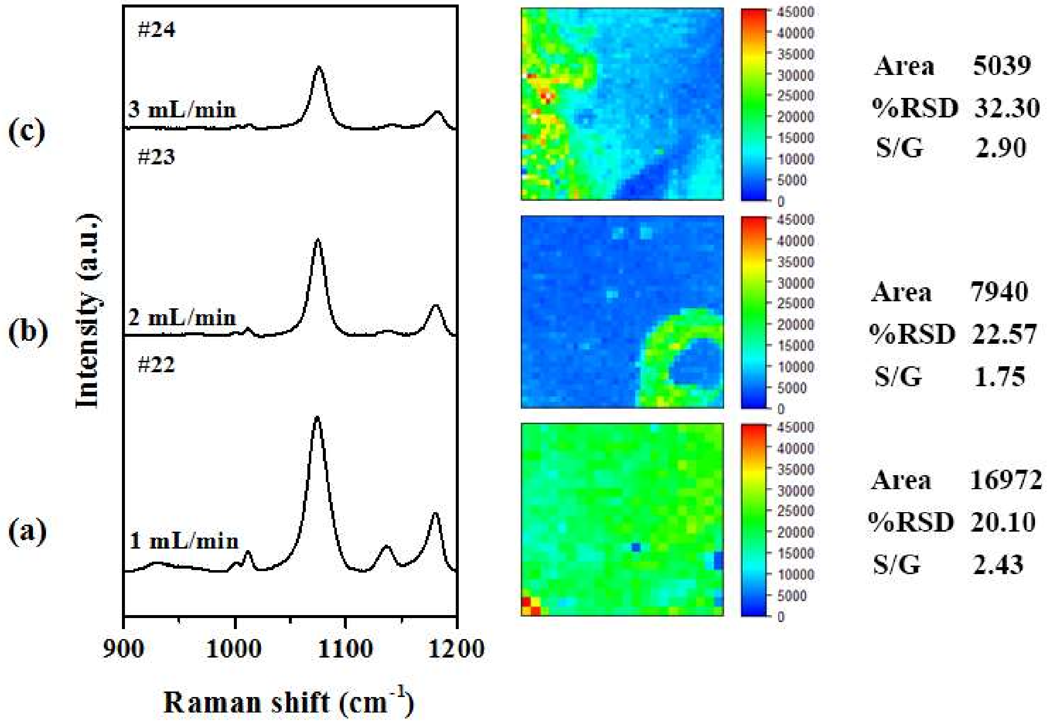

Figure 4.17 – SERS efficiency and reproducibility evaluation for the samples synthetized using a 100 mM $AgNO_3$ at 60 °C with a flow rate of a) 1 mL/min b) 2 mL/min and c) 3 mL/min. SERS spectrum and the related false colour maps of the integrated area of the 1077 cm^{-1} peak are reported on the left

and in the centre, respectively, of the graph. On the right side, the numerical value of the integrated area of the highlighted band and its %RSD along with the size-gap ratio obtained by the FESEM images, are reported.

Finally, concerning the substrates produced in static conditions it appears in fact that the only effect of the increment of silver nitrate solution concentration is to consistently lower the %RSD of the sample, whereas the temperature rise show different outcomes if combined with lower or higher $AgNO_3$ concentration. In the former case, the increment from 20 °C to 40 °C almost halves the %RSD, while a further increase shows an opposite effect as the samples is proven to be less homogeneous. Indeed, the FESEM micrographs confirm this trend, especially concerning the latter increment.

While the reproducibility of the samples is proven to be affected by the temperature variation, the SERS efficiency, calculated by means of the integrated area of the 1077 cm^{-1} peak, does not show any substantial differences. This is probably due to the wide range of dimensions of the inter-particle gaps whose size, in almost each cases, is comparable to the average particle diameters (Figure A.4).

At last, the temperature variation was combined with a 100 mM $AgNO_3$ solution, as shown in Figure 4.18. The variation of both the synthesis parameters did not positively affect neither the SERS efficiency nor the reproducibility of the signal, as the former displays a net decrease as the temperature rise while the latter exhibits an opposite trend. Moreover, the enhanced reaction rate leads to the growth of less ordered silver NPs that negatively affect the reproducibility of the SERS signal and therefore causes an increment, even though less evident than for previously reported conditions, of the %RSD.

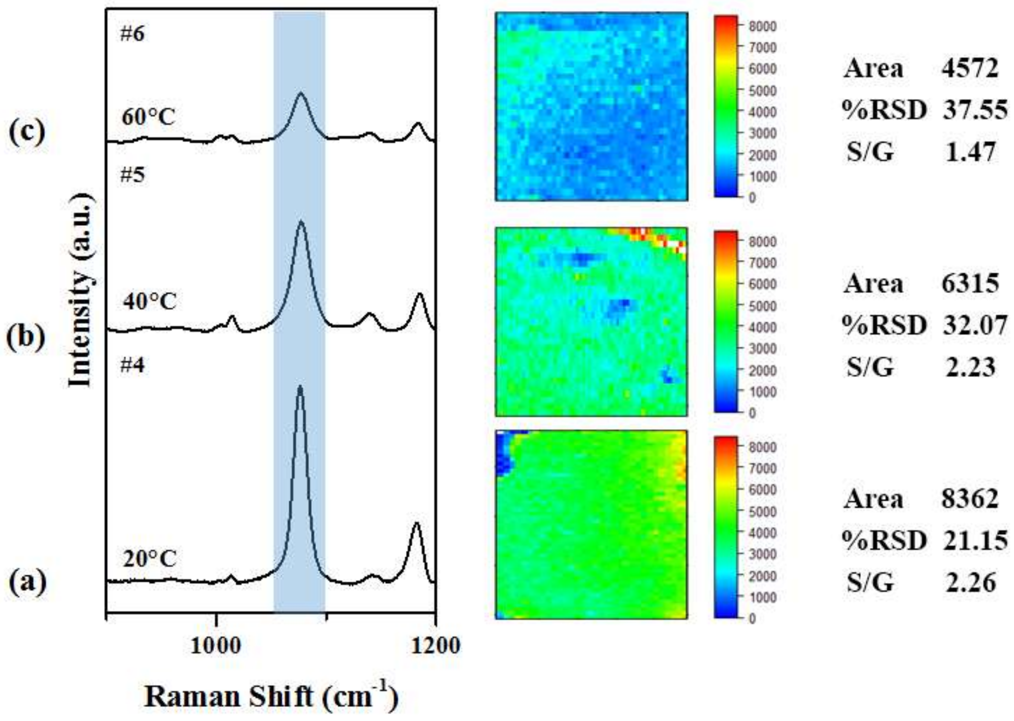

Figure 4.18 - SERS efficiency and reproducibility evaluation for the samples synthetized in static conditions using a 100 mM $AgNO_3$ solution at a) 20 °C b) 40 °C and c) 60 °C. SERS spectrum and the related false colour maps of the integrated area of the 1077 cm^{-1} peak are reported on the left and in the centre, respectively, of the graph. On the right side, the numerical value of the integrated area of the

highlighted band and its %RSD along with the size-gap ratio obtained by the FESEM images, are reported.

4.4 Conclusions

The goal of this chapter was to determine the effect of three main synthesis parameters on the growth and distribution of silver nanoparticles: i) the silver precursor concentration, ii) the temperature, iii) the flow rate.

In order to better control the variation of the parameters, a microfluidic approach was exploited, by hosting the pSi-PDMS membrane in a microfluidic cell, in which a silver nitrate solution was injected. Each synthesis parameter was then varied in order to understand its effect onto the optical and morphological characteristics of the obtained sample, thanks to the in situ UV-Vis monitoring of the LSPRs evolution and the image analysis of the related FESEM micrographs. Moreover, the SERS efficiency of each substrate was tested exploiting 4-mercaptobenzoic acid as a probe to evaluate the intensity and the repeatability of the SERS signal.

Thanks to such experimental protocol it was possible to determine the effect of each of the three selected variables on the reaction outcome, and the relationship among them. It was noticed that the temperature increment has the strongest effect, leading to an increased reaction rate and to the production of bigger nanoparticles. The drawback of such fast kinetic was a broader distribution of the silver particle size and thus the production of less homogeneous samples from the morphological point of view. A similar result was obtained rising by ten time the concentration of the silver precursor, which in most of the cases caused an increment of the nanoparticles dimensions. Finally, the flow rate showed to be the less effective of the three synthesis parameters, whose influence was often overcome by the result of the temperature and concentration variation. The flow rate modification displayed an opposite impact with respect of the other two parameters, as the nanoparticles grew smaller and more uniform as the velocity was risen.

Concerning the SERS analysis, some trends were highlighted, showing a correlation between the SERS results and the morphologies of the related substrates. The most evident patterns are related to the synthesis carried out using a 10 mM $AgNO_3$ solution, in which a moderate flow rate increment mitigates the effect of the temperature rise, as revealed by the decrease of the relative standard deviation of the SERS signal. Nevertheless, a further increase of the flow rate, up to 3 mL/min, combined with high temperature, caused an increment of the %RSD. Concerning the samples synthetized using a higher silver nitrate concentration, the results are not very well correlated with the synthesis parameters variation. Unfortunately, the reliability of the FESEM micrographs analysis could be negatively affected by the morphology complexity. The only observed trend is related to the series fabricated at 60 °C using different flow rates, in which a consistent decrease in the signal intensity together with a rise of the %RSD, is displayed as the flow rate is increased. In conclusion, an increase of the silver precursor concentration coupled with a mild temperature raise and a moderate flow rate often led to the fabrication of homogeneous samples, whereas pushing the synthesis conditions has been proven to be detrimental for both the SERS efficiency and homogeneity of the substrates. Interestingly, the most efficient sample has been obtained using a low silver nitrate concentration, alongside with a moderate temperature increase (40 °C) and a strong flow rate. Such result is probably due to the development of very narrow inter-particle gaps, which are responsible for the SERS signal increase.

Chapter 5

5 SERS bioapplications

In this chapter the Ag-PSD samples were exploited for the development of a bioassay for the selective detection of miR222, and for the discrimination of different bacterial strains. To this aim, the Ag-PSD substrates were produced by immersion plating using thicker pSi membranes. These substrates have been proven to provide a good intra and inter substrates reproducibility allowing the development of reliable sensing platforms. In the following section a brief discussion about the fabrication protocol and the SERS performances of such silvered porous silicon substrates is provided.

5.1 Immersion plating of pSi-PDMS substrates

Porous silicon membranes with a ~2 μm thickness were produced by electrochemical etching of boron doped silicon wafers. The obtained layer was then detached and transferred onto a PDMS slice obtained by mixing a PMDS precursor with a curing agent with a 10:1 ratio [119]. The silver nanoparticles are synthetized by means of immersion plating, dipping the obtained pSi-PDMS (PSD) membranes into a 10^{-2} M silver nitrate solution, after a refresh step performed in HF.

From the analysis of the FESEM micrograph shown in Figure 5.1a a highly packed and homogeneous distribution of particle is revealed, with an average size of around 30 nm.

In order to test the SERS efficiency of the Ag-PSD samples, R6G and 4-MBA were exploited as molecular probes, taking advantage of their different characteristics. Indeed, resonant Raman conditions can be exploited using R6G, thanks to an intense absorption band at around 520 nm (Figure 5.1b), allowing the detection of very low concentrations, whereas a more homogeneous and stable distribution of molecules can be achieved using 4-MBA, thanks to the strong thiol-metal bond. As shown in Figure 5.1c, ultra-low R6G concentrations were detected, as its vibrational pattern is still recognizable down to 10^{-14} M concentration. Concerning the reproducibility of the SERS signal, a %RSD of 12-15% was obtained by the analysis of samples incubated with 4-MBA, as shown by the false colour map of the integrated area of the 1584 cm^{-1} 4-MBA peak (Figure 5.1d). Such result indicates a good spatial homogeneity of the synthetized silver nanoparticle and thus of the provided SERS enhancement.

.

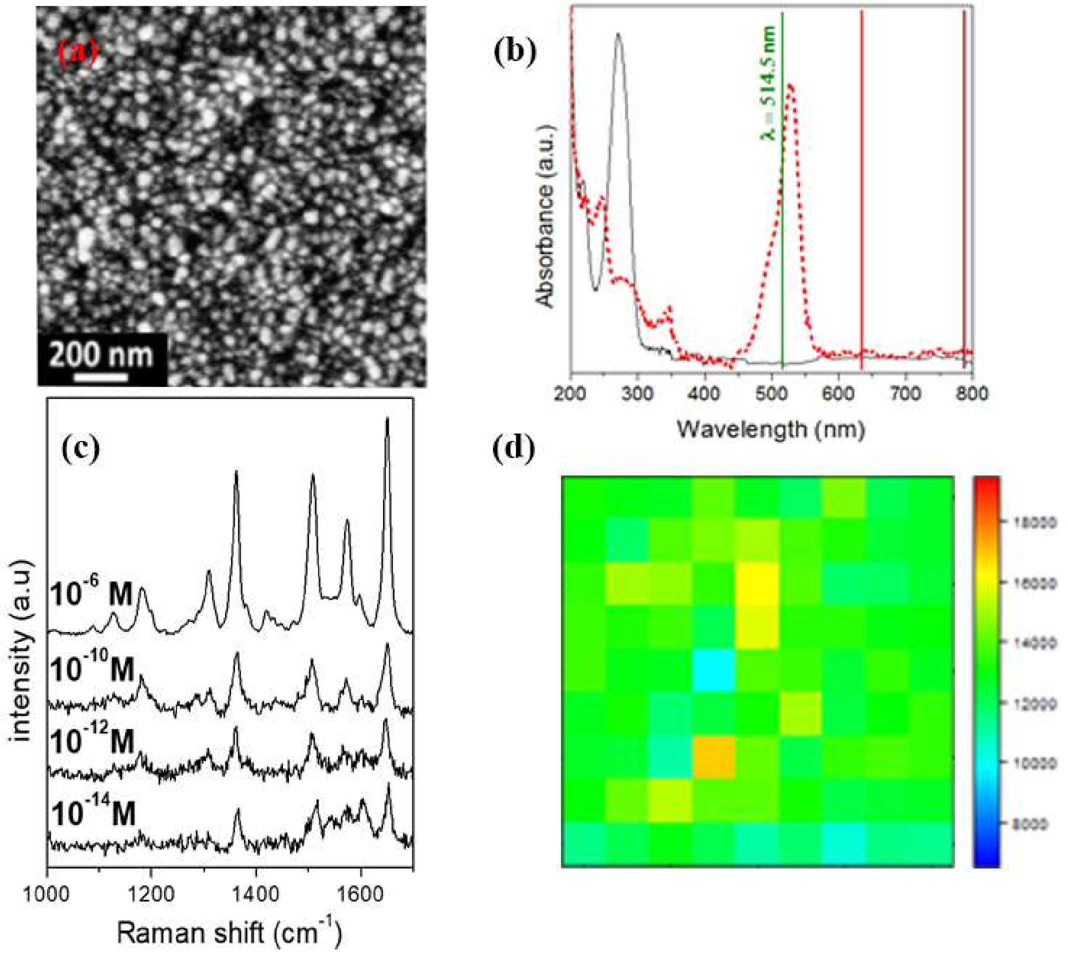

Figure 5.1 – a) FESEM micrograph of the Ag coated pSi-PDMS membranes b) Schematic representation of the Ag-PSD architecture c) SERS spectra collected from Ag-PSD samples at several R6G concentrations c) False colour maps of the fitted area of the 4-MBA 1584 cm^{-1} band.

5.2 miRNA detection

The content of this section has been partially published in the following paper:

[83] Novara, C.; Chiadò, A.; Paccotti, N.; Catuogno, S.; Esposito, C. L.; Condorelli, G.; De Franciscis, V.; Geobaldo, F.; Rivolo, P.; Giorgis, F. SERS-active metal-dielectric nanostructures integrated in microfluidic devices for label-free quantitative detection of miRNA. *Faraday Discuss.* **2017**, *205*, 271–289, doi:10.1039/c7fd00140a

5.2.1 Introduction

In this chapter, Ag-PSD substrates integrated in a microfluidic chip were exploited for the detection of miRNAs. In particular, for these initial tests we focused on the detection of miR222 because of its involvement in numerous neoplastic disease, such as brain, lung, prostatic, liver, and pancreatic cancer [154–156]. To this aim, two assays were designed and compared. The first protocol concerns the functionalization of the metallic NPs surface with a thiol capped DNA probe enabling the selective recognition of the target miRNA. In this case, the probe is a full-complementary sequence with respect to the miRNA of interest. This protocol was previously developed also as an enzyme-linked immunosorbent assay (ELISA) for metal-dielectric structures [119]. On the other side, the second approach takes advantage of a label-free detection of miRNAs, in which the probe is divided in two halves, namely half1 and half2. The first half-probe is immobilized on the metal surface enabling the capture of the target miRNA, while the half2, which is labelled with a Raman reporter, allows the SERS detection in a second hybridization step. Indeed, the former approach could theoretically allow the label-free detection of the targeted miRNA, exploiting its vibrational pattern, but the similarities of both the probe and miRNA fingerprints could lead to some practical concerns in the SERS detection. On the contrary, the latter protocol can overcome these issues taking advantage of the clear and intense fingerprint of the Raman label, also avoiding any chemical modifications of the target. Nevertheless, to allow a direct comparison between the results obtained using the two different protocol, a labelled miRNA was exploited for the one-step protocol. Cyanine 5 (Cy5), Cyanine 3 (Cy3), and Rhodamine 6G (R6G) were exploited as Raman labels, to investigate the effect of different dyes. Indeed, using a laser line at 514.5 nm for Raman excitation, Cy5 exhibits the lowest fluorescence background, that can be detrimental for the spectra analysis, while using Cy3 and R6G, resonant Raman conditions can be exploited.

A careful optimization of each step of the assay has been carried out in order to maximize the amount of hybridized molecules. A schematic representation of the two different assays is shown in Figure 5.2.

Furthermore, the effect of different positions of the Raman dyes along the probe was invesigated, in order to further enhance the SERS sensitivity. To this aim calibration curves were prepared incubating the samples with different concentrations of miRNA allowing the determination of the LODs. The two-step assay was then used to specifically detect the miR222 mixed with other synthetic miRNA. Finally, the two-step assay was exploited to determine the target miRNA concentration in cellular extracts, in order to avoid complex and expensive chemical processes aimed to label the micro-RNA sequences.

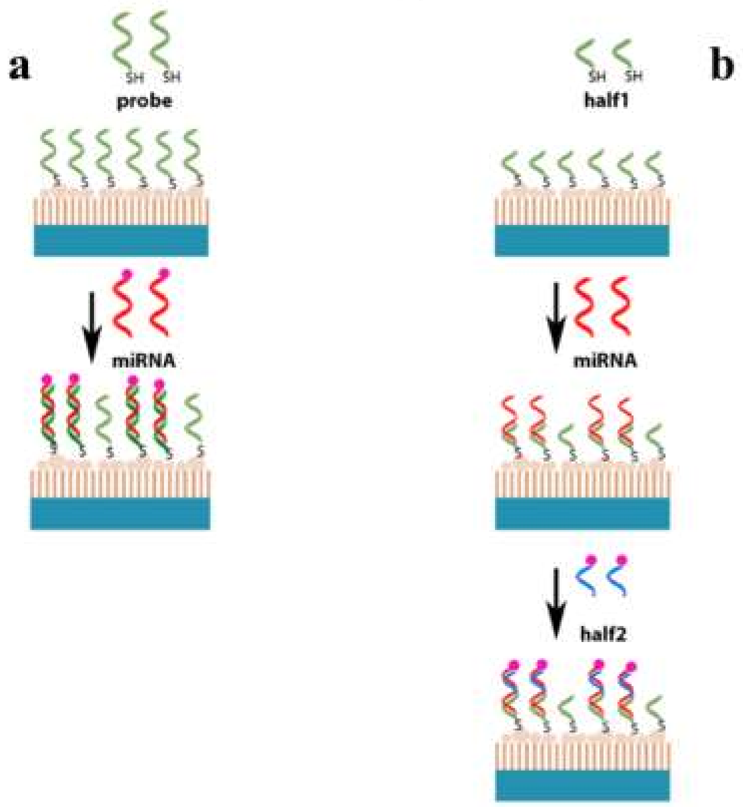

Figure 5.2 – Scheme of the a) one-step hybridization assay and b) two-step hybridization assay.

5.2.2 Bioassay optimization

The functionalization of the Ag-PSD substrates surface for both the one and the two steps bioassays requires a fine-tuning of the probe immobilization and hybridization conditions. Due to the different probe length and probe-miRNA interactions the optimal conditions are expected to be peculiar for each assay. To refine the protocol, the optimization of each step was supported by means of SERS spectroscopy, providing insights in the interactions taking place on the sample surface.

The first step was designed to evaluate and therefore to minimize the non-specific binding due to the interaction between the target miRNA and the surface. In this context, the non-specific binding refers to an interaction of the target molecule with the SERS active surface that is not mediated by the designated receptor. To this aim SERS substrates were pre-treated with BSA, as in the previously developed protocol [119], and subsequently incubated with a CyX (X = 3, 5) labelled miRNA/half2, avoiding the functionalization of the surface with the probe. As stated in the previous paragraph, Cy5 was used due to its lower fluorescence background, while using Cy3 allows to exploit resonant Raman conditions. After 1 hour of incubation, the samples were washed using the same buffer employed for the previous step. Due to the differences mentioned above, the composition of the applied buffers was varied analysing the one-step and two-step assays. Indeed, in the latter case a higher ionic strength (namely four times higher) is required for the washing step because of the lower number of base pairs formed between half1/half2 and the target miRNA that decreases the melting temperature of the complex.

Figure 5.3 shows the main results of this test. The spectra collected on substrates without any blocking treatment of the surface are reported on top of each series, as reference, and appear dominated by the vibrational modes of the Raman reporters. The Cyanine-based dyes employed exhibit indeed a clear vibrational fingerprint, whose most intense bands are related to the C=N stretching of the ring atoms, located at 1589 cm^{-1}, to the CH_3 deformation of the ring substituents, at 1463 cm^{-1}, and to the methine chain vibration, located at 1388 cm^{-1} for Cy3; for such a band, a shift to 1352 cm^{-1} is observed for Cy5, due to the greater length of the chain. As clearly seen, there is a concrete need for a pre-treatment step to avoid the non-specific binding. This could be minimized increasing the surfactant concentrations in the incubation buffers, even though an excessive increment could negatively affect the specific hybridization: therefore, a compromise should be found. As shown in Figure 5.3 (black curves), adding a passivation step based on BSA before incubating the samples, leads to a decrease of the signal of the labelled target, regardless of the used protocol as well as the surfactant concentration. A similar result is obtained by adding a surfactant such as tween or SDS to the washing buffers, as it can be noticed comparing the spectra obtained for miRNA-CyX incubated in SSC 1x or SSC 4x with the ones collected using the same buffers supplemented with a 0.01% of SDS. The same results are recorded for the half2, using an incubation buffers with SSC 1x or SSC 4x, despite a higher non-specific signal probably due to the smaller size of the shorter sequences. It is worth to notice that the vibrational fingerprint of the half2-Cy3 complex is still recognizable even after washing in SSC 4x SDS. Such persistent phenomenon is probably due to the resonant excitation of the Cy3 reporter rather than to a higher surface affinity compared to the Cy5, taking into account the excitation at 514.5 nm. In such conditions, the electronic resonance of the Cy3 is exploited, leading to a further increase of its Raman scattering efficiency. For the same reason, a lower LOD could be achieved for the half2-Cy3/miRNA complex detection. To address the issue related to the persistence of the half2-Cy3 fingerprint, the SDS was replaced with 0.05% tween and BSA at 1% concentration was added to the washing buffer. This was then used to rinse the samples after the half2 incubation step, effectively reducing the SERS signal of the label (Figure 5.3b at the bottom).

This first phase pointed out the need of a surface blocking step of the PSD samples as well as the enhanced performances of the washing buffers supplemented with surfactants.

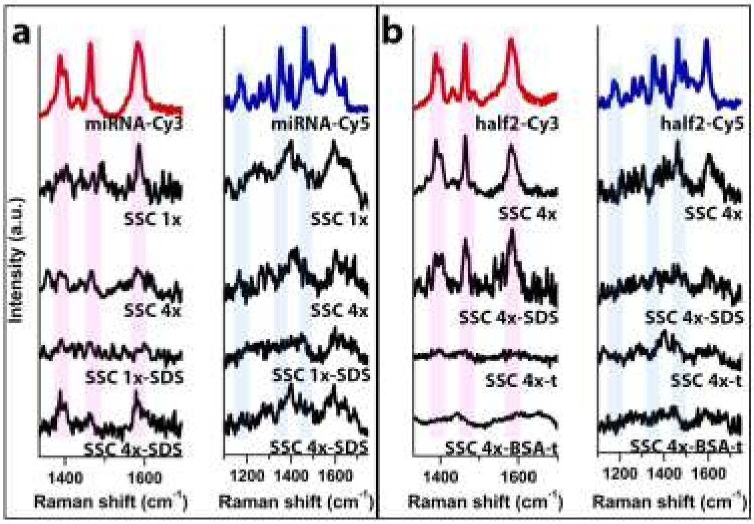

Figure 5.3 – a) One step assay non-specific SERS signal evaluation for labelled miRNA-Cy3 (left) and miRNA-Cy5 (right). Different buffer compositions were: from the top to the bottom SSC 1x, SSC 4x, SSC 1x 0.01% SDS, SSC 4x 0.01% SDS. b) Two step assay non-specific SERS signal evaluation for labelled half2-Cy3 (left) and half2-Cy5 (right). Different buffer compositions were: from the top to the bottom SSC 4x, SSC 4x 0.01% SDS, SSC 4x 0.05% tween, SSC 4x 0.05% tween 1% BSA. Incubation and washing steps have been carried out using the same buffers composition. Reference spectra are shown on the top of the graphs (red and blue curves). The displayed spectra are offset to clarify the representation.

Once addressed the non-specific binding issue, the focus was devoted to the optimization of the probe concentration as well as the ionic strength of the immobilization buffer, in order to maximize the subsequent hybridization with the miRNA and the related SERS signal intensity. The probe surface density has indeed an ambiguous role, since it should be as high as possible to maximize the number of hybridization sites, but it could be also responsible for a decrease of the SERS signal of the miRNA/half2 in case of an excessively tightly packed probe monolayer, due to the steric hindrance that limits the pairing between the probe and the target. As previously shown for the non-specific binding concern, SERS spectroscopy provides a simple and reliable method for the evaluation of the optimal probe surface density.

At first, both the probe222 (one-step assay) and the half1 (two-step assay) were incubated in a concentration range from 1 to 50 µM (TE, 1 M NaCl). Figure 5.4 shows the results of the probe222 SERS analysis. Typical vibrational features of the nitrogenous bases already appear at 1 µM, emerging from the SERS background signal due to the presence of BSA. Their main bands are related to the ring breathing modes of adenine (730 cm^{-1}), cytosine, and thymine (790 cm^{-1}), the adenine ring stretching (1325 cm^{-1}), the guanine bands related to the C-N stretching, and N-H bending (1480 cm^{-1}, and 1580 cm^{-1}), and finally to an adenine related shoulder due to the scissoring of the amino group (1577 cm^{-1}). A distinct band located at around 1640 cm^{-1} is related to the carbonyl stretching of the pyrimidine bases, while less intense peaks at 1030 cm^{-1} and 1096 cm^{-1} have been assigned to the deoxyribose and PO_2^- stretching modes, respectively. Concurrently, as the probe222 concentration is raised, the BSA related background, characterized by the bands located at 1660 cm^{-1} (amide I), 1452 cm^{-1} (deformations of proteins side chains), 1001 cm^{-1}, 1203 cm^{-1}, 1370 cm^{-1}, and 1614 cm^{-1} (aromatic amino acids), decreased. A certain surface saturation is indeed observed using concentration higher than 25 µM, as clearly shown in Figure 5.4b, in which the integrated area of peak at 790 cm^{-1} is plotted vs the probe concentration.

Subsequently, the samples were incubated with a 1 µM miR222-Cy5 buffer solution, as shown in Figure 5.4c, where the entire vibrational pattern of Cy5 is clearly recognizable even for the lowest probe concentration. The highest signal is obtained for the samples incubated with a 25 µM probe solution, meaning that the maximum hybridization is achieved, whereas the signal intensity decreases if the probe concentration is further raised. This pattern is highlighted also by the integrated area of the 552 cm^{-1} peak displayed in Figure 5.4d. The optimal probe density is therefore achieved using a 25 µM probe solution concentration.

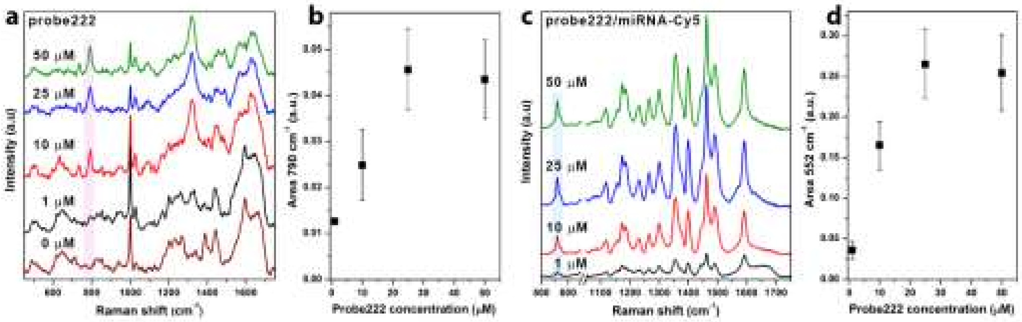

Figure 5.4 – Optimization of the probe222 surface packing. a) SERS spectra acquired from samples incubated with different concentration of probe222. Reference spectrum (brown curve) was collected from the sample incubated with BSA b) Fitted areas of the 790 cm^{-1}probe band plotted against the probe concentration. c) SERS spectra collected from the samples incubated with 1 µM of miR222-Cy5. d) Fitted areas of the 552 cm^{-1} miRNA-Cy5 SERS plotted against the probe222 concentration. The error bars represent the SD of the fitted spectra. The displayed spectra are offset to clarify the representation.

The same conditions were applied to evaluate the optimal probe density for the two-step assay, allowing the comparison between the two protocols. Figure 5.5 reports the spectra collected after the incubation of different concentration of half1. It is worth to notice that even though it is composed by only 10 nucleotides, the detectable vibrational features are comparable to the ones belonging to the previously analysed probe222, featured by additional 12-nucleotides. Such result indicates that the SERS vibrational pattern is provided by the same components of the oligonucleotidic chains and therefore, that the probe molecules are vertically oriented over the Ag surface. Nevertheless, a small amount of tilted molecules cannot be excluded, even though their contributions to the vibrational pattern does not appear to be relevant. Moreover, it is known that long probes (more than 100 nucleotides) can bend towards the surface [157]. In our case the length of the probes does not exceed 22 nucleotides and no differences between the different spectra are recorded, and therefore a further interaction between the nucleobases and the surface is negligible. As for the previous test, the saturation regime is achieved using a 25 µM half1 solution concentration, for which the integrated area of the 790 cm^{-1} peak reaches its maximum (Figure 5.5c). Afterwards, the samples were incubated with a 1 µM miR222/Cy5 solution, allowing the comparison between the one-step and the two-step assay. Figure 5.5d shows that the highest SERS signal is attained for a probe concentration of 10 µM, whereas for higher concentration the signal does not display a significant increment, reaching a saturation regime, and for the lower ones a decrease is observed. Such results indicate that a 10 µM probe concentration is therefore ideal for the half1 immobilization.

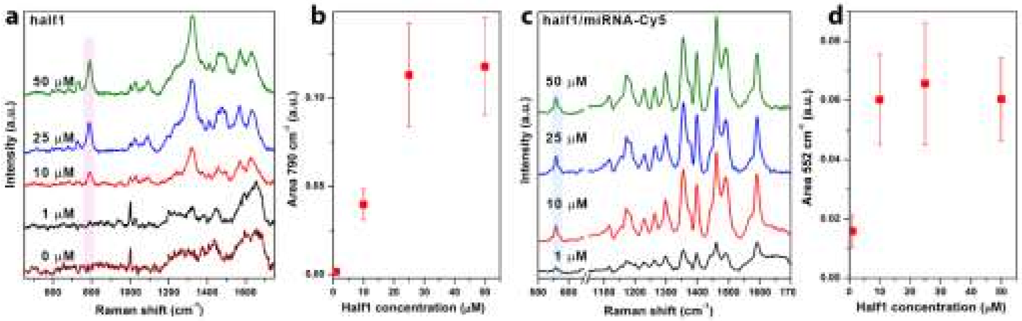

Figure 5.5 – Optimization of the half1 surface packing. a) SERS spectra acquired from samples incubated with different concentration of half1. Reference spectrum (brown curve) was collected from the sample incubated with BSA. b) Fitted areas of the 790 cm^{-1}probe band plotted against the probe concentration. c) SERS spectra collected from the samples incubated with 1 µM of half1-Cy5. d) Fitted areas of the 552 cm^{-1} half1-Cy5 band plotted against the half1 concentration. The error bars represent the SD of the fitted spectra. The displayed spectra are offset to clarify the representation.

Finally, in order to attain an optimal packing of the probe on the substrate surface, the negative charges of the phosphate groups in the nucleotides need to be shielded to lower the electrostatic repulsion between different strands. A certain amount of salt is then required in the buffer solution.

As for the evaluation of the non-specific binding and the optimal probe density, SERS spectroscopy was exploited to assess the ideal salt concentration in the immobilization buffer for both the one-step and the two-step assays. To this aim, the probe222 and the half1 were incubated on the substrates in TE added buffer with increasing NaCl concentration and analysed. Figure 5.6 shows that the intensity of the probe222 characteristic bands increases as the NaCl concentration raises, without apparently reaching a surface saturation. To test the efficiency of each condition the same samples were subsequently incubated with 1 µM miR222/Cy5. Despite the trend displayed by the immobilized probe spectra, the better hybridization efficiency is obtained for the 1 M NaCl concentration (Figure 5.6d, f, black squares), as confirmed by the integrated area of the 552 cm^{-1} peak of the target label. Such results suggest that a surface featured by excessively packed probe molecules, due to the high salt concentration, might lead to a decrease of the hybridization efficiency, as expected.

The same procedure was applied to test the probe packing for the two-step assay. Similarly to the results obtained for the one-step assay, the collected spectra show a monotonic increase of the half1 bands along with the ionic strength, without reaching the saturation regime (Figure 5.6b). Equally, the highest signal for the miRNA hybridization is achieved for 1 M NaCl, as confirmed by the integration of the 552 cm^{-1} peak of miR222/Cy5 in Figure 5.6f (red dots). Even though the maximum amount of immobilized half1 is obtained using the same ionic strength, its immobilization is achieved at lower salt concentration compared to the probe222, as shown in Figure 5.6c (red dots). This phenomenon is probably due to the longer chain of the probe222 that requires more ions to solvate the negative charges of the probe backbone. Such results are in agreement with the outcomes previously reported (Figure 5.4, and Figure 5.5), showing that a lower concentration (10 µM) of half1 is required to attain the ideal surface density with respect to the probe222 (25 µM). SERS analyses finally confirmed the presented results highlighting that the optimal probe surface density required to obtain the highest hybridization with the miRNA is reached before the saturation regime.

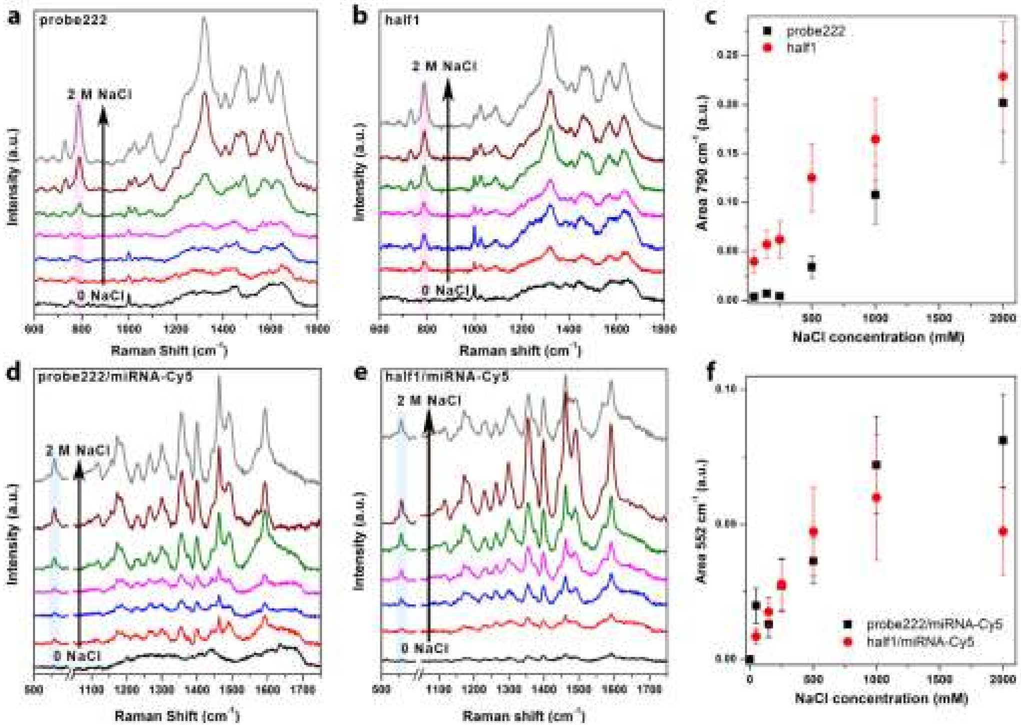

Figure 5.6 – Optimization of the buffer saline concentration. a) SERS spectra collected from samples incubated with 25 µM probe222 using different NaCl concentrations; b) SERS spectra collected from the samples incubated with 10 µM half1 using different NaCl concentrations; c) Fitted areas of the 790 cm^{-1} probe222 (black squares) and half1 (red dots) peak plotted against. the NaCl concentration; d) SERS spectra of the samples in Figure 5.6a incubated with 1 µM miR222-Cy5; e) SERS spectra of the samples in Figure 5.6b incubated with 1 µM miR222-Cy5; f) Fitted area of the 552 cm-^{1} miRNA-Cy5 peak plotted against the NaCl concentration of the substrates incubated with probe222 (black squares) and the half1 (red dots). The error bars represent the SD of the fitted spectra. The displayed spectra are offset to clarify the representation.

5.2.3 Bioassays specificity and sensitivity

Once the immobilization as well as the hybridization conditions were optimized, the two different approaches were compared in terms of sensitivity. The samples, after being functionalized with the two probes, probe222 for the one-step assay and half1 for the two-step assay, were therefore incubated with different miRNA concentrations, ranging from 0.5 nM to 250 nM, using miRNA- CyX and unlabelled miRNA, respectively. Finally, only concerning the two-step assay, half2-CyX was incubated on the samples previously functionalized with half1/miRNA duplex.

The collected spectra are shown in Figure 5.7. Both Cy3 and Cy5 vibrational pattern is clearly recognizable at high concentrations, whereas as the concentration decreases it is gradually overcome by the probe signals. Nevertheless, even at low concentrations, the presence of a peak arising from the Cy3 vibration can still be observed at 1462 cm^{-1} (Figure 5.7 a, b), making it suitable for the determination of the LOD. On the contrary, the Cy5 related signal already disappears at quite high concentrations (Figure 5.7 d, e), limiting its suitability for a quantitative evaluation.

A calibration curve was thus prepared taking advantage of the integrated area of the band at 1462 cm^{-1} (Figure 5.7c, f) of the CyX-labelled oligos. The graph reveals an interesting trend for both the used approaches. It is indeed clearly noticeable that the half1/miRNA/half2-CyX displays a lower Raman intensity at high miRNA concentrations, compared to the samples incubated with miRNA-CyX, due to the weaker interactions between the two halves of the probe and the miRNA itself. On the contrary, as the miRNA concentration decreases, the signal intensity of the two-step assay related samples is featured by a weaker reduction.

In order to calculate the limit of detection for both the Cy3-related assays, only the portion of the calibration curve between 25 nM and 0.5 nM, in which a linear regime was observed, was exploited. The data provided different detection limits, equal to 0.5 nM and 1.51 nM, for the one-step and two-step hybridization assay. As stated before, the interactions of the two halves of the probe with the miRNA are generally expected to be less strong if compared to the probe222/miRNA-Cy3 complex. A higher detection limit is therefore usually expected. Nevertheless, such gap can be levelled off by tuning the conditions of the hybridization step: this was in fact reduced using a higher salt concentration. Unfortunately, as was previously highlighted by Figure 5.7 d,e, and f, the Cy5-related signal disappeared already at quite high concentrations and the LODs are therefore expected to be higher. Indeed, they have been found to be equal to 10.3 nM and 10.93 nM for the one-step and two-step hybridization assay, respectively. Nevertheless, such results show that the two-step approach is suitable for the development of a label-free assay for the detection of miRNA, avoiding a complex and expensive chemistry needed for the labelling of the target miRNA, as in the one-step assay.

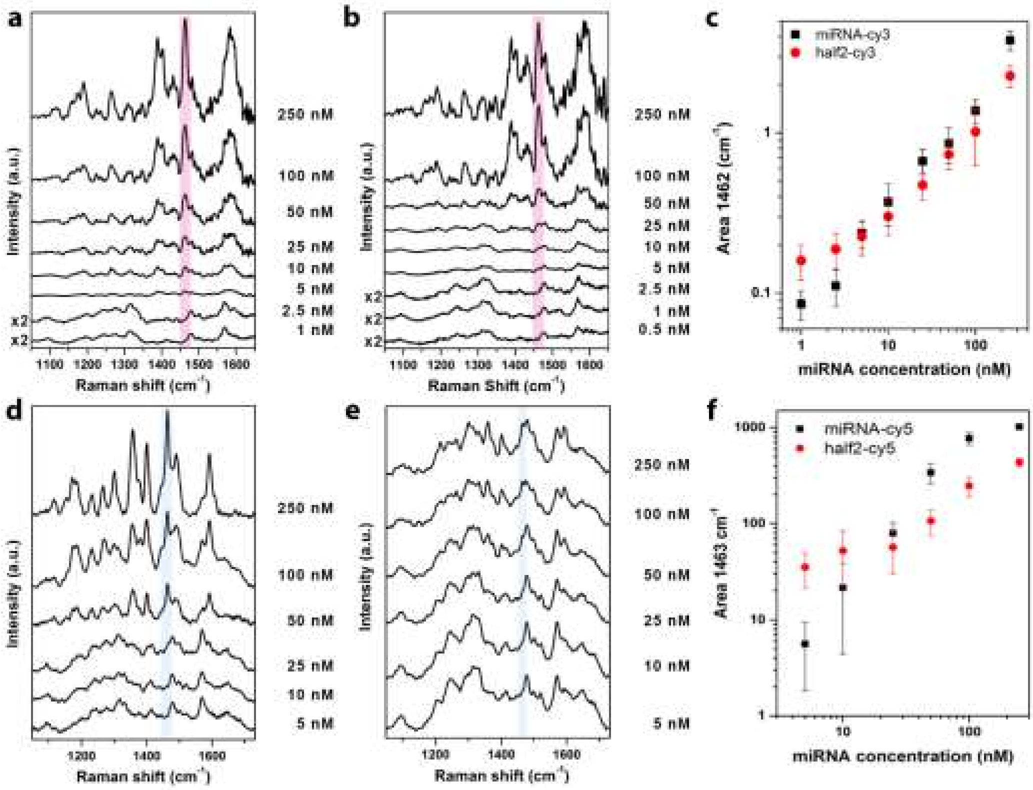

Figure 5.7 - a) SERS spectra collected from the samples incubated with different concentrations of a) miR222-Cy3; b) miR222 and afterwards with 1 µM half2-Cy3; c) Fitted area of 1462 cm^{-1} Cy3 peak plotted against miR222 concentration, obtained for miR222-Cy3 (black squares) and half2-Cy3 (red dots); d) miR222-Cy5; e) miR222 and afterwards with 1 µM half2-Cy5; f) Fitted area of 1462 cm^{-1} Cy3 peak plotted against miR222 concentration, obtained for miR222-Cy3 (black squares) and half2-Cy3 (red dots). The error bars represent the SD of the fitted spectra. The displayed spectra are offset for to clarify the representation. The displayed spectra are offset to clarify the representation.

In order to apply the presented bioassay to the detection of miRNA in real biological samples, it has to fulfil strict selectivity requirements, to avoid the non-specific signal due to the presence of different miRNAs, whose sequence analogies can be very strong. Moreover, different miRNAs can interfere with the target one and inhibit the hybridization with the probe. To check the selectivity of the assay mixtures of miR222 and miR16 at different concentrations were incubated on the SERS substrates previously functionalized for the specific recognition of miR222.

As shown in Figure 5.8, the selective detection of miR222 was not affected by the presence of miR16 under any circumstances. The characteristic vibrational features of the Cy3 labelled half2 at 1388 cm^{-1} and 1462 cm^{-1} are highlighted by the blue bands. No substantial difference is observed comparing their intensities measured in the absence (curve a) or in presence of miR-16 (curves b, c). Even using a 100 times higher concentration of miR16 with respect to miR222 does not lead to noticeable changes (curve f). Such results were confirmed also by an ELISA-like assay, emphasizing the selectivity of the probe towards miR222 in a wide range of concentration.

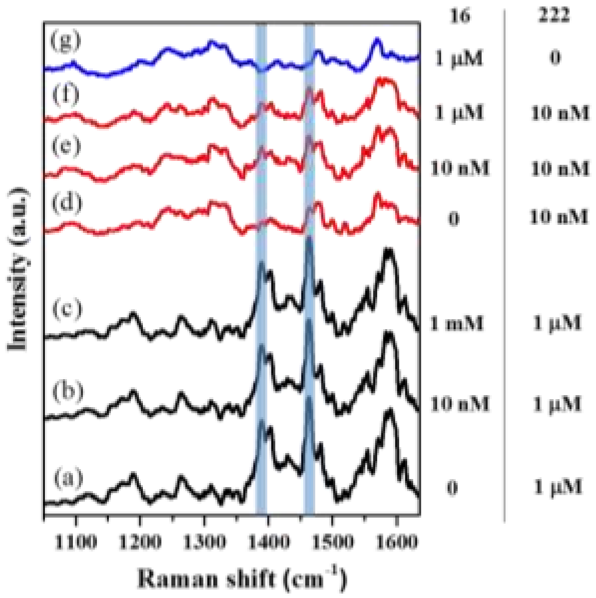

Figure 5.8 - SERS spectra of the samples incubated with mixtures of target miR222 and an interfering miR16 at different concentrations. Curves a, d, and g show the reference spectra of the substrates after the incubation with 1 µM and 10 nM of miR222, and 1 µM of miR-16 respectively. SERS spectra collected from the analysis of different mixtures are shown by the curves b, c, e, and f. The composition of the employed mixtures is reported on the right side. The displayed spectra are offset to clarify the representation.

5.2.4 miRNA 222 detection in cell extracts

In the previous sections, the one-step and the two-step assay were tested, in order to establish whether they could provide a good sensitivity. The obtained results confirmed the suitability of the two-step protocol for the detection of the target miRNA in real biological samples. To this aim, the synthetic miR222 was diluted in total RNA extracts of H460 NSCLC cells. Such cells line does not display a high expression of the miR222 if compared to other NSCLC cells [155], and therefore, the H460 extracts can be considered as blank samples, to be used to study the matrix interference. Total and small RNA enriched extracts of H460 and miR222 transfected H460 cells (H460-miR222) were employed. In order to assess the possible interference of the biological matrix with the hybridization process, incubating two different miRNA concentrations (100 nM, and 50 nM) both in the buffer solution and in the H460 cells extracts. As shown in Figure 5.9 no interference in the hybridizations process is detected, as the acquired spectra do not display any significant difference for both the concentrations.

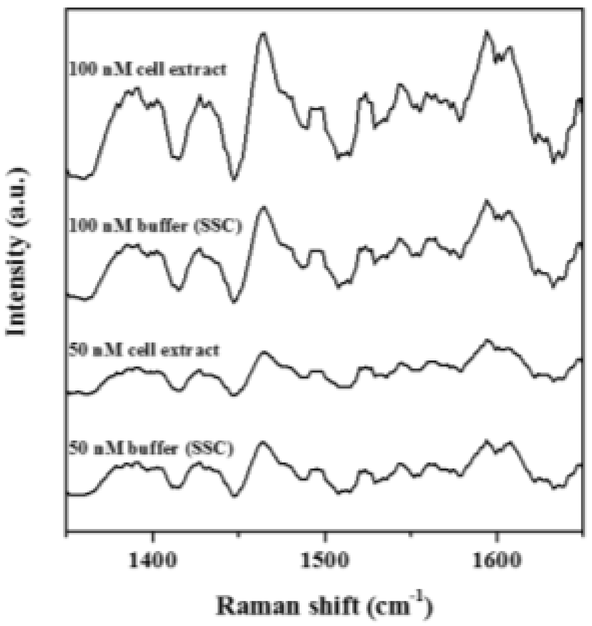

Figure 5.9 - Comparison between different concentrations of miRNA analysed after the hybridization step carried out in buffer or in cell extract. The displayed spectra are offset to clarify the representation.

Total and small RNA enriched extracts of H460 and miR222 transfected H460 cells (H460+mir222) were then employed to test the assay in the detection of miRNA in complex matrixes. A first quantification of the relative expression of miR222 in the presented samples was carried out by means of RT-qPC. Figure 5.10a shows the relative expression of miR222 in total and small-enriched RNA extracts. The comparison between the H460 and the H460-miR222 cells illustrates that the miR222 expression is about 40 times higher in the transfected cells.

Concerning the SERS analysis, a further step to optimize the ionic strength needed for the hybridization step was performed, diluting the samples 1:2 in SSC10x.

As for the LOD evaluation, a quantitative measurement was performed taking advantage of the Cy3 related band at 1463 cm^{-1}. As shown in Figure 5.10b, such band can be clearly observed in the spectrum related to the total RNA extract of the transfected cells, and, even though less evident, its presence can still be detected in the spectrum related to the small-enriched samples. On the contrary, the spectra related to the H460 small enriched RNA and the total RNA extract samples, do not display any assessable vibrational feature belonging to the Cy3. The integrated area of the highlighted band was then employed, in accordance with the data from the above presented calibration curves, to quantify the miR222 concentration in the analysed cells extracts. Concerning the total extracts of the transfected H460 cells a concentration of 3.240 nM was detected, while for the small H460-miR222 a concentration of 0.734 nM was calculated. However, this last result falls below the LOD and therefore it is not possible to state with certainty the reliability of the obtained data.

The results obtained from the SERS analysis are though in good agreement with the ELISA-like assay, which shows a higher miR222 concentration in the total extract (2.78 nM), in comparison with the small-H460-miR222 sample (0.650 nM) (Figure 5.10c).

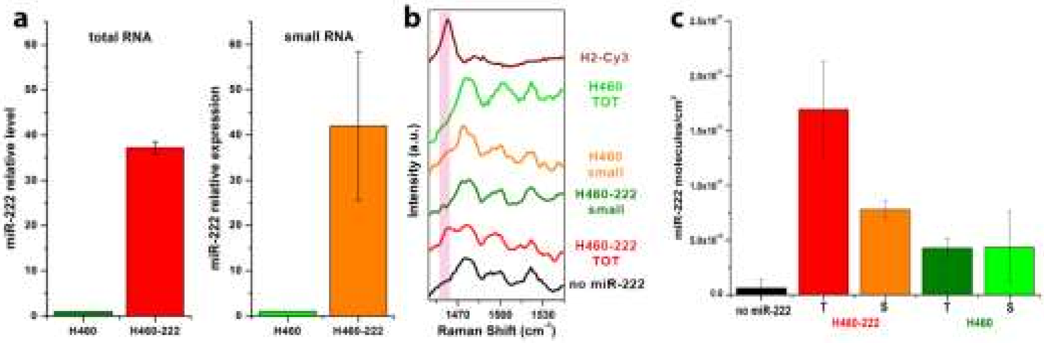

Figure 5.10 - a) RT-qPCR standard evaluation of the level of expressed miR222 in the small and total RNA extracts of H460; b) SERS spectra of miR222 transfected H460 NSCLC cells small and total RNA extracts of H460 NSCLC cells (from bottom to top). The displayed spectra are offset to clarify the representation.; c) ELISA-like assay results obtained on the same samples.

5.2.5 Influence of the Raman reporter position

After the successful optimization of the two assays, and their subsequent application to the detection of miRNA in real biological samples, we focused on increasing the sensitivity of the protocol. So far, the assays exploit an oligonucleotide sequence, miR222 or half2, labelled with a Raman reporter at its end. In such configuration, the reporter lies at a maximum possible distance from the Ag nanoparticle surface, which has been estimated around 7.5 nm for both the approaches. To further push the sensitivity and therefore the detection limits an additional modification has been applied to the two protocol, aiming to investigate the effect of a different labelling position of the Raman reporter along the sequence of the probe. Figure 5.11 shows the two different positions of the reporter, which can be localized at the beginning or at the end of the nucleotide sequence. Such positions have been named -3’ or -5’, depending on which binding site of the terminal ribose is exploited. Concerning the one-step assay the distance of the reporter from the Ag surface can be reduced to less than 1 nm. A strong SERS enhancement is therefore expected. Regarding the two-step assay the closest gap from the NPs surface is 3.5 nm. Notably, the labelling of the far and close to the surface positions of the Raman reporter are inverted for the two different assays, due to the different binding mechanisms of the labelled miRNA and half2.

Three different Raman reporters were employed to investigate the labelling position: Cyanine 3, Cyanine 5, that have already been used for the optimization of the bioassay, and Rhodamine 6G. Nevertheless, given the poor performance showed in section 5.2.3, no calibration curve was performed on Cy5-related assays.

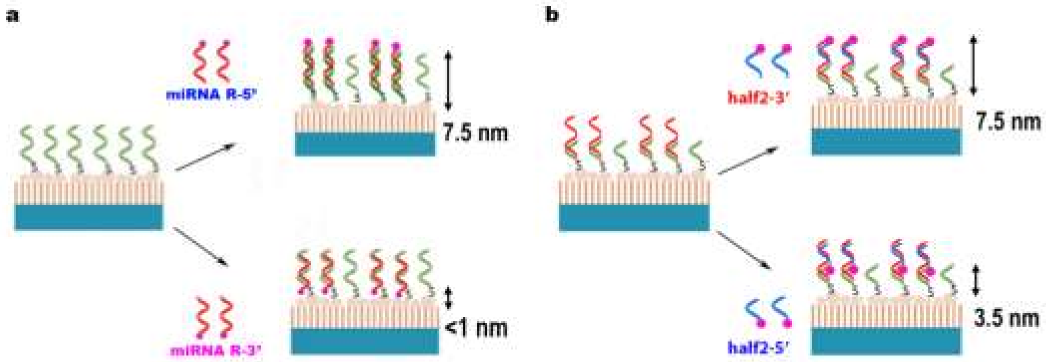

Figure 5.11 – Schematic representation of the Raman label position variation along the probe for the a) one-step and b) two-step assays.

As stated before, this last fluorophore is characterized by an intense absorption band around 520 nm, thus enabling the resonant excitation with a 514.5 nm laser line. A good resonant SERS enhancement is therefore expected. The band assignments for the SERS spectrum of Rhodamine 6G are reported in Table 4. Moreover, the presented Raman reporters were exploited in both the one-step and two-step configurations of the bioassay, for the detection of the miR222.

Table 4 – Band assignment for Rhodamine 6G.

Raman shift (cm^{-1})	Assignment	References
612	C−C ring in-plane bending in xanthene/phenyl rings	[158,159]
774	C−H out-of-plane bending	[158,159]
1127	C−H in-plane bending in xanthene/phenyl rings	[158,159]
1184	C−H plane bending in xanthene ring	[158]
1204	C−H plane bending in xanthene ring	[158]
1275	hybrid mode (xanthene/ phenyl rings)	[158]
1309	hybrid mode (xanthene/ phenyl rings and NHC_2H_5 group)	[158]
1364	C−C stretching in xanthene ring	[158]
1449	C-N stretching in NHC_2H_5 group	[158]
1509	C−C stretching in xanthene ring	[158]
1575	C−C stretching in phenyl ring	[158]
1595	hybrid mode (phenyl ring with $COOC_2H_5$ group)	[158]
1650	C−C stretching in xanthene ring	[158]

5.2.5.1 One step hybridization assay

In order to perform a quantitative measurement, the porous silicon based SERS substrates, functionalized with the probe222, were incubated with different concentrations of miR222, ranging from 100 nM to 0.5 nM (1 nM for Cy5), labelled with all of the presented Raman reporter, each one localized at the described positions. Figure 5.12 shows the comparison between the spectra of the miR222 labelled with Cy3, Cy5, and R6G in -3' position (Figure 5.12a, c, and e respectively), and in -5' position (Figure 5.12b, d, and f). A characteristic peak from each Raman reporter is highlighted to better underline the signal evolution. Concerning Cy3 and Cy5, the peak at 1463 cm^{-1} has been chosen, while for the R6G the band at 647 cm^{-1} was exploited (highlighted band in Figure 5.12). It is worth to notice that the selected band for R6G do not belong to its traditional vibrational pattern, shown in Table 4, but arises from the shift of the band located at 612 cm^{-1} plausibly due to the binding with the miRNA molecule. From such comparison, it is clearly noticeable that the spectra of the samples incubated with the target miRNA labelled with the reporter closer to the surface are featured by more intense SERS signals. Moreover, the labelled 5'-miRNA are affected by the presence of a higher background noise, due to the farther distance from the surface of the fluorophore, reducing the well-known phenomenon fluorescence quenching. Among the three investigated dyes, Cy5 displays the worst performance in terms of sensitivity due to its electronic off-resonant excitation using a 514.5 nm laser source. Moreover, the diminished performances of Cy5 could also arise from the steric hindrance due to its bigger dimensions, which could negatively affect the hybridization with the probe. Indeed, the Cy5 related spectra could provide a valuable information only down to 10 nM miRNA concentration independently of the labelling position, while for both Cy3 and R6G the limit was pushed to 1 nM.

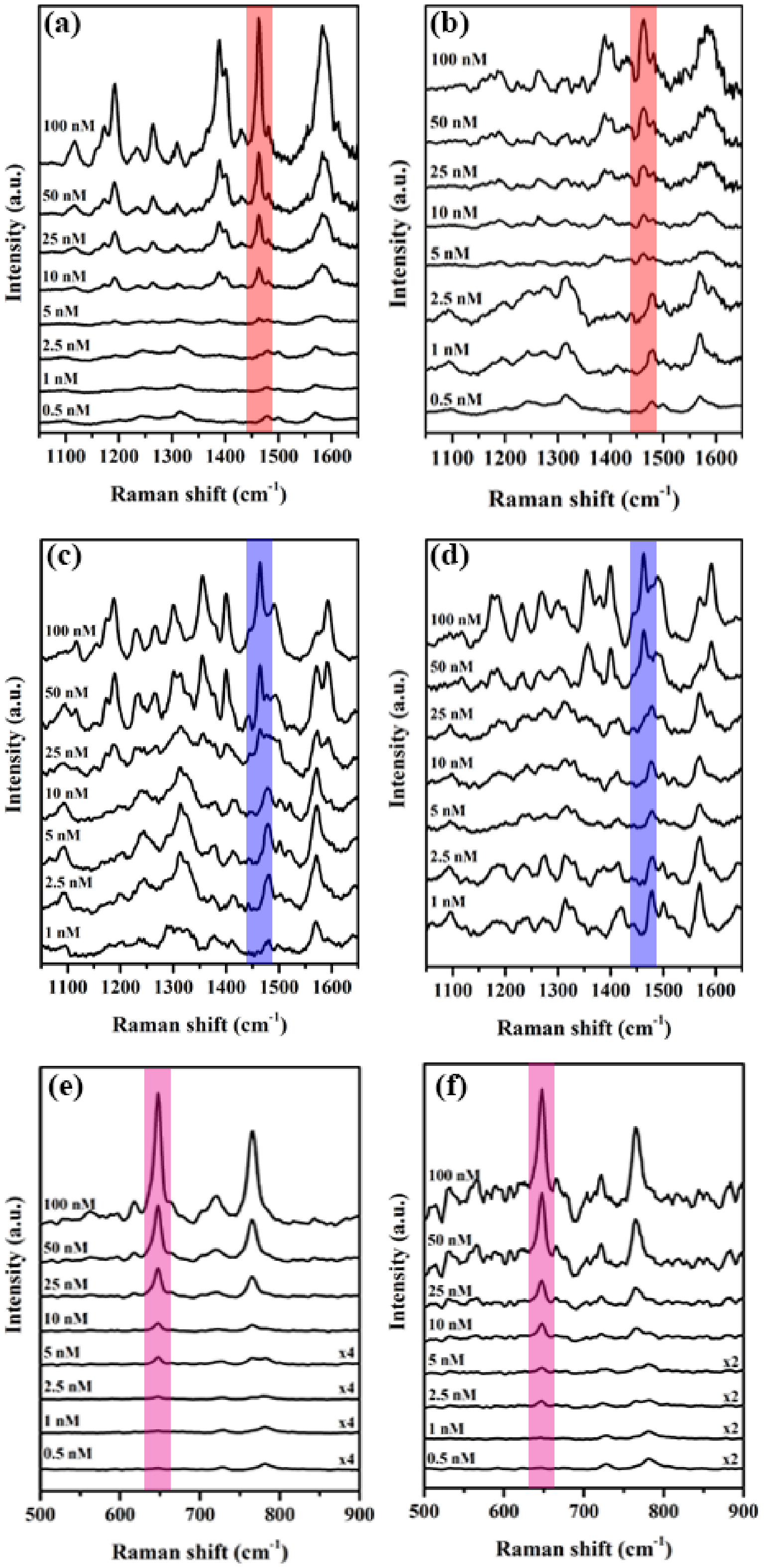

Figure 5.12 - SERS spectra collected from the samples incubated with different concentrations of a) miR222-Cy3 3' b) miR222-Cy3 5' c) miR222-Cy5 3' d) miR222-Cy5 5' e) miR222-R6G 3' and f) miRNA222-R6G 5'. The displayed spectra are offset to clarify the representation.

To evaluate the difference between the two labelling positions in terms of Raman signal enhancement, the calibration curve for both Cy3 and R6G, which are those that provide the best performances (Figure 5.13a, and respectively), can be analysed. For such a purpose, the integrated area of the previously selected bands has been calculated. From the analysis of the curves, a linear regime between 25 nM and 0.5 nM was observed and therefore exploited for the LOD calculations. Concerning Cy3, the calculated detection limits were 0.89 nM and 0.64 nM for the -3’ (black squares) and -5’ (red dots) labelling position, respectively, while for R6G these LODs were equal 0.83 nM and 0.46 nM. Such results do not confirm the expected outcome, since the lowest detection limits are recorded for the 5’-miRNA, meaning that the position of the Raman reporter is far from the NPs surface. Even though the signal related to higher concentration appeared to be more intense for the labelled position closer to the surface, a greater enhancement for lower concentration was expected, too.

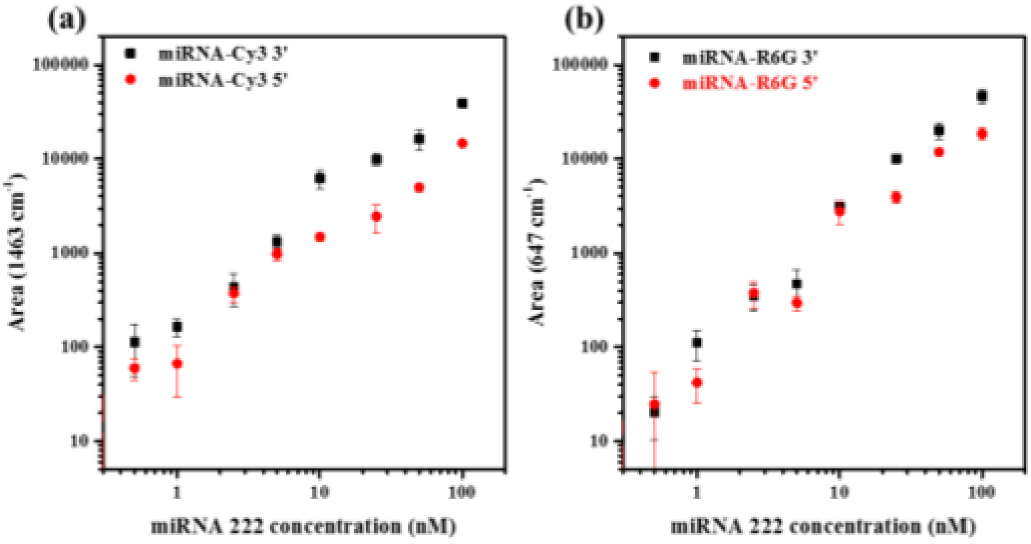

Figure 5.13 - a) Fitted area of 1463 cm^{-1} Cy3 band plotted against miRNA concentration, b) Fitted area of 647 cm R6G band plotted against miRNA concentration. Both Raman reporters are labelled in position -5’ (red dots) and -3’ (black squares). The error bars represent the SD of the fitted spectra.

A possible explanation to such conflicting results takes into account the relative position of the probe/miRNA duplex onto the surface. Figure 5.14 shows a simplified scheme of the probe/miRNA duplex orientation onto the Ag NPs surface. As stated in section 5.2.2. it is assumed that the majority of the probe molecules are vertically oriented onto the surface. However, the presence of a small amount of tilted molecules has to be taken into account, even though it is assumed that their presence will not alter the final result. Indeed, if the complex is localized within an inter-particle gap the enhancement of the EM field would be greater compared to the one occurring for a molecular system positioned on top of a nanoparticle. Particularly concerning the low concentration range, the contribution to the SERS signal could be mostly due to the inter-particle gap enhancement. In such framework the miRNA labelled with the reporter on top of the oligonucleotide chain, namely the 5’- labelling position, could exploit the enhancement arising from both the involved NPs. The resulting SERS signal could therefore be comparable to the one obtained for the fluorophore groups that are closer to the surface. Moreover, the steric hindrance of the 3’-labelled miRNA, due to the close proximity to the surface, could negatively affect the hybridization efficiency, resulting in a diminished SERS signal.

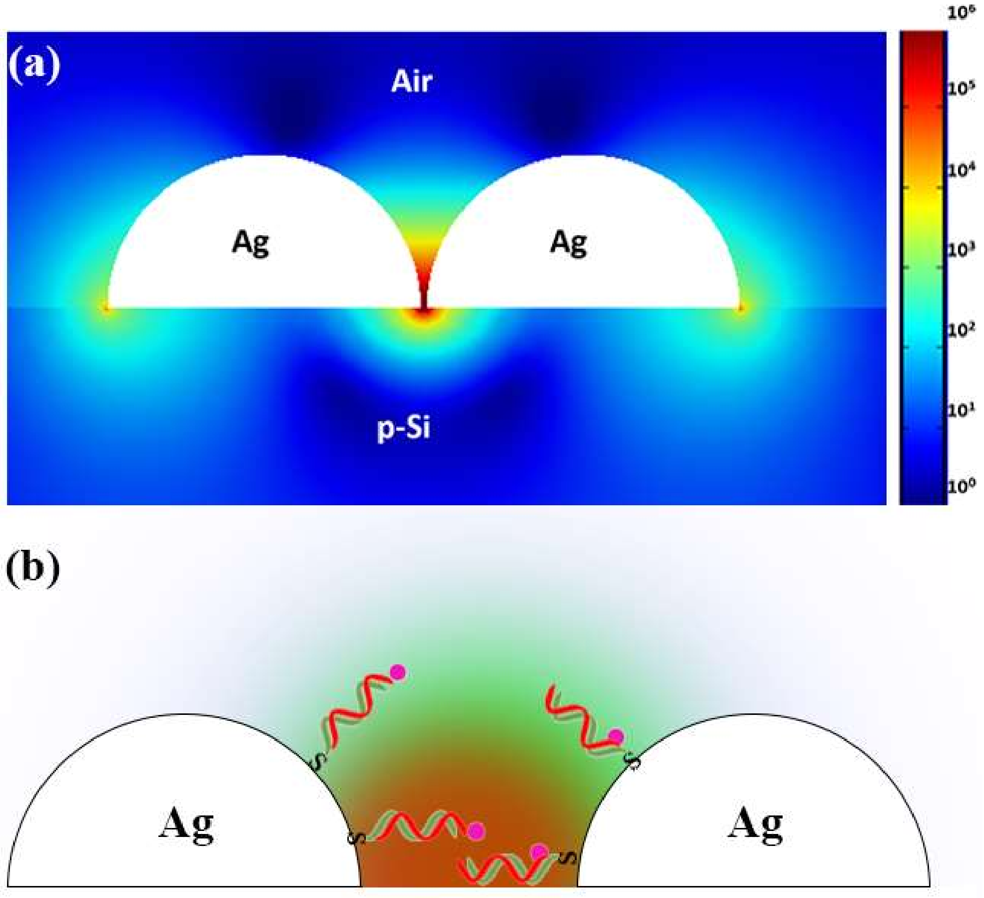

Figure 5.14 – a) Examples of near-field intensity distribution calculated for a Ag hemisphere dimers supported on pSi. b) Schematic representation of the possible binding sites and orientations for the probe222/miRNA-X hybridized complexes (X = Cy3, R6G).

5.2.5.2 Two steps hybridization assay

The same approach was exploited to evaluate the sensitivity of the two-step assay. Figure 5.15 shows the spectra of the samples incubated with different concentration of miRNA, subsequently incubated with the Cy3, Cy5, and R6G half2 labelled in the -3’ (Figure 5.15a, b, and c) or in the -5’ position (Figure 5.15d, e, and f). using the same range of concentrations. As for the one-step approach, the spectra collected for the samples incubated with the 5’-labelled half2, which correspond to the configuration in which the Raman reporter is close to the surface, are generally more intense (especially concerning the Cy3 and Cy5 related spectra) and less affected by the noise due to the fluorescence background, compared to the far position of the label. As for the above mentioned case the Cy5 related spectra do not provide a good sensitivity if compared to the Cy3 and R6G ones.

Once more, a calibration curve was performed for half2-Cy3 and half2-R6G and a linear regime between 25 nM and 0.5 nM was exploited to calculate LOD (Figure 5.16). The provided detection limits for the half2-Cy3 show an enhanced sensitivity for the half2 labelled with the Raman reporter closer to the surface (Figure 5.16a, red dots), if compared to the one in which the reporter is localized on top of the second half of the probe (Figure 5.16a, black squares). Indeed, the calculated LOD are equal to 0.68 nM and 1.51 nM, for the -3’ and -5’ label position, respectively. A similar trend is observed concerning the R6G-labelled half2. In fact, the detection limits for the 3’-half2 and the 5’-half2 are 0.860 nM and 0.234 nM, respectively. Such results emphasize the effect of the closer proximity of the Raman reporter with the NPs surface

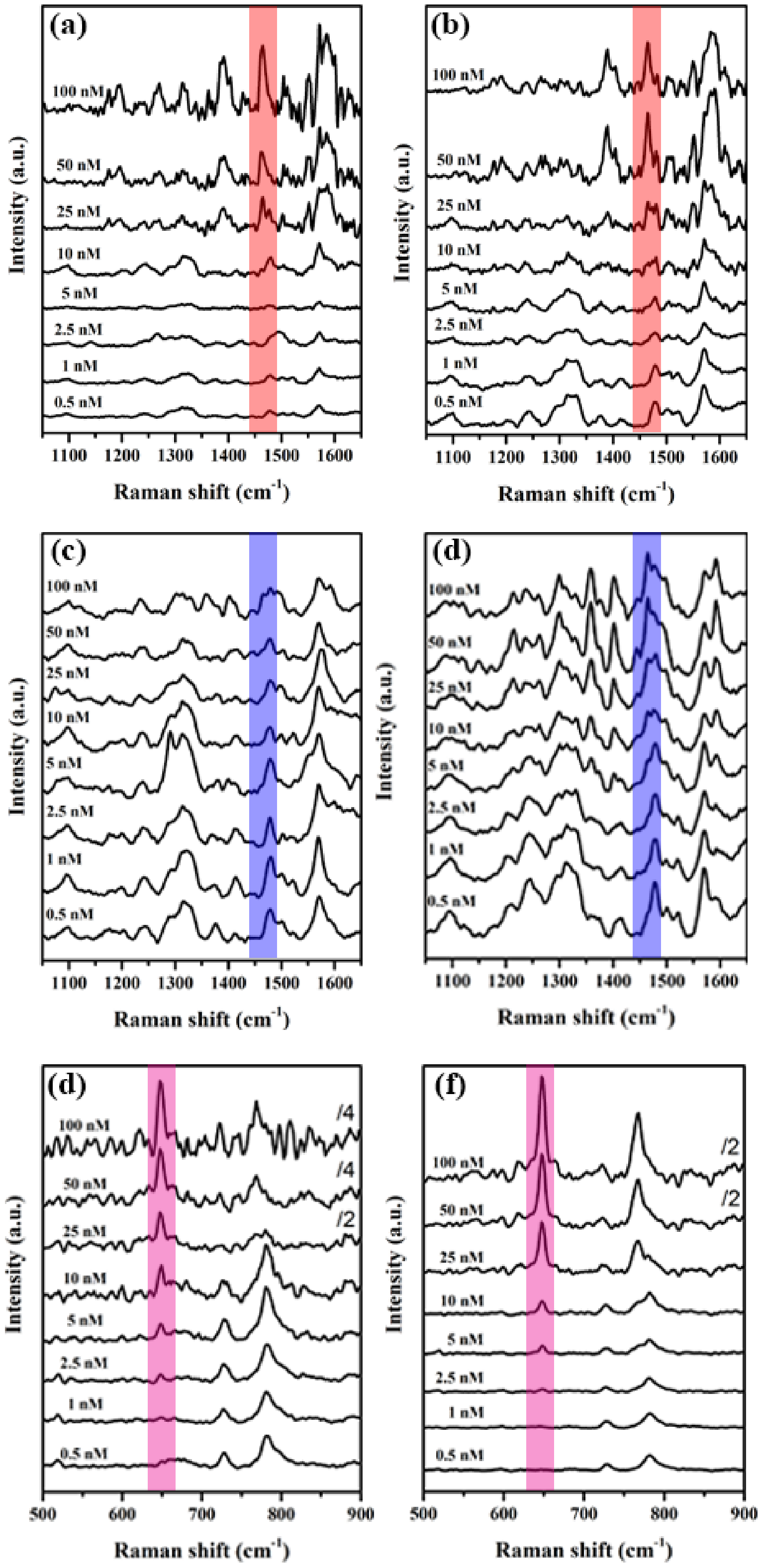

Figure 5.15 – a) SERS spectra collected from the samples incubated with different concentrations of a) miR222/half2-Cy3 3’ b) miR222/half2-Cy3 5’ c) miR222/half2-Cy5 3’ d) miR222/half2-Cy5 5’ e) miR222/half2-R6G 3’ f) miR222/half2-R6G 5’. The displayed spectra are offset to clarify the representation.

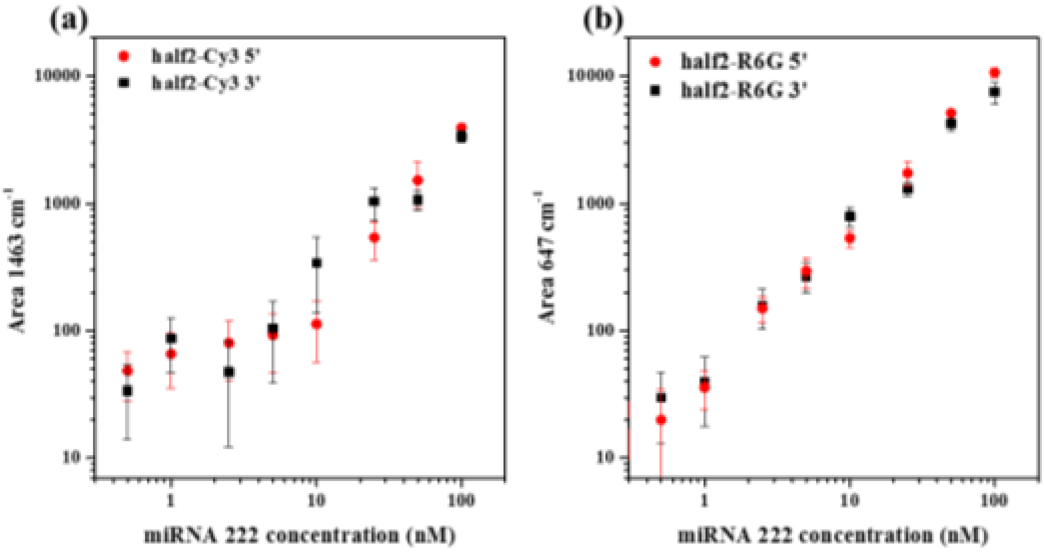

Figure 5.16 – a) Fitted area of 1463cm^{-1} Cy3 band plotted against miRNA concentration. b) Fitted area of 647 cm^{-1} R6G band plotted against miRNA concentration. Both Raman reporters are labelled in position -5' (red dots) and -3' (black squares). The error bars represent the SD of the fitted spectra.

Finally, since the Rhodamine 6G provided the best performances, it was exploited for the detection of miR222 in cell extracts, following the same protocol employed in section 5.2.4. For such experiment, the configuration displaying the R6G in close proximity with the surface was exploited. The samples were incubated with total and small RNA enriched extracts of H460 and miR222 transfected H460 cells as well as with the total and small enriched extracts of A549. The latter cellular line is indeed well known for the overexpression of miR222 [83]. A spectrum of the half2-R6G is presented as reference on the top of the graphs, as well as a blank control, located at the bottom. From the analysis of the integrated area of the R6G peak at 647 cm^{-1} (Figure 5.17), using the above presented calibration curves, a concentration of 2.22 nM was calculated for the total extracts of H460-miR222 cells, while concerning the A549 total extracts a concentration of 0.359 nM was detected. As expected, the detection limits were substantially lowered if compared with the previously obtained results (section 5.2.4).

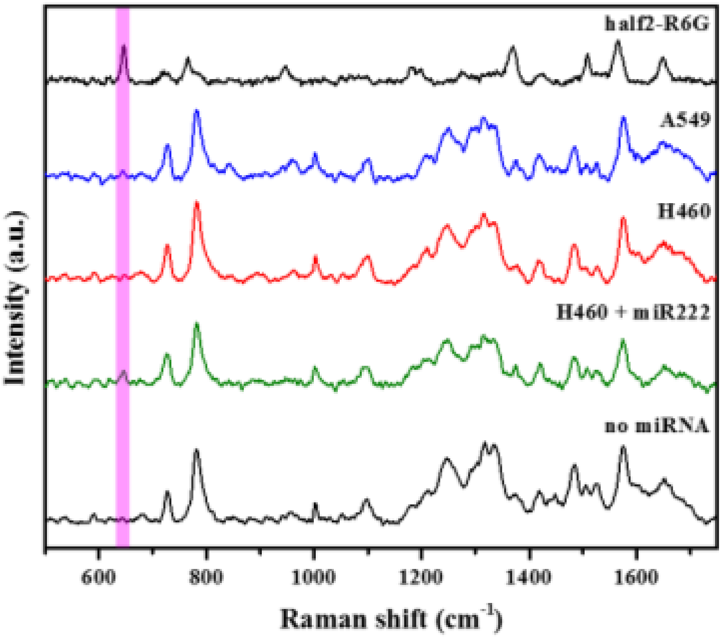

Figure 5.17 –SERS spectra of total extracts of miR222 transfected H460 NSCLC cells (red curve) H460 NSCLC cells (green curve), and A549 cells (blue curve). Reference spectrum of half2-R6G is shown at the top (black curve). SERS spectra of the control is shown at the bottom (black curve). The displayed spectra are offset to clarify the representation.

5.2.6 Conclusions

Porous silicon based SERS substrates integrated in a microfluidic chip were exploited for the selective detection and evaluation of miRNAs. To this purpose, two different methods were developed, based on a one-step and a two-step hybridization approach. This last protocol allows the label free detection of the target miRNA since the Raman reporter is bonded with the second half of the probe (i.e. half2). Moreover, the influence on the SERS signal of the position of the Raman reporter along the probe was investigated.

SERS analysis was employed for the optimization of each functionalization step of the two protocols, allowing to determine the optimal surface probe density needed to maximize the subsequent hybridization step. Once finely tuned, the sensitivity of the two assay was evaluated, by means of resonant Cy3 and R6G dyes. Comparable LODs for both the protocols were obtained, confirming a good hybridization efficiency also for the two step assay. Moreover, the Raman reporters were labelled farther and closer to the surface along the probe, in order to further push the previously obtained LODs. Concerning the two-step approach the detection limits were successfully lowered, thanks to the greater SERS signal enhancement resulting from the closer position of the reporters to the surface.

Finally, the detection and quantitation of miRNA in NSCLC cell extracts, were performed exploiting the two-step assay. A comparison between Cy3 and Rhodamine 6G, labelled respectively far and close to the Ag surface, was performed showing the enhanced sensitivity for the latter configuration.

5.3 Bacteria

The content of this section has been published in the following paper:

[87] Paccotti, N.; Boschetto, F.; Horiguchi, S.; Marin, E.; Chiadò, A.; Novara, C.; Geobaldo, F.; Giorgis, F.; Pezzotti, G. Label-Free SERS Discrimination and In Situ Analysis of Life Cycle in Escherichia coli and Staphylococcus epidermidis. *Biosensors* **2018**, *8*, 131, doi:10.3390/bios8040131.

5.3.1 Introduction

This last chapter focus on exploiting SERS spectroscopy, and in particular, to the application of Ag coated pSi substrates, to detect and discriminate between different kind of bacteria strains.

Escherichia coli and *Staphylococcus epidermidis* were selected as representative strains of, respectively, Gram-negative and Gram-positive bacteria. The strains used for the experiments are not pathogenic, reducing any risk for the operator.

S. epidermidis, a Gram-positive bacterium, is commonly known as an opportunistic pathogens and ranks among the first position as cause of nosocomial infections [158,159]. As the name suggests it can be found predominantly on human skin and his pathogenesis is mostly due to his penetration under the skin, thanks to a trauma or to the implantation of a biomedical device [160]. The biofilm formation plays a key role into the evolution of the *S. epidermidis* related infections. In particular, the extra cellular matrix produced by *S. epidermidis* is mostly composed by β 1-6-linked N-acetyl glucosamine residues that, along with the teichoic acids, form the polysaccharide intercellular adhesin (PIA), the polymer mainly responsible for the intercellular adhesion [130,160]. The mechanism probably relies on the cationic nature of PIA, originating from the partial de-acetylation of the N-acetyl glucosamine residues, that can easily interact with the negatively charged molecules of extracellular DNA (eDNA) present in the biofilm matrix [141,160].

E. coli, a Gram-negative bacterium, is one of the most common and widespread pathogenic microorganisms in food and water and as well as *S. epidermidis*, it is deeply connected with the human body, since it typically resides in the intestinal tract of the digestive system [131,161]. Compared with *S. epidermidis*, the composition of *E. coli* biofilm shows some substantial differences, expressing different adhesion proteins, like conjugative pili, curli and fimbria, and a larger amount of lipopolysaccharides (LPS) [87,139,161,162].

The bacterial population shows different stages of growth, ranging from the start of the evolution to the death of the bacterial cells. In the first stage, the cells try to adapt to environment and no significant growth is recorded (lag phase). This phase is followed by a rapid increment of the bacterial population in the second stage, named exponential phase, in which the nutrients are rapidly depleted. Eventually, the lacks of nutrients will lead to a stop into the bacterial growth, reaching the maximum expansion in the third phase, namely the stationary phase. At this stage, the number of living and dead cells reaches an equilibrium.

Afterwards, the bacteria enter in a phase of senescence, in which the number of dead cells rises, together with a reduction of the population [89,163]. As the bacterial population grows, also the extracellular matrix undergoes some modifications. Different stages have been identified in which the biofilm production plays a key role into the evolution of the bacterial strains [139,160,161]. The different stages can be summarized as follows.

A first step takes into account the attachment of the bacteria to the surface (I stage): the role of the EPS is to create a frame in which the cells are immobilized close to each other, transitioning from a planktonic state to a biofilm state [160]. The molecules involved in this step can vary among different strains. Indeed, *S. epidermidis* takes advantage of the production of PIA [160], while the cohesion of *E. coli* cells is mainly driven by protein or protein-based organelles [87,139,161]. Once the transition from a reversible to an irreversible attachment is complete (II stage) the biofilm undergoes an evolution towards the development of a three dimensional structure (mature biofilm, III stage). In this phase, the production of extracellular DNA (eDNA) plays a key role, that due to its poly-anionic nature can link other molecules together in the biofilm matrix [140,160]. Particularly in *S. epidermidis* the eDNA has been proven to interact with PIA, thanks to their opposite ionic characteristics, showing a positive correlation [141]. The last step of the biofilm evolution involves its detachment and disruption to allow the bacterial cells to go back to the planktonic state and to colonize different sites (IV stage) [139].

In this work, the Ag-PSD substrates were used to design a sensitive and yet reliable assay for the discrimination of Gram-negative and Gram-positive bacterial strains, minimally affect their environment and metabolism. The developed label-free approach aimed to fully resolve the vibrational pattern displayed by both *E. coli* and *S. epidermidis* strains, exploiting the vibrational differences to discriminate between Gram-negative and Gram-positive species. A complete deconvolution and labelling of the whole SERS bands was performed monitoring the evolution of each component over the complete growth curve. To further confirm the data obtained by the SERS analysis several fluorescence microscopy micrographs were taken at different times of the culture to monitor the amount of living and dead cells.

5.3.2 Labelling SERS Spectrum of *E. coli* and *S. epidermidis*

To fully understand the vibrational pattern of both *E. coli* and *S. epidermidis*, samples of the two strains were cultured on agar plate and collected promptly before the measurement, in order to maintain unaffected the bacterial environment. Figure 5.18 shows the comparison between SERS spectra of *E. coli* and *S. epidermidis* samples collected after 24 hours of incubation. This period of time was chosen in order to achieve the maximum amount of living bacteria, that according to literature is obtained in the stationary phase [163,164]. Each spectrum, which is displayed in the frequency range between 600 – 1800 cm^{-1}, was divided in three separated regions, namely low (600–900 cm^{-1}), middle (900–1380 cm^{-1}), and high (1380–1800 cm^{-1}) frequency regions. Each band shown in the two compared spectra has been assigned to a vibrational feature, according to the literature [88,89].

Each molecular features of both bacterial strains and their extracellular matrix lead to a characteristic vibrational fingerprint. The next section deals with the labelling of those vibrational features.

Zone I (600 – 900 cm^{-1}) shows several common vibrational features, but the main difference is due to the band located at 665~670 cm^{-1} (labelled Band 4 in Figure 5.18a, b). This band has been assigned to the presence of N-acetyl glucosamine (NAG) [89,163], that along with the N-acetyl muramic acid is one of the component of the amino sugar linear chain forming the peptidoglycan layer. This envelope, whose thickness varies depending on the species of the bacteria strain, is one of the main features to distinguish between Gram-negative and Gram-positive bacterial population. Indeed, the bacterial cell walls of Gram-negative bacteria, as *E. coli*, display a thin layer of peptidoglycan that separates the inner cytoplasmatic membrane and the outer phospholipidic layer of the membrane, while the cell wall of Gram-positive bacteria, such as *S. epidermidis*, shows a thick layer of peptidoglycan that protects the cytoplasmatic envelope. Furthermore, *S. epidermidis* biofilms is known to be constituted by an extracellular polymeric substance (EPS), mostly made of polysaccharide intercellular adhesin (PIA), in which cells aggregates are embedded. More in detail, PIA is a linear exopolysaccharide consisting of β(1,6)-linked N-acetyl-glucosamine residues. This band and the sub bands in the spectral neighbourhood can be seen as a clear fingerprint for the presence of the peptidoglycan structure and are indeed more intense in *S. epidermidis* (Figure 2b) than in *E. coli* (Figure 2a). Supplementary peaks in Zone I are associated to the twisting mode of phenylalanine located at 621 cm^{-1} [88] (only in *E. coli*), and to the Raman fingerprint of the nucleobases, ~650 cm^{-1}, 660 cm^{-1} (Band 3; only in *S. epidermidis*) [88,127], 725 cm^{-1} (Band 6) [83,127,165,166], 780 cm^{-1} (Band 9) [89,127,163,165], 800 cm^{-1} (Band 10; only in *S. epidermidis*) [89,163], and ~850 cm^{-1} (Band 12) [88,127].

Especially, the Band 6 at 725 cm^{-1} is associated to the ring breathing of adenine [83,88,165,166] due to the presence of extracellular DNA (eDNA), or to other important regulator of cellular metabolism such as ribonucleic acid (RNA), flavin adenine dinucleotide (FAD), nicotinamide adenine dinucleotide (NAD), adenosine monophosphate (AMP), adenosine diphosphate (ADP), or adenosine triphosphate (ATP). It is worth to notice that the DNA related bands (Band 6-9) are significantly less intense in the *S. epidermidis* spectrum. Notably, this bacterial strains have been found to produce less eDNA as a component of the extracellular matrix [138].

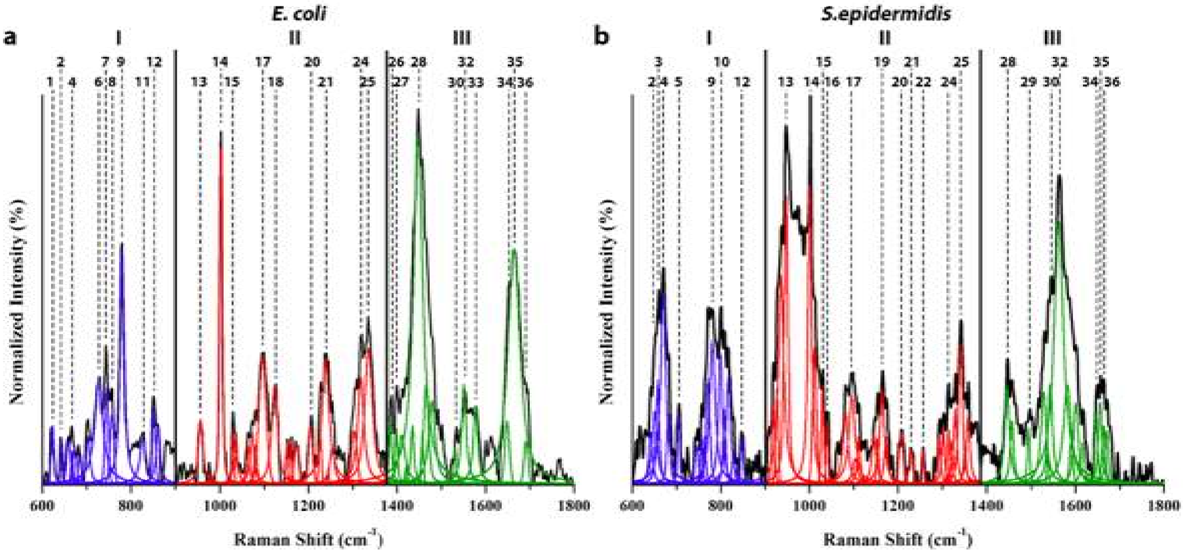

Figure 5.18 - SERS spectra of *E. coli* (a) and *S. epidermidis* (b) in the spectral range from 600 to 1800 cm^{-1}. The spectra were divided into three distinct zones (labelled zones I to III), while the band frequencies were labelled according to Table 1

A further proof of the presence of eDNA is displayed by numerous other signal such as the band at 650 cm^{-1} (Band 2), that has been assigned to guanine, the one around 780 cm^{-1} (Band 9), which was ascribed to the ring breathing of cytosine and thymine, and to the one at 848~851 cm^{-1}, labelled as vibrational modes of the thymine (Band 12).

The presence of DNA related bands, especially the signal located at 780 cm^{-1}, could be ascribed both to intracellular or extracellular DNA, that can be found in the biofilm matrix [162]. In accordance with previous studies [166–168], the eDNA could more efficiently interact with the substrate surface, compared with the intracellular DNA, and therefore it is more probable that the SERS signal could originates from eDNA. It is worth to notice that the majority of the mentioned studies proposes a bacteria sample pre-treatment aiming to remove the extracellular biofilm matrix [88,90,165,166], taking advantage of a colloidal solution of Au/Ag NPs. In accordance with such results, the SERS analysis of *E. coli* carried out by *Lemma et al.* highlights the complete lack of this band [88], whereas a quite low intensity is shown in the results obtained by *Witkowska et al.* it has a really low intensity [165]. This results support the eDNA hypothesis. Moreover, the adenine ring breathing peak (band 6), which as reported in literature usually dominated this portion of the spectra, appears to be greatly overcome by the signal belonging to the ring breathing of cytosine and thymine (Band 9, and only in *S. epidermidis* Band 10).

The remaining bands (Band 7, 8, 11) have been attributed to various component of the cellular environment, particularly band 7, located at 744 cm^{-1}, that arises from the vibrational mode, namely B1g, of the heme group of cytochrome c. This is a small molecule deeply involved in the electron transport chain [168–172]. Band 18 at 1124 cm^{-1} could provide a second hint about the presence of cytochrome c (Zone II); however, its effective presence is hard to be proven and is worth to underline that several different assignments concerning this band are reported in literature, such as: backbone C-C skeletal modes of proteins [90,173], C-C vibration of unsaturated fatty acids [90] and modes of phosphate groups related to the nucleotides [88,90]. In particular, the LPS presence on the Gram-negative bacteria surface, matches with the above assigned vibrations [174]. A band related to the presence of tryptophan, located at 755 cm^{-1} (Band 8), [169,175] and a weak signal at 826 cm^{-1} which was assigned to the vibration of O-P-O groups unit in the phosphates [88,104], can be also observed in the *E. coli* spectrum.

Zone II (medium frequencies, 900-1380 cm^{-1}) main vibrational feature is the signal due to phenylalanine at 1002 cm^{-1} (Band 14), whose abundance can be used as a marker for cell viability [176]. Furthermore, this compound plays a key role in the protein formation processes. Its sharp and intense band dominates this region of the spectrum making it suitable for the normalization of the whole spectrum. Additional bands, at ~ 1030 cm^{-1} and 1204 cm^{-1} (Bands 15 and 20) have been assigned to phenylalanine [88,89,163,165,169], confirming its presence.

Characteristic vibrational modes of protein, arising from peptide units bond vibrations, are highlighted by the amide I, II, and III bands, each one lying in a different spectral region, that provide information on the secondary structure of peptides [177]. Amide III vibrational pattern of frequencies ranges from ≃ 1150 cm^{-1} to ≃ 1350 cm^{-1}, displaying intense bands located at 1165 cm^{-1} and 1230 - 1241 cm^{-1} (Bands 19 and 21, respectively) [88,89]. Additional bands related to the twisting of CH_2 and CH_3 (Band 22) are located at about 1335 cm^{-1} (*E. coli*) and 1342 cm^{-1} (*S. epidermidis*) [89,169], whereas an additional peak assigned to the vibrations of methyl group organized in α-helix structures is located around 950 cm^{-1} (Band 13) [88]. It is worth to notice that, as stated in the literature, the signal of Band 21 arises both from the amide III vibrations and from the phosphate groups modes [88,89]. Thanks to the comparison between the spectra in Figure 5.18, a clear difference in the intensity of this band can be seen, showing a more intense signal in the *E. coli* spectrum than in the *S. epidermidis* one. This peculiar difference could be assigned to the contribute of the LPS phosphate groups that can be found on the external membrane of the *E. coli* [174], while concerning the *S. epidermidis*, only the teichoic acids located on the outer surface of the peptidoglycan layer could contribute to this vibration [133,160]. A further proof could be provided by a supplementary band at ≃ 1096 cm^{-1} (Bands 17), that can be assigned to the vibration of the phosphate groups [88,104]. However, such vibrational modes could also arise by the nucleobases vibrations, whose presence is pointed out by the guanine related signal at ≃ 1319 cm^{-1} (Band 24) [88,89].

To summarize, this region does not provide strong evidences to discriminate between the two strains species but is worth to underline that, compared to the previous work, a detailed characterization is provided, showing an enhanced sensitivity [88,89,165,178].

The vibrational pattern of proteins is shown to be more detailed in Zone III (high frequencies; 1380 – 1800 cm^{-1}), particularly concerning the amide I and II vibrational modes, with the addition of the modes related to the presence of fatty acids.

Amide I bands arise mostly from N–H bending and from C–C–N deformation combined with the C=O stretching vibrations [177]. Due to the large variety of contributes that are involved in the Amide I, the set of bands usually fluctuate in a wide range of frequency, typically from 1640 cm^{-1} to 1694 cm^{-1}, as shown in Figure 5.18a, b. Although the identification of each contribution is difficult, due to the overlap of the bands, and in spite of the challenges to obtain a unified analysis of the spectra, an attempt to isolate and discriminate the contribution of each vibrational mode has been made, taking into account the distinctive structure of the two bacterial strains and the previous studies in literature (Table 5). Moreover, a small contribution arising from cytosine and thymine carbonyl groups vibration, located in the early amide I region, has to be taken into account [127]. Despite the difficulties to isolate every single mode, this set of bands lies in a region of the spectrum where no other proteins vibrational features are located, making it suitable as marker for the determination of the proteins secondary structure [178]. Nevertheless, SERS spectra of peptides often show a suppressed amide I band, probably because the intensity of the SERS signal of the peptide chain is often influenced by the constituent amino acids, as stated by Kurouski et al [178,179]. In particular, the intensity of the amide I band is strongly influenced by the proximity to the metal nanostructure surface of the aminoacid itself, which could be affected by the length of the aminoacids sidechains. Longer sidechains, like aromatic groups, lead to a greater distance between the peptide and the surface, resulting in a lack of the amide I bands. On the contrary, peptide sequences characterized by shorter sidechains, like –H and –CH_3, usually display a more intense amide I band [178].

These differences can be clearly recognized comparing the amide I regions in Figure 5.18a, showing that the *S. epidermidis* e spectrum show a less intense set of amide I bands compared to *E. coli* one. Gram-negative bacteria display a more substantial presence of proteins allowing the diffusion of several molecules throughout the outer layer of the cell walls, such as outer membrane proteins (OMP) and porins [133,137]. Even though the contribution of each aminoacids sidechains is hard to estimate, the previously highlighted difference could be once again related to the different structure of the two bacteria strains cell wall. Indeed, these transmembrane protein channels are rich in hydrophilic aminoacids with short sidechains [180], which could be responsible for the more intense SERS signal related to the amide I vibrations in the *E. coli* spectrum (Figure 5.18a). Other OMPs can be involved in several vital processes, like virulence factors, waste exports, and cell signalling or adhesion [137]. In particular concerning *E. coli* bacterial cells, several adhesion protein are expressed, like conjugative pili, curli, and fimbriae [161]. *S. epidermidis* outer layer of the membrane is composed by a lower amount of proteins compared to *E. coli* (Figure 2b, Bands 34–36), as it can be easily noticed by the weaker signal of the amide I related bands. Indeed, as previously mentioned, the staphylococci surface is mostly composed by PIA, a homoglycan constituted of -1,6-linked N-acetyl glucosamine residues and another polysaccharide, referred to as 20-kDa polysaccharide (20-kDaPS): This is composed by partially sulphated NAG and glucose, which constitute the EPS of the extracellular biofilm matrix, and a small content of proteins [160,181]. Data collected by Neugerbauer et al in which the amide I band are strongly suppressed, corroborated this hypothesis [89],

Table 5 - Surface enhanced Raman spectroscopy (SERS) assignments in Gram-negative and Gram-positive bacteria.

	E. coli (cm^{-1})	*S. epidermidis* (cm^{-1})	**Proposed Assignment**	**References**
1	621		C–C twisting mode of phenylalanine	[6]
2	643	650	Guanine ring breathing	[88,127]
3		660	Guanine, thymine ring breathing	[6]
4	665	670	NAG	[89,165]
5	702	706	PDMS	[184]
6	725		Adenine ring breathing	[83,88,167,168]
7	744		B_{1g} heme vibration (cytochrome c)	[170–174]
8	755		Tryptophan ring breathing	[171,177]
9	778	780	DNA/RNA ring breathing (cytosine/thymine)	[89,127,165,167]
10		800	DNA/RNA ring breathing	[89,165]
11	826		$\nu_a(O-P-O)$ str.	[88,104]
12	851	848	Thymine	[88,185]
13	955	950	$\nu(CH_3)$ of proteins (a-helix)	[88]
14	1003	1002	Phenylalanine	[88,89,165,167,171]
15	1032	1030	Phenylalanine C–H in plane bending	[88]
16		1040	ν (CC) aromatic ring	[89]
17	1096	1097	$\nu_s(PO_2)$	[88,104]
18	1124		$\nu(PO_2)$	[88]
19		1165	Tyrosine, phenylalanine, amide III	[89]
20	1204	1208	Phenylalanine	[171]
21	1241	1230	$\nu(PO_2^-)$, amide III	[88]

22		1257	amide III	[88]
23		1277	PDMS	[184]
24	1319	1314	Guanine, CH$_2$ twist (lipids)	[88,89]
25	1335	1342	Protein twisting (CH$_2$ and CH$_3$), ν(NH$_2$) Adenine	[89,171]
26	1386		δ(CH$_3$) symmetrical	[88]
27	1399		C– O– O $^-$ stretching in aminoacids	[89]
28	1449	1446	Scissoring (fatty acids, phospholipids, and mono- and oligo-saccharides); CH$_2$CH$_3$ deformation	[88,89]
29		1495	δ (CH$_2$)	[89]
30	1533	1529	Amide II of proteins, N-acetyl related bands (amide II)	[89]
31		1538	Amide II of proteins	[89]
32	1553	1564	Amide II of proteins, guanine/adenine (only *S. epidermidis*)	[88,89,127]
33	1579		Guanine, adenine, tryptophan (proteins)	[88]
34	1651	1648	Amide I of proteins (α—helix), cytosine/thymine	[88,89,127,179]
35	1667	1657	Amide I of proteins (random coils)	[179]
36	1694	1665	Amide I of proteins (β—sheet)	[179]

The last clearly noticeable difference between *E. coli* and *S. epidermidis* can be observed in the early region of Zone III. It concerns the presence of the vibrational modes of the phospholipids, around 1450 cm^{-1} (Band 28) [88,89], and the bands belonging to the amide II located at about 1553 cm^{-1} (Band 32) [88,89], typically arising from the NH in-plane bending combined with CN/CC stretching and CO in-plane bending vibrations. These differences originate, as previously stated, from the different composition of the membrane of the two bacteria strains, especially concerning their external layer. Indeed, the external layer of Gram-positive bacteria is only made by peptidoglycan with the addition of a small amounts of teichoic acids, whereas Gram-negative bacteria show an additional phospholipidic layer. Such differences can be recognized in the comparison between the two spectrum, as the *E. coli* one displays an intense band at 1449 cm^{-1} (Band 28) due to the additional phospholipidic layer and to the LPS in the biofilm matrix [88,89]. Conversely, the *S. epidermidis* displays a more intense amide II vibration (Band 32 at 1564 cm^{-1}), probably because of the contribution from both the N-acetyl related vibrations at around 1530 cm^{-1} (Band 30) [89] (due to peptidoglycans and to glucosamine in the EPS), and from the vibrations assigned to guanine and adenine (Band 32) [127].

5.3.3 Comparison between Raman and SERS

In order to prove the richness of spectral information provided by SERS analysis with respect to Raman spectroscopy, a comparison between these two techniques has been made, acquiring a Raman spectrum of *E. coli* with the same acquisition conditions. A representative spectrum for both approaches is shown in Figure 5.19. It is clearly noticeable that the SERS analysis provide a clear enhancement of the vibrational features related to the outer membrane and biofilm components, due to the close proximity of these structural elements to the surface of the Ag coated pSi/PDMS substrates, enabling the detection of those features that are characteristic of each bacterial strains. The major efficiency of the SERS analysis is particularly witnessed by the intensity of the eDNA related band, at 788 cm^{-1} and 1319 cm^{-1}, and by the change of shape of the phospholipids signal at 1450 cm^{-1}, due to an increased contribution of the phospholipids vibrational modes, located on the outer membrane.

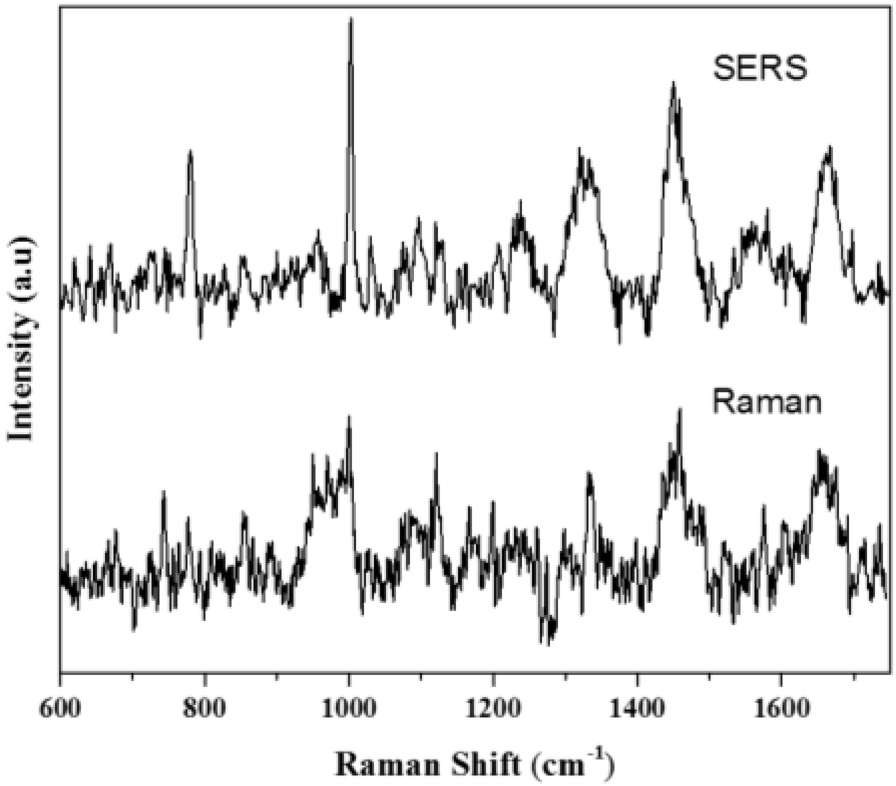

Figure 5.19 - Comparison between Raman and SERS spectra of *E. coli* in a spectral range from 600 to 1800 cm^{-1}.

5.3.4 Monitoring Bacteria Metabolism

In order to evaluate the behaviour of the bands labelled in Table 5, the metabolic evolution of each population of bacteria was analysed at fixed times of culture (i.e., 12, 24, and 48 h). Therefore, the variation over times of selected vibrational features of the principal molecular components of living bacteria, such as proteins, polysaccharides, DNA, and phospholipids, was took into account.

Figure 5.20 shows the average SERS spectra, which are divided into the same regions as in Figure 5.18, acquired analysing samples of living *E. coli* and *S. epidermidis* at different times. Moreover, to provide a further confirmation of the data obtained by the SERS analysis, fluorescence microscope imaging was employed to monitor the evolution of the bacteria population over time. As stated before, in the first 12 h of incubation, an exponential increase of the bacterial population started is observed, due the fast consumption of the nutrients provided by the culturing medium. These nutrients will eventually be depleted around 20 h of incubation, where a maximum number of living bacteria is reached, entering in the stationary phase [89,139]. After reaching a maximum the bacteria start to die, due to the depletion of the nutrients, reaching an equilibrium between living and dead cells. Afterwards, the bacteria population start to decrease, as the number of living cells is increasingly reduced while the number of dead one rises. [89,139]. This beginning of this phase can be recognize in the vibrational pattern evolution of the measurements performed at 48 h. The spectra shown in Figure 5.20 highlight a trends that match the succession of the exponential, stationary, and death phases of the growth curve.

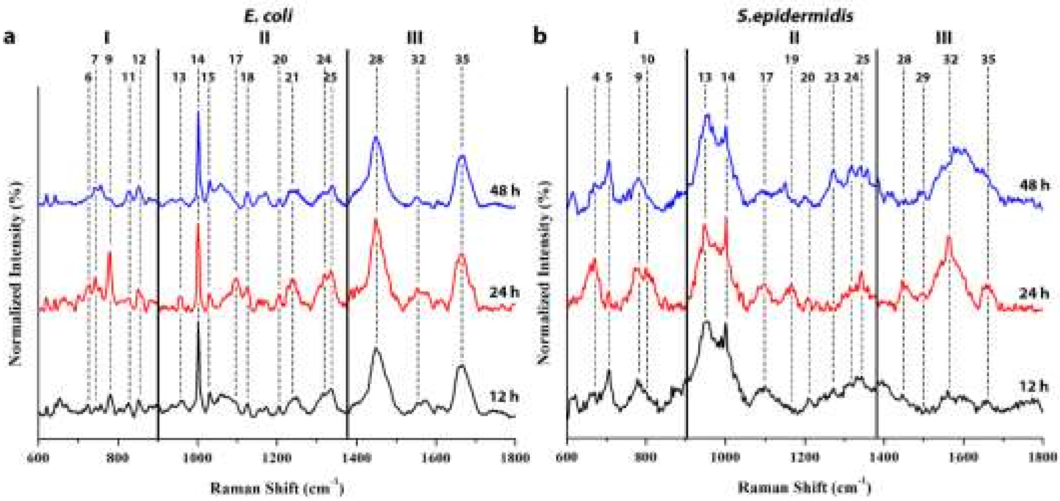

Figure 5.20 - SERS spectra of *E. coli* (a) and *S. epidermidis* (b) in the 600 to 1800 cm^{-1} range, collected after 12, 24, and 48 h of culturing. The spectrum was divided into three distinct zones (labelled zones I to III), while the band frequencies were labelled according to Table 1

Figure 5.20a (*E. coli*) shows a strong increment of eDNA related bands during the first 24 hours, in particular concerning Band 9 (Zone I) at around 778 cm^{-1}, that is related to the ring breathing vibration of the nucleobases. This could be due to the accretion of eDNA from the bacteria into the biofilm matrix during the exponential phase [162] because, thanks to its poly-anionic nature [141], it has been proven to be a major component in the formation of extracellular matrix, leading to an increased inter-cellular adhesion and the exchange of genetic information [140,162]. Coherently, a raise of other nucleobases and phosphate groups related peaks at 1096, and 1124, and 1560 cm^{-1} (Bands 17, 18, and 32, respectively), was observed. As discussed in the previous section both nucleic acids and phospholipids provide a contribution to the signal of the phosphate groups, which is shown to be stronger in the *E. coli* spectrum, because of the higher amount of eDNA and the presence of LPS on the outer layer of the membrane. A similar pattern is observed in Zones II and III, displaying a slight increase of the vibrations related to the structural components, such as amide I, II, and III of the protein and phospholipids: especially the amide III bands located at 1241 cm^{-1} and 1335 cm^{-1}, and the amide II bands at 1553 cm^{-1} (Bands 21, 25, and 32, respectively), display the major intensity raise. After 48 hours of culture, a clear reduction in the intensity of the bands assigned to the structural components is observed (i.e., proteins, nucleic acids, phospholipids), due to the decrease of the bacterial population in the late stationary phase. In particular, a more substantial decrease is observed for the bands related to nucleic acids with respect to the protein bands [182,183], probably because of a concentration decrement of such constituents. As expected, Figure 5.20 shows a dramatic decrease in intensity of the DNA related vibrational modes, in particular Band 9 in the *E. coli* spectrum, whereas a weaker signal reduction is observed for the protein bands. A comparable behaviour is observed in *S. epidermidis* spectrum (Figure 5.20b). In the first 24 hours a strong increase of the signal of DNA and structural components is noticed. In particular, a significant increments of NAG related band at 670 cm^{-1}, which is one of the component of the peptidoglycan layer constituting both the outer layer of the *S. epidermidis* cell wall and the EPS in the biofilm matrix. Such results could be interpreted as a signal of new cell membranes construction. A less intense increment was observed for the DNA peak located at 778 cm^{-1} (Band 9). A positive correlation between the accretion of eDNA and EPS has been previously reported [141], perfectly matching our results, in which an increase of both EPS and eDNA is observed during the first 24 hours, whereas a decrease is shown after 48 hours of culture (late senescence phase). Concerning the proteins vibrational modes, amide II and III bands located at about 1657, 1563, and 1165–1342 cm^{-1} (Figure 5.20) respectively, exhibit an increase after 24 hours of incubation compared to the samples analysed after only 12 hours, pointing out a rise of the structural components both in the cell wall and in the biofilm matrix. As reported above for *E. coli*, after 48 hours of incubation all the highlighted bands display a substantial decrease, implying an alteration in the bacterial in the bacteria metabolism. To further validate the results obtained from the SERS analysis a set of fluorescence microscope images was taken at 12, 24, and 48 hours of incubation. Figure 5.21 and Figure 5.22 show the evaluation of dead and living bacteria, as well as the presence of nucleic acids for both bacterial strains after staining respectively with PI, CFDA, and DAPI. The pictures were taken at different times of culturing. As displayed in Figure 5.21b and Figure 5.22b the number of living bacterial cells rises during the first 24 hours, and subsequently decreases after 48 hours. As stated before, after 48 hours of culture, the bacteria start reducing their population, due to autolysis and apoptosis processes. This behaviour is clearly underlined in Figure 5.21c and Figure 5.22c. A high fluorescence background is observed for the DAPI staining, and in particular concerning the *S. epidermidis* samples, while both the images collected at 12 hours, display a great amount of PI positive cells. Although a bacterial staining kit was exploited, in which the molecules used are studied for their specific interaction with a target, as the nucleic acids for PI and DAPI, this can be subjected to interference with other structural components. For instance, DAPI can be affected by a high fluorescence background leading to an error into the enumeration of the positive cells [184,185]. At the same time, the PI staining, which is largely used for the bacteria viability, has been investigated because of his tendency to also label the viable cells of the Gram-positive and Gram-negative bacteria in the first phase of the bacterial growth (i.e. exponential phase) [186]. As a result, the presence of eDNA and EPS in the biofilm matrix, could lead to a certain amount of binding between the dye and these components. Therefore, the acquired images can only provide a qualitative information, even though they match the evolution over time showed by the SERS analysis. Nevertheless, a further effort to obtain a quantitative data from the images in Figure 5.21 and Figure 5.22 was made, by combining the image analysis with a microbial viability assay (WST8), to estimate the amount of living and dead cells during the selected time points. Figure 5.23 shows the results obtained from both analyses. It can be seen that both the experiments displayed trends that are coherent with the SERS analysis. The increase of the amount of living cells (CFDA signal in green) within the first 24 hours is clearly recognizable, in particular in comparison to the samples taken at 12 h, and its subsequent reduction after 48 h of culture. The WST8 assay displays a comparable trend, showing a higher amount of living bacteria at 24 hours, as well as the increase of dead cells, and the simultaneous decrease of living ones. Indeed, comparing the values recorded for the 24 h and 48 h samples, the amount of dead cells (PI signal in red) is increasing over time.

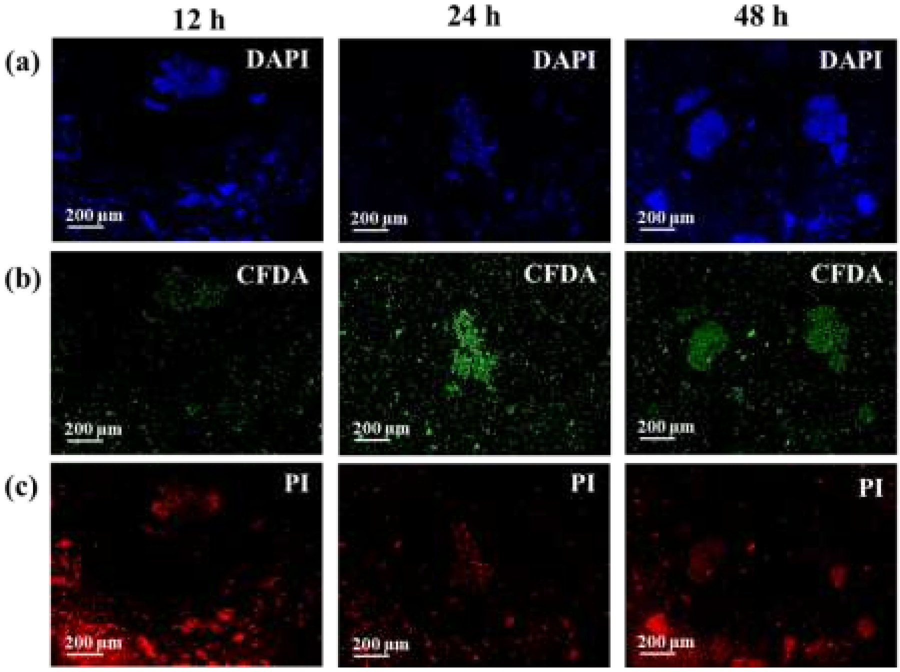

Figure 5.21 - Fluorescence micrographs collected after the staining of the *E. coli* cultured for 12, 24, and 48 h, using a) DAPI, b) CFDA, and c) PI. Nucleic acids are labelled in blue while living and dead cells are displayed in green and red, respectively.

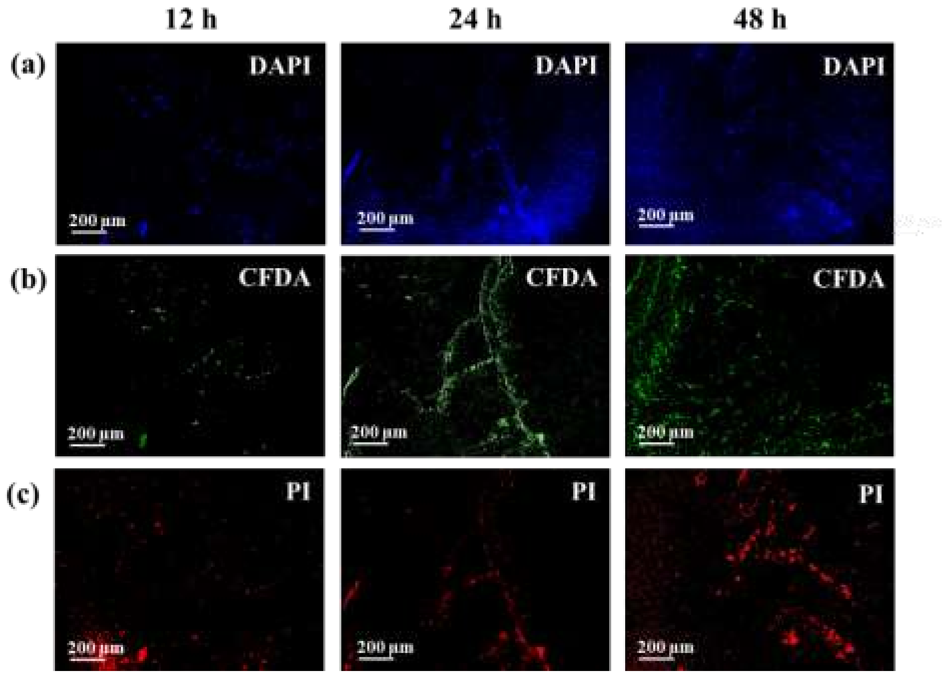

Figure 5.22 - Fluorescence micrographs collected after the staining of the *S.epidermidis* cultured for 12, 24, and 48 h, using a) DAPI, b) CFDA, and c) PI. Nucleic acids are labelled in blue while living and dead cells are displayed in green and red, respectively.

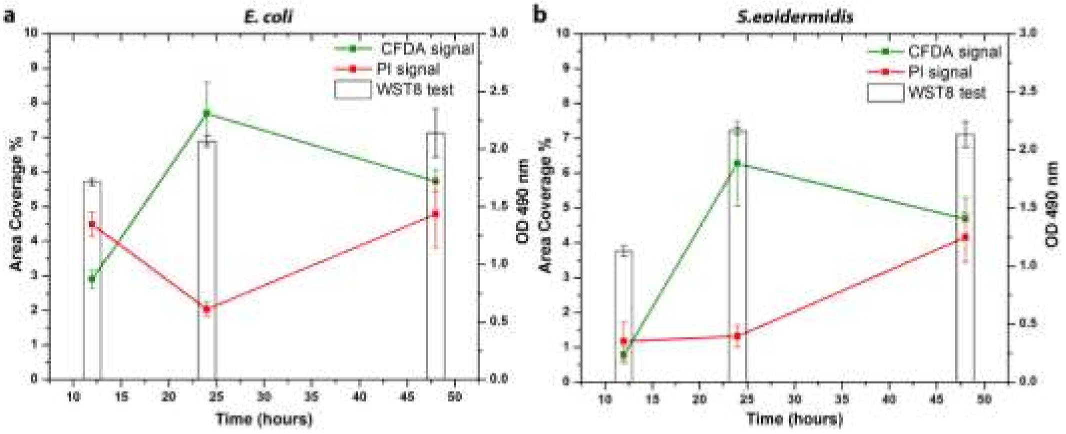

Figure 5.23 – WST8 assay and image analysis for the evaluation of the amount of dead and living bacteria cells for a) *E. coli* and b) *S. epidermidis*.

5.3.5 Conclusions

In this work, the detection and discrimination on different bacterial strains (i.e. *E. coli* and *S. epidermidis*) was carried out thanks to the Ag-PSD substrates. In comparison with other reported technique, the employment of such substrates allows to achieve several advantages both in terms of fabrication and simplicity of the analysis. Indeed, it combines the low cost and simplicity of fabrication, with the opportunity to develop a label-free bioassay with a minimal treatment of the samples. Thanks to these features, it was possible to preserve the biofilm matrix of the bacteria that has been proven to be an important constituent of the bacterial environment and to strongly contribute to the vibrational pattern of both bacterial strains. A complete characterization of the SERS spectra of both Gram-negative and Gram-positive bacteria was obtained, allowing to identify and depict the main spectral differences. In particular, a strong contribution to the vibrational pattern was given by the outer layer of the bacterial cells along with the extracellular matrix, as stated before, especially for the vibrational modes related to the peptidoglycan, EPS, and LPS, as well as to the presence of eDNA. Furthermore, the deconvolution of the vibrational features was used to discuss the growth over selected time of both bacterial populations. Once again, the biofilm matrix plays a key role in the evolution of the bacteria population, as a strong increment of the structural components (lipids, phospholipids, eDNA, and proteins) was observed within the first 24h, while a net decrease over 48 h of incubation was recorded. The evolution of the highlighted bands has been proven to match the evolution of the biofilm matrix composition over the bacterial growth. To obtain a further confirm, an analysis of the fluorescence image of stained samples was performed. The results show an increase of the living bacteria cells within the 24 hours of culture, while after 48 hours a net decrease is observed, combined with a rise of the number of dead cells.

Conclusions

This thesis was focused on providing a reliable platform for the development of bioassays for the detection of various biological targets by means of Surface Enhanced Raman Scattering. A first study was carried out to investigate the correlation between the variation of the synthesis parameters and both the morphologies and the distribution of the produced silver nanoparticles, in the framework of metal-dielectric SERS substrates. To this aim, a microfluidic approach was employed allowing a fine control over the variation of temperature, silver precursor concentration and solution flow rate. Moreover, the obtained morphologies were evaluated by means of image analysis of the related FESEM micrographs and the effect of the variation of each parameter onto the shape and the size distribution of the nanoparticles was therefore highlighted. It was noticed that an increase of temperature has the strongest effect, causing the production of bigger nanoparticles and leading to a faster reaction rate, compared to room temperature. However, a broader distribution of the silver particle size was observed. A ten-time raise of the silver precursor concentration led to similar results, causing an increment of the nanoparticles dimensions. At last, the flow rate showed to be the less effective of the three synthesis parameters, whose influence was often overcome by the combined effect of temperature and $AgNO_3$ concentration. Finally, the assessment of the SERS efficiency and reproducibility of the produced samples was carried out using 4-MBA as molecular probe. Both the intensity and the reproducibility of the SERS signal were evaluated, aiming to investigate the correlation between a specific morphology and the SERS response. In this framework, the NPs distribution on the substrate surface played a key role, in particular concerning the size of the inter-particles gaps. Even though this analysis showed conflicting results, a few trends were highlighted, confirming the relationship between the SERS efficiency and the morphology of the related substrates.

After having discussed the effect of each synthesis parameters on the Ag NPs synthesis, the focus was devoted to their bioapplications. In order to exploit a greater stability and reproducibility of the SERS signal, the Ag-PSD synthetized by immersion plating were used. Concerning the application of the silvered porous silicon substrates, two different bioassays were developed: at first the work focused onto the selective recognition and quantification of miRNAs, and in particular miR222 as it is well known as a biomarker for lung cancer, developing two protocols for the low-concentration and label-free detection of such small biomarker. A second application was instead oriented towards the discriminations of different bacterial strains.

To selectively detect miRNAs, a hybridization with a complementary probe labelled with a Raman reporter was exploited. A one-step and a two-step protocols were developed and each step of the bioassays was finely optimized to achieve the maximum amount of hybridized molecules. Several resonant Raman dyes were employed to label the probes aiming to determine which one could provide the best performances. Moreover, in order to accomplish lower detection limits, the position of the Raman reporters along the probe chains was investigated. Finally, the two-step protocol was applied for the detection of miR222 into NSCLC cell extracts, using an R6G labelled close to the surface, analysing total and small enriched RNA extracts of H460 and miR222 transfected H460 cells as well as total and small enriched extracts of A549 cells.

At last, the discrimination between Gram-negative and Gram-positive bacteria was carried out, exploiting their different cellular composition, especially concerning the outer membranes, and the difference in the production of the biofilm matrix. *E. coli* and *S. epidermidis* were respectively chosen as representative for the above mentioned categories. The entire vibrational patterns of both bacteria was successfully labelled, highlighting the differences related to the outer membrane structural components. Moreover, the metabolic evolution of both bacterial strains was monitored to investigate the development of the culture over time.

In conclusion, in this work the potentialities of the pSi-based SERS substrates were exploited in different bioanalytical fields of application, thanks to the great efficiency and reliability of these platforms. Such characteristics allowed the development of an assay for the label-free detection of miR222, whose application have been extended to real biological samples, as well as the *in-situ* discrimination of different bacterial strains, highlighting the versatility of the developed nanostructures, that in terms of SERS performance, showed high sensitivity, good homogeneity and cheap fabrication processes.

References

1. Fleischmann, M.; Hendra, P. J.; McQuillan, A. J. Raman spectra of pyridine adsorbed at a silver electrode. *Chem. Phys. Lett.* **1974**, *26*, 163–166, doi:10.1016/0009-2614(74)85388-1.
2. Kneipp, K.; Wang, Y.; Kneipp, H.; Perelman, L. T.; Itzkan, I.; Dasari, R. R.; Feld, M. S. Single Molecule Detection Using Surface-Enhanced Raman Scattering (SERS). *Indian J. Urol.* **1997**, *18*, 195–197.
3. Maier, S. A. *Plasmonics : fundamentals and applications*; Springer, 2007; ISBN 9781441941138.
4. Baffou, G.; Quidant, R. Thermo-plasmonics: Using metallic nanostructures as nano-sources of heat. *Laser Photonics Rev.* **2013**, *7*, 171–187, doi:10.1002/lpor.201200003.
5. Schlücker, S. Surface-Enhanced Raman Spectroscopy : Concepts and Chemical Applications Angewandte. *Angew. Chemie Int. Ed.* **2014**, *53*, 4756–4795, doi:10.1002/anie.201205748.
6. Kneipp, K.; Haka, A. S.; Kneipp, H.; Badizadegan, K.; Yoshizawa, N.; Boone, C.; Shafer-Peltier, K. E.; Motz, J. T.; Dasari, R. R.; Feld, M. S. Surface-enhanced raman spectroscopy in single living cells using gold nanoparticles. *Appl. Spectrosc.* **2002**, *56*, 150–154, doi:10.1366/0003702021954557.
7. Njoki, P. N.; Lim, I. I. S.; Mott, D.; Park, H. Y.; Khan, B.; Mishra, S.; Sujakumar, R.; Luo, J.; Zhong, C. J. Size correlation of optical and spectroscopic properties for gold nanoparticles. *J. Phys. Chem. C* **2007**, *111*, 14664–14669, doi:10.1021/jp074902z.
8. Haes, A. J.; Haynes, C. L.; Mcfarland, A. D.; Schatz, G. C. P lasmonic Materials for Surface-Enhanced Sensing and. *MRS Bull.* **2005**, *30*, 368–375, doi:10.1557/mrs2005.100.
9. Gangadharan, D. T.; Xu, Z.; Liu, Y.; Izquierdo, R.; Ma, D. Recent advancements in plasmon-enhanced promising third-generation solar cells. *Nanophotonics* **2017**, *6*, 153–175, doi:10.1515/nanoph-2016-0111.
10. Camden, J. P.; Dieringer, J. A.; Wang, Y.; Masiello, D. J.; Marks, L. D.; Schatz, G. C.; Van Duyne, R. P. Probing the structure of single-molecule surface-enhanced Raman scattering hot spots. *J. Am. Chem. Soc.* **2008**, *130*, 12616–12617, doi:10.1021/ja8051427.
11. Grésillon, S.; Aigouy, L.; Boccara, A. C.; Rivoal, J. C.; Quelin, X.; Desmarest, C.; Gadenne, P.; Shubin, V. A.; Sarychev, A. K.; Shalaev, V. M. Experimental observation of localized optical excitations in random metal-dielectric films. *Phys. Rev. Lett.* **1999**, *82*, 4520–4523, doi:10.1103/PhysRevLett.82.4520.
12. Halas, N. J.; Lal, S.; Chang, W. S.; Link, S.; Nordlander, P. Plasmons in strongly coupled metallic nanostructures. *Chem. Rev.* **2011**, *111*, 3913–3961, doi:10.1021/cr200061k.
13. Radziuk, D.; Moehwald, H. Prospects for plasmonic hot spots in single molecule SERS towards the chemical imaging of live cells. *Phys. Chem. Chem. Phys.* **2015**, *17*, 21072–21093, doi:10.1039/c4cp04946b.
14. Le Ru, E. C.; Etchegoin, P. G. Phenomenological local field enhancement factor distributions around electromagnetic hot spots. *J. Chem. Phys.* **2009**,

130, doi:10.1063/1.3138784.

15. Kessentini, S.; Barchiesi, D.; D'Andrea, C.; Toma, A.; Guillot, N.; Di Fabrizio, E.; Fazio, B.; Maragó, O. M.; Gucciardi, P. G.; Lamy De La Chapelle, M. Gold dimer nanoantenna with slanted gap for tunable LSPR and improved SERS. *J. Phys. Chem. C* **2014**, *118*, 3209–3219, doi:10.1021/jp409844y.
16. Matthew Rycenga, Claire M. Cobley, Jie Zeng, Weiyang Li, Christine H. Moran, Qiang Zhang, Dong Qin, Y. X. Controlling the Synthesis and Assembly of Silver Nanostructures for Plasmonic Applications. *Chem. Eng. J.* **2011**, *6*, 3669–3712, doi:10.1038/jid.2014.371.
17. Herzog, J. B.; Knight, M. W.; Li, Y.; Evans, K. M.; Halas, N. J.; Natelson, D. Dark plasmons in hot spot generation and polarization in interelectrode nanoscale junctions. *Nano Lett.* **2013**, *13*, 1359–1364, doi:10.1021/nl400363d.
18. Langer, J.; Jimenez de Aberasturi, D.; Aizpurua, J.; Alvarez-Puebla, R. A.; Auguié, B.; Baumberg, J. J.; Bazan, G. C.; Bell, S. E. J.; Boisen, A.; Brolo, A. G.; Choo, J.; Cialla-May, D.; Deckert, V.; Fabris, L.; Faulds, K.; García de Abajo, F. J.; Goodacre, R.; Graham, D.; Haes, A. J.; Haynes, C. L.; Huck, C.; Itoh, T.; Käll, M.; Kneipp, J.; Kotov, N. A.; Kuang, H.; Le Ru, E. C.; Lee, H. K.; Li, J.-F.; Ling, X. Y.; Maier, S.; Mayerhoefer, T.; Moskovits, M.; Murakoshi, K.; Nam, J.-M.; Nie, S.; Ozaki, Y.; Pastoriza-Santos, I.; Perez-Juste, J.; Popp, J.; Pucci, A.; Reich, S.; Ren, B.; Schatz, G. C.; Shegai, T.; Schlücker, S.; Li-Lin, T.; Thomas, K. G.; Tian, Z.-Q.; Van Duyne, R. P.; Vo-Dinh, T.; Wang, Y.; Willets, K. A.; Xu, C.; Xu, H.; Xu, Y.; Yamamoto, Y. S.; Zhao, B.; Liz-Marzán, L. M. Present and Future of Surface Enhanced Raman Scattering. *ACS Nano* **2019**, doi:10.1021/acsnano.9b04224.
19. Otto, A. The "chemical" (electronic) contribution to surface-enhanced Raman scattering. *J. Raman Spectrosc.* **2005**, *36*, 497–509, doi:10.1002/jrs.1355.
20. Kneipp, K. Chemical Contribution to SERS Enhancement: An Experimental Study on a Series of Polymethine Dyes on Silver Nanoaggregates. *J. Phys. Chem. C* **2016**, *120*, 21076–21081, doi:10.1021/acs.jpcc.6b03785.
21. Valley, N.; Greeneltch, N.; Van Duyne, R. P.; Schatz, G. C. A look at the origin and magnitude of the chemical contribution to the enhancement mechanism of surface-enhanced Raman spectroscopy (SERS): Theory and experiment. *J. Phys. Chem. Lett.* **2013**, *4*, 2599–2604, doi:10.1021/jz4012383.
22. Zong, C.; Xu, M.; Xu, L. J.; Wei, T.; Ma, X.; Zheng, X. S.; Hu, R.; Ren, B. Surface-Enhanced Raman Spectroscopy for Bioanalysis: Reliability and Challenges. *Chem. Rev.* **2018**, *118*, 4946–4980, doi:10.1021/acs.chemrev.7b00668.
23. Xia, Y.; Xiong, Y.; Lim, B.; Skrabalak, S. E. Shape-controlled synthesis of metal nanocrystals: Simple chemistry meets complex physics? *Angew. Chemie - Int. Ed.* **2009**, *48*, 60–103, doi:10.1002/anie.200802248.
24. Lee, P. C.; Meisel, D. Adsorption and surface-enhanced Raman of dyes on silver and gold sols. *J. Phys. Chem.* **1982**, *86*, 3391–3395, doi:10.1021/j100214a025.
25. Meng, W.; Hu, F.; Jiang, X.; Lu, L. Preparation of silver colloids with improved uniformity and stable surface-enhanced Raman scattering. *Nanoscale Res. Lett.* **2015**, *10*, 1–8, doi:10.1186/s11671-015-0746-1.
26. Steinigeweg, D.; Schlücker, S. Monodispersity and size control in the

synthesis of 20-100 nm quasi-spherical silver nanoparticles by citrate and ascorbic acid reduction in glycerol-water mixtures. *Chem. Commun.* **2012**, *48*, 8682–8684, doi:10.1039/c2cc33850e.

27. Millstone, J. E.; Hurst, S. J.; Métraux, G. S.; Cutler, J. I.; Mirkin, C. A. Colloidal gold and silver triangular nanoprisms. *Small* **2009**, *5*, 646–664, doi:10.1002/smll.200801480.
28. Mao, A.; Jin, X.; Gu, X.; Wei, X.; Yang, G. Rapid, green synthesis and surface-enhanced Raman scattering effect of single-crystal silver nanocubes. *J. Mol. Struct.* **2012**, *1021*, 158–161, doi:10.1016/j.molstruc.2012.04.043.
29. Wiley, B.; Sun, Y.; Xia, Y. Synthesis of silver nanostructures with controlled shapes and properties. *Acc. Chem. Res.* **2007**, *40*, 1067–1076, doi:10.1021/ar7000974.
30. Spadavecchia, J.; Barras, A.; Lyskawa, J.; Woisel, P.; Laure, W.; Pradier, C. M.; Boukherroub, R.; Szunerits, S. Approach for plasmonic based DNA sensing: Amplification of the wavelength shift and simultaneous detection of the plasmon modes of gold nanostructures. *Anal. Chem.* **2013**, *85*, 3288–3296, doi:10.1021/ac3036316.
31. Cañamares, M. V.; Garcia-Ramos, J. V.; Gómez-Varga, J. D.; Domingo, C.; Sanchez-Cortes, S. Comparative study of the morphology, aggregation, adherence to glass, and surface-enhanced Raman scattering activity of silver nanoparticles prepared by chemical reduction of Ag+ using citrate and hydroxylamine. *Langmuir* **2005**, *21*, 8546–8553, doi:10.1021/la050030l.
32. Bell, S. E. J.; McCourt, M. R. SERS enhancement by aggregated Au colloids: effect of particle size. *Phys. Chem. Chem. Phys.* **2009**, *11*, 7348–7349, doi:10.1039/b913171j.
33. Boken, J.; Soni, S. K.; Kumar, D. Microfluidic Synthesis of Nanoparticles and their Biosensing Applications. *Crit. Rev. Anal. Chem.* **2016**, *46*, 538–561, doi:10.1080/10408347.2016.1169912.
34. Fraire, J. C.; Sueldo Ocello, V. N.; Allende, L. G.; Veglia, A. V.; Coronado, E. A. Toward the design of highly stable small colloidal SERS substrates with supramolecular host-guest interactions for ultrasensitive detection. *J. Phys. Chem. C* **2015**, *119*, 8876–8888, doi:10.1021/acs.jpcc.5b01647.
35. Fan, M.; Andrade, G. F. S.; Brolo, A. G. A review on the fabrication of substrates for surface enhanced Raman spectroscopy and their applications in analytical chemistry. *Anal. Chim. Acta* **2011**, *693*, 7–25, doi:10.1016/j.aca.2011.03.002.
36. Cottat, M.; Lidgi-Guigui, N.; Tijunelyte, I.; Barbillon, G.; Hamouda, F.; Gogol, P.; Aassime, A.; Lourtioz, J. M.; Bartenlian, B.; de la Chapelle, M. L. Soft UV nanoimprint lithography-designed highly sensitive substrates for SERS detection. *Nanoscale Res. Lett.* **2014**, *9*, 1–6, doi:10.1186/1556-276X-9-623.
37. Jahn, M.; Patze, S.; Hidi, I. J.; Knipper, R.; Radu, A. I.; Mühlig, A.; Yüksel, S.; Peksa, V.; Weber, K.; Mayerhöfer, T.; Cialla-May, D.; Popp, J. Plasmonic nanostructures for surface enhanced spectroscopic methods. *Analyst* **2016**, *141*, 756–793, doi:10.1039/c5an02057c.
38. Gunnarsson, L.; Bjerneld, E. J.; Xu, H.; Petronis, S.; Kasemo, B.; Käll, M. Interparticle coupling effects in nanofabricated substrates for surface-enhanced Raman scattering. *Appl. Phys. Lett.* **2001**, *78*, 802–804, doi:10.1063/1.1344225.
39. Sow, I.; Grand, J.; Lévi, G.; Aubard, J.; Félidj, N.; Tinguely, J. C.; Hohenau, A.; Krenn, J. R. Revisiting surface-enhanced raman scattering on realistic

lithographic gold nanostripes. *J. Phys. Chem. C* **2013**, *117*, 25650–25658, doi:10.1021/jp407983h.

40. Kahl, M.; Voges, E.; Kostrewa, S.; Viets, C.; Hill, W. Periodically structured metallic substrates for SERS. *Sensors Actuators, B Chem.* **1998**, *51*, 285–291, doi:10.1016/S0925-4005(98)00219-6.
41. Wu, D. Y.; Li, J. F.; Ren, B.; Tian, Z. Q. Electrochemical surface-enhanced Raman spectroscopy of nanostructures. *Chem. Soc. Rev.* **2008**, *37*, 1025–1041, doi:10.1039/b707872m.
42. Haynes, C. L.; Van Duyne, R. P. Nanosphere lithography: A versatile nanofabrication tool for studies of size-dependent nanoparticle optics. *J. Phys. Chem. B* **2001**, *105*, 5599–5611, doi:10.1021/jp010657m.
43. Giallongo, G.; Durante, C.; Pilot, R.; Garoli, D.; Bozio, R.; Romanato, F.; Gennaro, A.; Rizzi, G. A.; Granozzi, G. Growth and optical properties of silver nanostructures obtained on connected anodic aluminum oxide templates. *Nanotechnology* **2012**, *23*, doi:10.1088/0957-4484/23/32/325604.
44. Yao, J. L.; Pan, G. P.; Xue, K. H.; Wu, D. Y.; Ren, B.; Sun, D. M.; Tang, J.; Xu, X.; Tian, Z. Q. A complementary study of surface-enhanced Raman scattering and metal nanorod arrays. *Pure Appl. Chem.* **2000**, *72*, 221–228, doi:10.1351/pac200072010221.
45. Cheng, H. W.; Huan, S. Y.; Wu, H. L.; Shen, G. L.; Yu, R. Q. Surface-enhanced Raman spectroscopic detection of a bacteria biomarker using gold nanoparticle immobilized substrates. *Anal. Chem.* **2009**, *81*, 9902–9912, doi:10.1021/ac9014275.
46. Peng, C.; Song, Y.; Wei, G.; Zhang, W.; Li, Z.; Dong, W. F. Self-assembly of λ-DNA networks/Ag nanoparticles: Hybrid architecture and active-SERS substrate. *J. Colloid Interface Sci.* **2008**, *317*, 183–190, doi:10.1016/j.jcis.2007.09.017.
47. Wang, H.; Kundu, J.; Halas, N. J. Plasmonic nanoshell arrays combine surface-enhanced vibrational spectroscopies on a single substrate. *Angew. Chemie - Int. Ed.* **2007**, *46*, 9040–9044, doi:10.1002/anie.200702072.
48. Fan, M.; Brolo, A. G. Silver nanoparticles self assembly as SERS substrates with near single molecule detection limit. *Phys. Chem. Chem. Phys.* **2009**, *11*, 7381–7389, doi:10.1039/b904744a.
49. Yan, J.; Han, X.; He, J.; Kang, L.; Zhang, B.; Du, Y.; Zhao, H.; Dong, C.; Wang, H. L.; Xu, P. Highly sensitive surface-enhanced Raman spectroscopy (SERS) platforms based on silver nanostructures fabricated on polyaniline membrane surfaces. *ACS Appl. Mater. Interfaces* **2012**, *4*, 2752–2756, doi:10.1021/am300381v.
50. Zhang, Q.; Xu, J. J.; Liu, Y.; Chen, H. Y. In-situ synthesis of poly(dimethylsiloxane)-gold nanoparticles composite films and its application in microfluidic systems. *Lab Chip* **2008**, *8*, 352–357, doi:10.1039/b716295m.
51. Harraz, F. A.; Tsuboi, T.; Sasano, J.; Sakka, T.; Ogata, Y. H. Metal Deposition onto a Porous Silicon Layer by Immersion Plating from Aqueous and Nonaqueous Solutions. *J. Electrochem. Soc.* **2002**, *149*, C456, doi:10.1149/1.1498841.
52. Uhlir, A. Electrolytic Shaping of Germanium and Silicon. *Bell Syst. Tech. J.* **1956**, *35*, 333–347, doi:10.1002/j.1538-7305.1956.tb02385.x.
53. Lehmann, V.; Gösele, U. Porous silicon formation: A quantum wire effect. *Appl. Phys. Lett.* **1991**, *58*, 856–858, doi:10.1063/1.104512.
54. Tsuboi, T.; Sakka, T.; Ogata, Y. H. Metal deposition into a porous silicon

layer by immersion plating: Influence of halogen ions. *J. Appl. Phys.* **1998**, *83*, 4501, doi:10.1063/1.367212.

55. Fukami, K.; Tanaka, Y.; Chourou, M. L.; Sakka, T.; Ogata, Y. H. Filling of mesoporous silicon with copper by electrodeposition from an aqueous solution. *Electrochim. Acta* **2009**, *54*, 2197–2202, doi:10.1016/j.electacta.2008.10.024.
56. Bisi, O.; Ossicini, S.; Pavesi, L. Porous silicon: a quantum sponge structure for silicon based optoelectronics. *Surf. Sci. Rep.* **2000**, 469–471.
57. Novara, C. Silver nanostructures on porous silicon for multiplexed Surface Enhanced Raman Scattering biosensing platforms. **2016**.
58. Chan, S.; Kwon, S.; Koo, T. W.; Lee, L. P.; Berlin, A. A. Surface-Enhanced Raman Scattering of Small Molecules from Silver-Coated Silicon Nanopores. *Adv. Mater.* **2003**, *15*, 1595–1598, doi:10.1002/adma.200305149.
59. Giorgis, F.; Descrovi, E.; Chiodoni, A.; Froner, E.; Scarpa, M.; Venturello, A.; Geobaldo, F. Porous silicon as efficient surface enhanced Raman scattering (SERS) substrate. *Appl. Surf. Sci.* **2008**, *254*, 7494–7497, doi:10.1016/j.apsusc.2008.06.029.
60. Ye, W.; Shen, C.; Tian, J.; Wang, C.; Bao, L.; Gao, H. Self-assembled synthesis of SERS-active silver dendrites and photoluminescence properties of a thin porous silicon layer. *Electrochem. commun.* **2008**, *10*, 625–629, doi:10.1016/j.elecom.2008.01.040.
61. Bandarenka, H. V.; Girel, K. V.; Zavatski, S. A.; Panarin, A.; Terekhov, S. N. Progress in the development of SERS-active substrates based on metal-coated porous silicon. *Materials (Basel).* **2018**, *11*, 1–20, doi:10.3390/ma11050852.
62. Kosovic, M.; Balarin, M.; Ivanda, M.; Derek, V.; Marcius, M.; Ristic, M.; Gamulin, O. Porous silicon covered with silver nanoparticles as Surface-Enhanced Raman Scattering (SERS) substrate for ultra-low concentration detection. *Appl. Spectrosc.* **2015**, *69*, 1417–1424, doi:10.1366/14-07729.
63. Virga, A.; Rivolo, P.; Frascella, F.; Angelini, A.; Descrovi, E.; Geobaldo, F.; Giorgis, F. Silver nanoparticles on porous silicon: Approaching single molecule detection in resonant SERS regime. *J. Phys. Chem. C* **2013**, *117*, 20139–20145, doi:10.1021/jp405117p.
64. Bandarenka, H.; Artsemyeva, K.; Redko, S.; Panarin, A.; Terekhov, S.; Bondarenko, V. Effect of swirl-like resistivity striations in n+-type Sb doped Si wafers on the properties of Ag/porous silicon SERS substrates. *Phys. Status Solidi Curr. Top. Solid State Phys.* **2013**, *10*, 624–627, doi:10.1002/pssc.201200731.
65. Li, L.-L.; Li, X.; Wang, H. Microfluidic Synthesis of Nanomaterials for Biomedical Applications. *Small Methods* **2017**, *1*, 1700140, doi:10.1002/smtd.201700140.
66. Marre, S.; Jense, K. F. Synthesis of micro and nanostructures in microfluidic systems. *R. Soc. Chem.* **2010**, *39*, 1183–1202, doi:10.1039/b821324k.
67. Lee, J. N.; Park, C.; Whitesides, G. M. Solvent Compatibility of Poly(dimethylsiloxane)-Based Microfluidic Devices. *Anal. Chem.* **2003**, *75*, 6544–6554, doi:10.1021/ac0346712.
68. Boken, J.; Soni, S. K.; Kumar, D. Microfluidic Synthesis of Nanoparticles and their Biosensing Applications. *Crit. Rev. Anal. Chem.* **2016**, *46*, 538–561, doi:10.1080/10408347.2016.1169912.
69. Bayraktar, T.; Pidugu, S. B. Characterization of liquid flows in microfluidic

systems. *Int. J. Heat Mass Transf.* **2006**, *49*, 815–824, doi:10.1016/j.ijheatmasstransfer.2005.11.007.

70. Wagner, J.; Köhler, J. M. Continuous synthesis of gold nanoparticles in a microreactor. *Nano Lett.* **2005**, *5*, 685–691, doi:10.1021/nl050097t.
71. Wagner, J.; Tshikhudo, T. R.; Köhler, J. M. Microfluidic generation of metal nanoparticles by borohydride reduction. *Chem. Eng. J.* **2007**, *135*, 104–109, doi:10.1016/j.cej.2007.07.046.
72. Lawanstiend, D.; Gatemala, H.; Nootchanat, S.; Eakasit, S.; Wongravee, K.; Srisa-Art, M. Microfluidic approach for in situ synthesis of nanoporous silver microstructures as on-chip SERS substrates. *Sensors Actuators, B Chem.* **2018**, *270*, 466–474, doi:10.1016/j.snb.2018.05.051.
73. López-Lorente, Á. I.; Valcárcel, M.; Mizaikoff, B. Continuous flow synthesis and characterization of tailor-made bare gold nanoparticles for use in SERS. *Microchim. Acta* **2014**, *181*, 1101–1108, doi:10.1007/s00604-014-1215-8.
74. Jahn, I. J.; Žukovskaja, O.; Zheng, X. S.; Weber, K.; Bocklitz, T. W.; Cialla-May, D.; Popp, J. Surface-enhanced Raman spectroscopy and microfluidic platforms: Challenges, solutions and potential applications. *Analyst* **2017**, *142*, 1022–1047, doi:10.1039/c7an00118e.
75. Parisi, J.; Su, L.; Lei, Y. In situ synthesis of silver nanoparticle decorated vertical nanowalls in a microfluidic device for ultrasensitive in-. *Lab Chip* **2013**, 1501–1508, doi:10.1039/c3lc41249k.
76. Leem, J.; Kang, H. W.; Ko, S. H.; Sung, H. J. Controllable Ag nanostructure patterning in a micro fl uidic channel for real-time SERS systems †. *Nanoscale* **2014**, *6*, 2895–2901, doi:10.1039/c3nr04829b.
77. Zhao, H. Z.; Xu, Y.; Wang, C. Y.; Wang, R.; Xiang, S. T.; Chen, L. Design and fabrication of a microfluidic SERS chip with integrated Ag film@nanoAu. *RSC Adv.* **2016**, *6*, 14105–14111, doi:10.1039/c5ra25018h.
78. Streets, A. M.; Huang, Y. Microfluidics for biological measurements with single-molecule resolution. *Curr. Opin. Biotechnol.* **2014**, *25*, 69–77, doi:10.1016/j.copbio.2013.08.013.
79. Gao, R.; Cheng, Z.; Demello, A. J.; Choo, J. Wash-free magnetic immunoassay of the PSA cancer marker using SERS and droplet microfluidics. *Lab Chip* **2016**, *16*, 1022–1029, doi:10.1039/c5lc01249j.
80. Guo, M. T.; Rotem, A.; Heyman, J. A.; Weitz, D. A. Droplet microfluidics for high-throughput biological assays. *Lab Chip* **2012**, *12*, 2146–2155, doi:10.1039/c2lc21147e.
81. Yazdi, S. H.; Giles, K. L.; White, I. M. Multiplexed Detection of DNA Sequences Using a Competitive Displacement Assay in a Micro fl uidic SERRS-Based Device. **2013**, doi:10.1021/ac402744z.
82. Zhou, J.; Ren, K.; Zhao, Y.; Dai, W.; Wu, H. Convenient formation of nanoparticle aggregates on microfluidic chips for highly sensitive SERS detection of biomolecules. *Anal. Bioanal. Chem.* **2012**, *402*, 1601–9, doi:10.1007/s00216-011-5585-z.
83. Novara, C.; Chiadò, A.; Paccotti, N.; Catuogno, S.; Esposito, C. L.; Condorelli, G.; De Franciscis, V.; Geobaldo, F.; Rivolo, P.; Giorgis, F. SERS-active metal-dielectric nanostructures integrated in microfluidic devices for label-free quantitative detection of miRNA. *Faraday Discuss.* **2017**, *205*, 271–289, doi:10.1039/c7fd00140a.
84. Kim, W. H.; Lee, J. U.; Song, S.; Kim, S.; Choi, Y. J.; Sim, S. J. A label-free, ultra-highly sensitive and multiplexed SERS nanoplasmonic biosensor

for miRNA detection using a head-flocked gold nanopillar. *Analyst* **2019**, *144*, 1768–1776, doi:10.1039/c8an01745j.

85. Wang, H. N.; Crawford, B. M.; Fales, A. M.; Bowie, M. L.; Seewaldt, V. L.; Vo-Dinh, T. Multiplexed Detection of MicroRNA Biomarkers Using SERS-Based Inverse Molecular Sentinel (iMS) Nanoprobes. *J. Phys. Chem. C* **2016**, *120*, 21047–21055, doi:10.1021/acs.jpcc.6b03299.
86. Matteini, P.; Cottat, M.; Tavanti, F.; Panfilova, E.; Scuderi, M.; Nicotra, G.; Menziani, M. C.; Khlebtsov, N.; De Angelis, M.; Pini, R. Site-Selective Surface-Enhanced Raman Detection of Proteins. *ACS Nano* **2017**, *11*, 918–926, doi:10.1021/acsnano.6b07523.
87. Paccotti, N.; Boschetto, F.; Horiguchi, S.; Marin, E.; Chiadò, A.; Novara, C.; Geobaldo, F.; Giorgis, F.; Pezzotti, G. Label-Free SERS Discrimination and In Situ Analysis of Life Cycle in Escherichia coli and Staphylococcus epidermidis. *Biosensors* **2018**, *8*, 131, doi:10.3390/bios8040131.
88. Lemma, T.; Saliniemi, A.; Hynninen, V.; Hytönen, V. P.; Toppari, J. J. SERS detection of cell surface and intracellular components of microorganisms using nano-aggregated Ag substrate. *Vib. Spectrosc.* **2016**, *83*, 36–45, doi:10.1016/j.vibspec.2016.01.006.
89. Neugebauer, U.; Schmid, U.; Baumann, K.; Ziebuhr, W.; Kozitskaya, S.; Deckert, V.; Schmitt, M.; Popp, J. Towards a detailed understanding of bacterial metabolism - Spectroscopic characterization of Stophylococcus epidermidis. *ChemPhysChem* **2007**, *8*, 124–137, doi:10.1002/cphc.200600507.
90. Efrima, S.; Zeiri, L. Understanding SERS of bacteria. *J. Raman Spectrosc.* **2009**, *40*, 277–288, doi:10.1002/jrs.2121.
91. Zeiri, L.; Bronk, B. V.; Shabtai, Y.; Czégé, J.; Efrima, S. Silver metal induced surface enhanced Raman of bacteria. *Colloids Surfaces A Physicochem. Eng. Asp.* **2002**, *208*, 357–362, doi:10.1016/S0927-7757(02)00162-0.
92. Shanmukh, S.; Jones, L.; Driskell, J.; Zhao, Y.; Dluhy, R.; Tripp, R. A. Rapid and sensitive detection of respiratory virus molecular signatures using a silver nanorod array SERS substrate. *Nano Lett.* **2006**, *6*, 2630–2636, doi:10.1021/nl061666f.
93. Cialla, D.; Deckert-Gaudig, T.; Budich, C.; Laue, M.; Möller, R.; Naumann, D.; Deckert, V.; Popp, J. Raman to the limit: Tip-enhanced Raman spectroscopic investigations of a single tobacco mosaic virus. *J. Raman Spectrosc.* **2009**, *40*, 240–243, doi:10.1002/jrs.2123.
94. Olschewski, K.; Kämmer, E.; Stöckel, S.; Bocklitz, T.; Deckert-Gaudig, T.; Zell, R.; Cialla-May, D.; Weber, K.; Deckert, V.; Popp, J. A manual and an automatic TERS based virus discrimination. *Nanoscale* **2015**, *7*, 4545–4552, doi:10.1039/c4nr07033j.
95. Ferhan, A. R.; Jackman, J. A.; Park, J. H.; Cho, N. J. Nanoplasmonic sensors for detecting circulating cancer biomarkers. *Adv. Drug Deliv. Rev.* **2018**, *125*, 48–77, doi:10.1016/j.addr.2017.12.004.
96. Paul, A. M.; Fan, Z.; Sinha, S. S.; Shi, Y.; Le, L.; Bai, F.; Ray, P. C. Bioconjugated Gold Nanoparticle Based SERS Probe for Ultrasensitive Identification of Mosquito-Borne Viruses Using Raman Fingerprinting. *J. Phys. Chem. C* **2015**, *119*, 23669–23675, doi:10.1021/acs.jpcc.5b07387.
97. Lane, L. A.; Qian, X.; Nie, S. SERS Nanoparticles in Medicine: From Label-Free Detection to Spectroscopic Tagging. *Chem. Rev.* **2015**, *115*, 10489–10529, doi:10.1021/acs.chemrev.5b00265.

98. Sha, M. Y.; Xu, H.; Natan, M. J.; Cromer, R. Surface-enhanced raman scattering tags for rapid and homogeneous detection of circulating tumor cells in the presence of human whole blood. *J. Am. Chem. Soc.* **2008**, *130*, 17214–17215, doi:10.1021/ja804494m.
99. Podstawka, E.; Ozaki, Y.; Proniewicz, L. M. Adsorption of S-S containing proteins on a colloidal silver surface studied by surface-enhanced Raman spectroscopy. *Appl. Spectrosc.* **2004**, *58*, 1147–1156, doi:10.1366/0003702042336073.
100. Grabbe, E. S.; Buck, R. P. Surface-Enhanced Raman Spectroscopic Investigation of Human Immunoglobulin G Adsorbed on a Silver Electrode. *J. Am. Chem. Soc.* **1989**, *111*, 8362–8366, doi:10.1021/ja00204a006.
101. Lu, W.; Wang, Y.; Cao, X.; Li, L.; Dong, J.; Qian, W. Multiplexing determination of lung cancer biomarkers using electrochemical and surface-enhanced Raman spectroscopic techniques. *New J. Chem.* **2015**, *39*, 5420–5430, doi:10.1039/c5nj00445d.
102. Otto, C.; Van den Tweel, T. J. J.; De Mul, F. F. M.; Greve, J. Surf ace-Enhanced Raman Spectroscopy of DNA Bases. *J. Raman Spectrosc.* **1986**, *17*, 289–298.
103. Suh, J. S.; Moskovits, M. Surface-Enhanced Raman Spectroscopy of Amino Acids and Nucleotide Bases Adsorbed on Silver. *J. Am. Chem. Soc.* **1986**, *108*, 4711–4718, doi:10.1021/ja00276a005.
104. Najjar, S.; Talaga, D.; Schué, L.; Coffinier, Y.; Szunerits, S.; Boukherroub, R.; Servant, L.; Rodriguez, V.; Bonhommeau, S. Tip-enhanced raman spectroscopy of combed double-stranded DNA bundles. *J. Phys. Chem. C* **2014**, *118*, 1174–1181, doi:10.1021/jp410963z.
105. Bailo, E.; Deckert, V. Tip-enhanced Raman spectroscopy of single RNA strands: Towards a novel direct-sequencing method. *Angew. Chemie - Int. Ed.* **2008**, *47*, 1658–1661, doi:10.1002/anie.200704054.
106. Stofer, E.; Chipot, C.; Lavery, R. Free energy calculations of watson-crick base pairing in aqueous solution. *J. Am. Chem. Soc.* **1999**, *121*, 9503–9508, doi:10.1021/ja991092z.
107. Dong, H.; Lei, J.; Ding, L.; Wen, Y.; Ju, H.; Zhang, X. MicroRNA: Function, detection, and bioanalysis. *Chem. Rev.* **2013**, *113*, 6207–6233, doi:10.1021/cr300362f.
108. Barhoumi, A.; Halas, N. J. Label-free detection of DNA hybridization using surface enhanced Raman spectroscopy. *J. Am. Chem. Soc.* **2010**, *132*, 12792–12793, doi:10.1021/ja105678z.
109. Guerrini, L.; Krpetić, Ž.; Van Lierop, D.; Alvarez-Puebla, R. A.; Graham, D. Direct surface-enhanced Raman scattering analysis of DNA duplexes. *Angew. Chemie - Int. Ed.* **2015**, *54*, 1144–1148, doi:10.1002/anie.201408558.
110. Griffiths-Jones, S.; Saini, H. K.; Van Dongen, S.; Enright, A. J. miRBase: Tools for microRNA genomics. *Nucleic Acids Res.* **2008**, *36*, 154–158, doi:10.1093/nar/gkm952.
111. Ameres, S. L.; Martinez, J.; Schroeder, R. Molecular Basis for Target RNA Recognition and Cleavage by Human RISC. *Cell* **2007**, *130*, 101–112, doi:10.1016/j.cell.2007.04.037.
112. Ha, M.; Kim, V. N. Regulation of microRNA biogenesis. *Nat. Rev. Mol. Cell Biol.* **2014**, *15*, 509–524, doi:10.1038/nrm3838.
113. Lin, S.; Gregory, R. I. MicroRNA biogenesis pathways in cancer HHS Public Access. *Nat Rev Cancer* **2015**, *15*, 321–333, doi:10.1038/nrc3932.

114. Srivastava, A.; Suy, S.; Collins, S. P.; Kumar, D. Circulating MicroRNA as Biomarkers: An Update in Prostate Cancer. *Mol. Cell. Pharmacol.* **2011**, *23*, 1–7, doi:10.1038/jid.2014.371.

115. Skog, J.; Wurdinger, T.; Van Rijn, S.; Meijer, D.; Gainche, L.; Sena-Esteves, M.; Curry Jr, W. T.; Carter, R. S.; Krichevsky, A. M.; Breakfield, X. O. Glioblastoma microvesicles transport RNA and protein that promote tumor growth and provide diagnostic biomarkers. *Nat. Cell Biol.* **2008**, 1470–1476, doi:10.1097/CCM.0b013e31823da96d.Hydrogen.

116. Wark, A. W.; Lee, H. J.; Corn, R. M. Multiplexed detection methods for profiling microRNA expression in biological samples. *Angew. Chemie - Int. Ed.* **2008**, *47*, 644–652, doi:10.1002/anie.200702450.

117. Li, W.; Ruan, K. MicroRNA detection by microarray. *Anal. Bioanal. Chem.* **2009**, *394*, 1117–1124, doi:10.1007/s00216-008-2570-2.

118. Driskell, J. D.; Seto, A. G.; Jones, L. P.; Jokela, S.; Dluhy, R. A.; Zhao, Y. P.; Tripp, R. A. Rapid microRNA (miRNA) detection and classification via surface-enhanced Raman spectroscopy (SERS). *Biosens. Bioelectron.* **2008**, *24*, 917–922, doi:10.1016/j.bios.2008.07.060.

119. Chiadò, A.; Novara, C.; Lamberti, A.; Geobaldo, F.; Giorgis, F.; Rivolo, P. Immobilization of Oligonucleotides on Metal-Dielectric Nanostructures for miRNA Detection. *Anal. Chem.* **2016**, *88*, 9554–9563, doi:10.1021/acs.analchem.6b02186.

120. Su, J.; Wang, D.; Nörbel, L.; Shen, J.; Zhao, Z.; Dou, Y.; Peng, T.; Shi, J.; Mathur, S.; Fan, C.; Song, S. Multicolor Gold-Silver Nano-Mushrooms as Ready-to-Use SERS Probes for Ultrasensitive and Multiplex DNA/miRNA Detection. *Anal. Chem.* **2017**, *89*, 2531–2538, doi:10.1021/acs.analchem.6b04729.

121. Song, C. Y.; Yang, Y. J.; Yang, B. Y.; Sun, Y. Z.; Zhao, Y. P.; Wang, L. H. Ultrasensitive SERS sensor for simultaneous detection of multiple cancer-related miRNAs. *Nanoscale* **2016**, *8*, 17365–17373, doi:10.1039/c6nr05504d.

122. Liu, Z.; Cheng, L.; Zhang, L.; Jing, C.; Shi, X.; Yang, Z.; Long, Y.; Fang, J. Large-area fabrication of highly reproducible surface enhanced Raman substrate via a facile double sided tape-assisted transfer approach using hollow Au-Ag alloy nanourchins. *Nanoscale* **2014**, *6*, 2567–2572, doi:10.1039/c3nr05840a.

123. Zhang, H.; Liu, Y.; Gao, J.; Zhen, J. A sensitive SERS detection of miRNA using a label-free multifunctional probe. *Chem. Commun.* **2015**, *51*, 16836–16839, doi:10.1039/c5cc06225j.

124. Hu, M.; Ou, F. S.; Wu, W.; Naumov, I.; Li, X.; Bratkovsky, A. M.; Williams, R. S.; Li, Z. Gold nanofingers for molecule trapping and detection. *J. Am. Chem. Soc.* **2010**, *132*, 12820–12822, doi:10.1021/ja105248h.

125. Park, S. G.; Mun, C. W.; Xiao, X.; Braun, A.; Kim, S.; Giannini, V.; Maier, S. A.; Kim, D. H. Surface Energy-Controlled SERS Substrates for Molecular Concentration at Plasmonic Nanogaps. *Adv. Funct. Mater.* **2017**, *27*, doi:10.1002/adfm.201703376.

126. Lee, J. U.; Kim, W. H.; Lee, H. S.; Park, K. H.; Sim, S. J. Quantitative and Specific Detection of Exosomal miRNAs for Accurate Diagnosis of Breast Cancer Using a Surface-Enhanced Raman Scattering Sensor Based on Plasmonic Head-Flocked Gold Nanopillars. *Small* **2019**, *15*, doi:10.1002/smll.201804968.

127. Novara, C.; Lamberti, A.; Chiadò, A.; Virga, A.; Rivolo, P.; Geobaldo, F.;

Giorgis, F. Surface-enhanced Raman spectroscopy on porous silicon membranes decorated with Ag nanoparticles integrated in elastomeric microfluidic chips. *RSC Adv.* **2016**, *6*, 21865–21870, doi:10.1039/c5ra26746c.

128. Wang, Z.; Zong, S.; Wang, Z.; Wu, L.; Chen, P.; Yun, B.; Cui, Y. Microfluidic chip based micro RNA detection through the combination of fluorescence and surface enhanced Raman scattering techniques. *Nanotechnology* **2017**, *28*, doi:10.1088/1361-6528/aa527b.
129. Tyagi, S.; Kramer, F. R. Molecular Beacons: Probes that Fluoresce Upon Hybridization. *Nat. Biotechnol.* **1996**, *14*, 303–308, doi:10.1038/nbt0396-303.
130. Mack, D.; Rohde, H.; Harris, L. G.; Davies, A. P.; Horstkotte, M. A.; Knobloch, J. K. M. Biofilm formation in medical device-related infection. *Int. J. Artif. Organs* **2006**, *29*, 343–359, doi:10.1037/ccp0000057.
131. Fan, C.; Hu, Z.; Mustapha, A.; Lin, M. Rapid detection of food- and waterborne bacteria using surface-enhanced Raman spectroscopy coupled with silver nanosubstrates. *Appl. Microbiol. Biotechnol.* **2011**, *92*, 1053–1061, doi:10.1007/s00253-011-3634-3.
132. Jarvis, R. M.; Goodacre, R. Characterisation and identification of bacteria using SERS. *Chem. Soc. Rev.* **2008**, *37*, 931–936, doi:10.1039/b705973f.
133. Mosier-Boss, P. A. Review on SERS of bacteria. *Biosensors* 2017, *7*.
134. Patel, I. S.; Premasiri, W. R.; Moir, D. T.; Ziegler, L. D. Barcoding bacterial cells: A SERS-based methodology for pathogen identification. *J. Raman Spectrosc.* **2008**, *39*, 1660–1672, doi:10.1002/jrs.2064.
135. Fournier, A. M. The Gram stain. *Ann. Intern. Med.* **1998**, *128*, 776, doi:10.7326/0003-4819-128-9-199805010-00015.
136. Lorian, V. The Mode of Action of Antibiotics on Gram-Negative Bacilli. *Arch. Intern. Med.* **1971**, *128*, 623–632, doi:10.1001/archinte.1971.00310220131022.
137. Rollauer, S. E.; Sooreshjani, M. A.; Noinaj, N.; Buchanan, S. K. Outer membrane protein biogenesis in Gram-negative bacteria. *Philos. Trans. R. Soc. B Biol. Sci.* **2015**, *370*, doi:10.1098/rstb.2015.0023.
138. Flemming, H. C.; Wingender, J. The biofilm matrix. *Nat. Rev. Microbiol.* **2010**, *8*, 623–633, doi:10.1038/nrmicro2415.
139. Wood, K. T. Insights on Escherichia coli Biofilm Formation and Inhibition from Whole-Transcriptome Profiling. *Environ. Microbiol.* **2009**, *11*, 1–15, doi:10.1111/j.1462-2920.2008.01768.x.Insights.
140. Lappann, M.; Claus, H.; Van Alen, T.; Harmsen, M.; Elias, J.; Molin, S.; Vogel, U. A dual role of extracellular DNA during biofilm formation of Neisseria meningitidis. *Mol. Microbiol.* **2010**, *75*, 1355–1371, doi:10.1111/j.1365-2958.2010.07054.x.
141. Campoccia, D.; Montanaro, L.; Ravaioli, S.; Pirini, V.; Cangini, I.; Arciola, C. R. Exopolysaccharide production by Staphylococcus epidermidis and its relationship with biofilm extracellular DNA. *Int. J. Artif. Organs* **2011**, *34*, 832–839, doi:10.5301/ijao.5000048.
142. Mosier-Boss, P. Review of SERS Substrates for Chemical Sensing. *Nanomaterials* **2017**, *7*, 142, doi:10.3390/nano7060142.
143. Wang, Y.; Yan, B.; Chen, L. SERS Tags: Novel optical nanoprobes for bioanalysis. *Chem. Rev.* **2013**, *113*, 1391–1428, doi:10.1021/cr300120g.
144. Schwartzberg, A. M.; Zhang, J. Z. Novel Optical Properties and Emerging Applications of Metal Nanostructures? *J. Phys. Chem. C* **2008**, *112*, 10323–

10337, doi:10.1021/jp801770w.

145. Liu, Y.; Zhou, H.; Hu, Z.; Yu, G.; Yang, D.; Zhao, J. Label and label-free based surface-enhanced Raman scattering for pathogen bacteria detection: A review. *Biosens. Bioelectron.* 2017, *94*, 131–140.

146. Efrima, S.; Bronk, B. V. Silver colloids impregnating or coating bacteria. *J. Phys. Chem. B* **1998**, *102*, 5947–5950, doi:10.1021/jp9813903.

147. Zhou, H.; Yang, D.; Ivleva, N. P.; Mircescu, N. E.; Niessner, R.; Haisch, C. SERS detection of bacteria in water by in situ coating with Ag nanoparticles. *Anal. Chem.* **2014**, *86*, 1525–1533, doi:10.1021/ac402935p.

148. Jarvis, R. M.; Brooker, A.; Goodacre, R. Surface-enhanced Raman spectroscopy for bacterial discrimination utilizing a scanning electron microscope with a Raman spectroscopy interface. *Anal. Chem.* **2004**, *76*, 5198–5202, doi:10.1021/ac049663f.

149. Novara, C.; Petracca, F.; Virga, A.; Rivolo, P.; Ferrero, S.; Chiolerio, A.; Geobaldo, F.; Porro, S.; Giorgis, F. SERS active silver nanoparticles synthesized by inkjet printing on mesoporous silicon. *Nanoscale Res. Lett.* **2014**, *9*, 1–7, doi:10.1186/1556-276X-9-527.

150. Lamberti, A.; Virga, A.; Angelini, A.; Ricci, A.; Descrovi, E.; Cocuzza, M.; Giorgis, F. Metal-elastomer nanostructures for tunable SERS and easy microfluidic integration. *RSC Adv.* **2015**, *5*, 4404–4410, doi:10.1039/c4ra12168f.

151. Michota, A.; Bukowska, J. Surface-enhanced Raman scattering (SERS) of 4-mercaptobenzoic acid on silver and gold substrates. *J. Raman Spectrosc.* **2003**, *34*, 21–25, doi:10.1002/jrs.928.

152. Yang, L.; Jiang, X.; Ruan, W.; Zhao, B.; Xu, W.; Lombardi, J. R. Observation of enhanced Raman scattering for molecules adsorbed on TiO 2 nanoparticles: charge-transfer contribution. *J. Phys. Chem. C* **2008**, *112*, 20095–20098, doi:10.1021/jp8074145.

153. Tantra Ratna; Brown, R. J. C.; Milton, M. J. T. Strategy to improve the reproducibility of colloidal SERS. *J. Raman Spectrosc.* **2007**, *38*, 1469–1479.

154. Fabris, L.; Ceder, Y.; Chinnaiyan, A. M.; Jenster, G. W.; Sorensen, K. D.; Tomlins, S.; Visakorpi, T.; Calin, G. A. The Potential of MicroRNAs as Prostate Cancer Biomarkers. *Eur. Urol.* **2016**, *70*, 312–322, doi:10.1016/j.eururo.2015.12.054.

155. Bettazzi, F.; Hamid-Asl, E.; Esposito, C. L.; Quintavalle, C.; Formisano, N.; Laschi, S.; Catuogno, S.; Iaboni, M.; Marrazza, G.; Mascini, M.; Cerchia, L.; De Franciscis, V.; Condorelli, G.; Palchetti, I. Electrochemical detection of miRNA-222 by use of a magnetic bead-based bioassay. *Anal. Bioanal. Chem.* **2013**, *405*, 1025–1034, doi:10.1007/s00216-012-6476-7.

156. Teixeira, A. L.; Silva, J.; Ferreira, M.; Marques, I.; Gomes, M.; Mauricio, J.; Lobo, F.; Medeiros, R. 891 Circulating MicroRNA-222 in Plasma – a Potential Biomarker for Renal Cell Carcinoma. *Eur. J. Cancer* **2012**, *48*, S216, doi:10.1016/s0959-8049(12)71523-x.

157. Steel, A. B.; Levicky, R. L.; Herne, T. M.; Tarlov, M. J. Immobilization of nucleic acids at solid surfaces: Effect of oligonucleotide length on layer assembly. *Biophys. J.* **2000**, *79*, 975–981, doi:10.1016/S0006-3495(00)76351-X.

158. Otto, M. Staphylococcus epidermidis - The “accidental” pathogen. *Nat. Rev. Microbiol.* **2009**, *7*, 555–567, doi:10.1038/nrmicro2182.

159. Boschetto, F.; Adachi, T.; Horiguchi, S.; Fainozzi, D. Monitoring metabolic

reactions in Staphylococcus epidermidis exposed to silicon nitride using in situ time-lapse Raman spectroscopy. *J. Biomed. Opt.* **2018**, *23*, 1, doi:10.1117/1.JBO.23.5.056002.

160. Otto, M. Staphylococcal biofilms. *Curr. Top. Microbiol. Immunol.* **2008**, *322*, 207–228, doi:10.1007/978-3-540-75418-3_10.
161. Beloin, C.; Roux, A.; Ghigo, J. M. Escherichia coli biofilms. *Curr. Top. Microbiol. Immunol.* **2008**, *322*, 249–289, doi:10.1007/978-3-540-75418-3_12.
162. Chao, Y.; Zhang, T. Surface-enhanced Raman scattering (SERS) revealing chemical variation during biofilm formation: From initial attachment to mature biofilm. *Anal. Bioanal. Chem.* **2012**, *404*, 1465–1475, doi:10.1007/s00216-012-6225-y.
163. Neugebauer, U. Characterization of bacteria , antibiotics of the fluoroquinolone type and their biological targets DNA and gyrase utilizing the unique potential of vibrational spectroscopy, Friedrich Schiller University Jena, 2007.
164. Hlaing, M. M. Study of Factors Influencing Bacterial Identification by Raman Spectroscopy, Swinburne University of Technology, 2015.
165. Witkowska, E.; Korsak, D.; Kowalska, A.; Janeczek, A.; Kamińska, A. Strain-level typing and identification of bacteria – a novel approach for SERS active plasmonic nanostructures. *Anal. Bioanal. Chem.* **2018**, *410*, 5019–5031, doi:10.1007/s00216-018-1153-0.
166. Çulha, M.; Adigüzel, A.; Yazici, M. M.; Kahraman, M.; Şahin, F.; Güllüce, M. Characterization of thermophilic bacteria using surface-enhanced Raman scattering. *Appl. Spectrosc.* **2008**, *62*, 1226–1232, doi:10.1366/000370208786401545.
167. Novara, C.; Dalla Marta, S.; Virga, A.; Lamberti, A.; Angelini, A.; Chiadò, A.; Rivolo, P.; Geobaldo, F.; Sergo, V.; Bonifacio, A.; Giorgis, F. SERS-active Ag nanoparticles on porous silicon and PDMS substrates: A comparative study of uniformity and Raman efficiency. *J. Phys. Chem. C* **2016**, *120*, 16946–16953, doi:10.1021/acs.jpcc.6b03852.
168. Athamneh, A. I. M.; Senger, R. S. Peptide-guided surface-enhanced raman scattering probes for localized cell composition analysis. *Appl. Environ. Microbiol.* **2012**, *78*, 7805–7808, doi:10.1128/AEM.02000-12.
169. Shalabaeva, V.; Lovato, L.; La Rocca, R.; Messina, G. C.; Dipalo, M.; Miele, E.; Perrone, M.; Gentile, F.; De Angelis, F. Time resolved and label free monitoring of extracellular metabolites by surface enhanced Raman spectroscopy. *PLoS One* **2017**, *12*, doi:10.1371/journal.pone.0175581.
170. Yang, X.; Gu, C.; Qian, F.; Li, Y.; Zhang, J. Z. Highly sensitive detection of proteins and bacteria in aqueous solution using surface-enhanced raman scattering and optical fibers. *Anal. Chem.* **2011**, *83*, 5888–5894, doi:10.1021/ac200707t.
171. Walter, A.; Reinicke, M.; Bocklitz, T.; Schumacher, W.; Rösch, P.; Kothe, E.; Popp, J. Raman spectroscopic detection of physiology changes in plasmid-bearing Escherichia coli with and without antibiotic treatment. *Anal. Bioanal. Chem.* **2011**, *400*, 2763–2773, doi:10.1007/s00216-011-4819-4.
172. Brazhe, N. A.; Evlyukhin, A. B.; Goodilin, E. A.; Semenova, A. A.; Novikov, S. M.; Bozhevolnyi, S. I.; Chichkov, B. N.; Sarycheva, A. S.; Baizhumanov, A. A.; Nikelshparg, E. I.; Deev, L. I.; Maksimov, E. G.; Maksimov, G. V.; Sosnovtseva, O. Probing cytochrome c in living mitochondria with surface-enhanced Raman spectroscopy. *Sci. Rep.* **2015**, *5*,

1–13, doi:10.1038/srep13793.

173. Zeiri, L.; Bronk, B. V.; Shabtai, Y.; Eichler, J.; Efrima, S. Surface-Enhanced Raman Spectroscopy as a Tool for Probing Specific Biochemical Components in Bacteria. *Appl. Spectrosc.* **2004**, *58*, 33–40, doi:10.1366/000370204322729441.

174. Raetz, C. R. H.; Whitfield, C. LIPOPOLYSACCHARIDE ENDOTOXINS. *Annu. Rev. Biochem.* **1991**, *71*, 635–670, doi:10.1146/annurev.biochem.71.110601.135414.

175. Hirakawa, A. Y.; Nishimura, Y.; Matsumoto, T.; Nakanishi, M.; Tsuboi, M. Characterization of a few Raman lines of tryptophan. *J. Raman Spectrosc.* **1978**, *7*, 282–287, doi:10.1002/jrs.1250070511.

176. Pezzotti, G.; Bock, R. M.; McEntire, B. J.; Jones, E.; Boffelli, M.; Zhu, W.; Baggio, G.; Boschetto, F.; Puppulin, L.; Adachi, T.; Yamamoto, T.; Kanamura, N.; Marunaka, Y.; Bal, B. S. Silicon Nitride Bioceramics Induce Chemically Driven Lysis in Porphyromonas gingivalis. *Langmuir* **2016**, *32*, 3024–3035, doi:10.1021/acs.langmuir.6b00393.

177. Siddhanta, S.; Narayana, C. Surface Enhanced Raman Spectroscopy of Proteins: Implications for Drug Designing. *Nanomater. Nanotechnol.* **2012**, *2*, 1, doi:10.5772/46209.

178. Kurouski, D.; Postiglione, T.; Deckert-Gaudig, T.; Deckert, V.; Lednev, I. K. Amide i vibrational mode suppression in surface (SERS) and tip (TERS) enhanced Raman spectra of protein specimens. *Analyst* **2013**, *138*, 1665–1673, doi:10.1039/c2an36478f.

179. Podstawka, E.; Ozaki, Y. Bombesin-modified 6-14 C-terminal fragments adsorption on silver surfaces: Influence of a surface substrate. *Biopolymers* **2008**, *89*, 941–950, doi:10.1002/bip.21040.

180. Vogel, H.; Jähnig, F. Models for the structure of outer-membrane proteins of Escherichia coli derived from raman spectroscopy and prediction methods. *J. Mol. Biol.* **1986**, *190*, 191–199, doi:10.1016/0022-2836(86)90292-5.

181. Spiliopoulou, A. I.; Krevvata, M. I.; Kolonitsiou, F.; Harris, L. G.; Wilkinson, T. S.; Davies, A. P.; Dimitracopoulos, G. O.; Karamanos, N. K.; Mack, D.; Anastassiou, E. D. An extracellular Staphylococcus epidermidis polysaccharide: Relation to Polysaccharide Intercellular Adhesin and its implication in phagocytosis. *BMC Microbiol.* **2012**, *12*, doi:10.1186/1471-2180-12-76.

182. Liu, H.; Xu, Q.; Huo, L.; Wei, X.; Ling, J. Chemical composition of Enterococcus faecalis in biofilm cells initiated from different physiologic states. *Folia Microbiol. (Praha).* **2014**, *59*, 447–453, doi:10.1007/s12223-014-0319-1.

183. Keleştemur, S.; Çulha, M. Understanding and Discrimination of Biofilms of Clinically Relevant Microorganisms Using Surface-Enhanced Raman Scattering. *Appl. Spectrosc.* **2017**, *71*, 1180–1188, doi:10.1177/0003702816670916.

184. Weinbauer, M. G.; Beckmann, C. Utility of Green Fluorescent Nucleic Acid Dyes and Aluminum Oxide Membrane Filters for Rapid Epifluorescence Enumeration of Soil and Sediment Bacteria. *Appl. Environ. Microbiol.* **1998**, *64*, 5000–5003.

185. Ross, J.; Boon, P. I.; Sharma, R.; Beckett, R. Variations in the fluorescence intensity of intact DAPI-stained bacteria and their implications for rapid bacterial quantification. *Lett. Appl. Microbiol.* **1996**, *22*, 283–287, doi:10.1111/j.1472-765X.1996.tb01162.x.

186. Shi, L.; Günther, S.; Hübschmann, T.; Wick, L. Y.; Harms, H.; Müller, S. Limits of propidium iodide as a cell viability indicator for environmental bacteria. *Cytom. Part A* **2007**, *71*, 592–598, doi:10.1002/cyto.a.20402.

Publications and conferences

International Journal Papers

Boschetto, F.; Adachi, T.; Horiguchi, S.; Marin, E.; *Paccotti, N.*; Asai, T.; Zhu, W.; Mcentire, B. J.; Yamamoto, T.; Kanamura, N.; Mazda, O.; Ohgitani, E.; Pezzotti, G. In situ molecular vibration insights into the antibacterial behavior of silicon nitride bioceramic versus gram-negative Escherichia coli. Spectrochim. Acta Part A Mol. Biomol. Spectrosc. 2019, 223, 117299, doi:10.1016/j.saa.2019.117299.

Paccotti, N.; Boschetto, F.; Horiguchi, S.; Marin, E.; Chiadò, A.; Novara, C.; Geobaldo, F.; Giorgis, F.; Pezzotti, G. Label-Free SERS Discrimination and In Situ Analysis of Life Cycle in Escherichia coli and Staphylococcus epidermidis. *Biosensors* **2018**, *8*, 131, doi:10.3390/bios8040131.

Novara, C.; Chiadò, A.; Paccotti, N.; Catuogno, S.; Esposito, C. L.; Condorelli, G.; De Franciscis, V.; Geobaldo, F.; Rivolo, P.; Giorgis, F. SERS-active metal-dielectric nanostructures integrated in microfluidic devices for label-free quantitative detection of miRNA. *Faraday Discuss.* **2017**, *205*, 271–289, doi:10.1039/c7fd00140a

International Conferences

C. Novara, A. Chiadò, G. Caruso, R. Calmo, N. Paccotti, F. Geobaldo, P. Rivolo, M. Bertoldi, P. Puppo, F. Giorgis. In situ growth of silver nanoparticles on PDMS membranes for multi-wavelength SERS biosensing platforms. Plasmonica 2019, 19-21 Giugno 2019

A. Chiadò, C. Novara, N. Paccotti, P. Rivolo, G. Biasotto, R. Nisticò, G. Condorelli, V. de Franciscis, F. Geobaldo, F. Giorgis. Plasmonic Nanostructures Integrated in Microfluidic Chips for the Sensitive SERS Detection of miRNAs. 2019 - 7th International Symposium on Sensor Science, 9-11 Maggio 2019

SERS Analysis of Bacterial Strains: Escherichia coli and Staphylococcus epidermidis. N. Paccotti, A. Chiadò, C. Novara, F. Giorgis, F. Geobaldo, F. Boschetto, E. Marin, S. Horiguchi, G. Pezzotti. 2019 - 7th International Symposium on Sensor Science, 9-11 Maggio 2019

Chiadò A., C. Novara, Paccotti N., Geobaldo F., Rivolo P., Giorgis F. Study of aptamer immobilization on plasmonic surfaces by SERS analysis. 2018 - Plasmonica 2018, July 4-6, 2018

Novara C., Biasotto G., Nisticò R., Chiadò A., Paccotti N., Fontana M., Armandi M., Zaghete M.A., Geobaldo F., Rivolo P., Giorgis F. Porous plasmonic nanostructures for Surface Enhanced Raman Scattering: development of biosensing platforms. 2018 - Plasmonica 2018, July 4-6, 2018

C. Novara, A. Chiadò, A. Lamberti, N. Paccotti, P. Rivolo, S. Bianco, F. Geobaldo, F. Giorgis. Smart solid Surface Enhanced Raman Scattering substrates for biosensing applications. 2017 - SERS: Faraday Discussions, Aug 30-Sep 01

C. Novara, A. Lamberti, N. Paccotti, A. Chiadò, P. Rivolo, F. Geobaldo, F. Giorgis. Microfluidic growth of Ag nanoparticles onto porous silicon/PDMS surface for reliable SERS detection. 2017 - Plasmonica 2017, July 5-7, 2017

C. Novara, A. Chiadò, N. Paccotti, G. Condorelli, V. de Franciscis, F. Geobaldo, P. Rivolo, F. Giorgis. Microfluidic SERS chips for the selective detection of miRNAs in biological matrixes. 2017 - Plasmonica 2017, July 5-7, 2017

Appendix

A. Dynamic flow synthesis

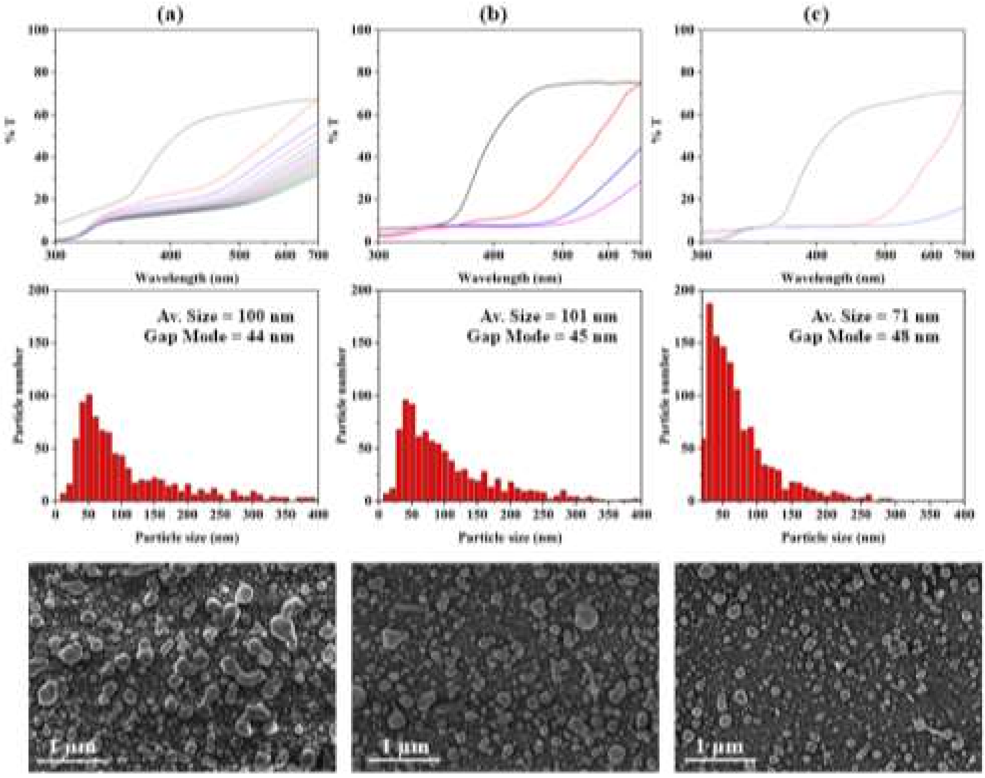

Figure A.1 - UV-Vis transmittance spectra, particle size distribution, and FESEM micrographs for the samples synthetized in static conditions using a 100 mM $AgNO_3$ at a) 20 °C b) 40 °C and c) 60 °C.

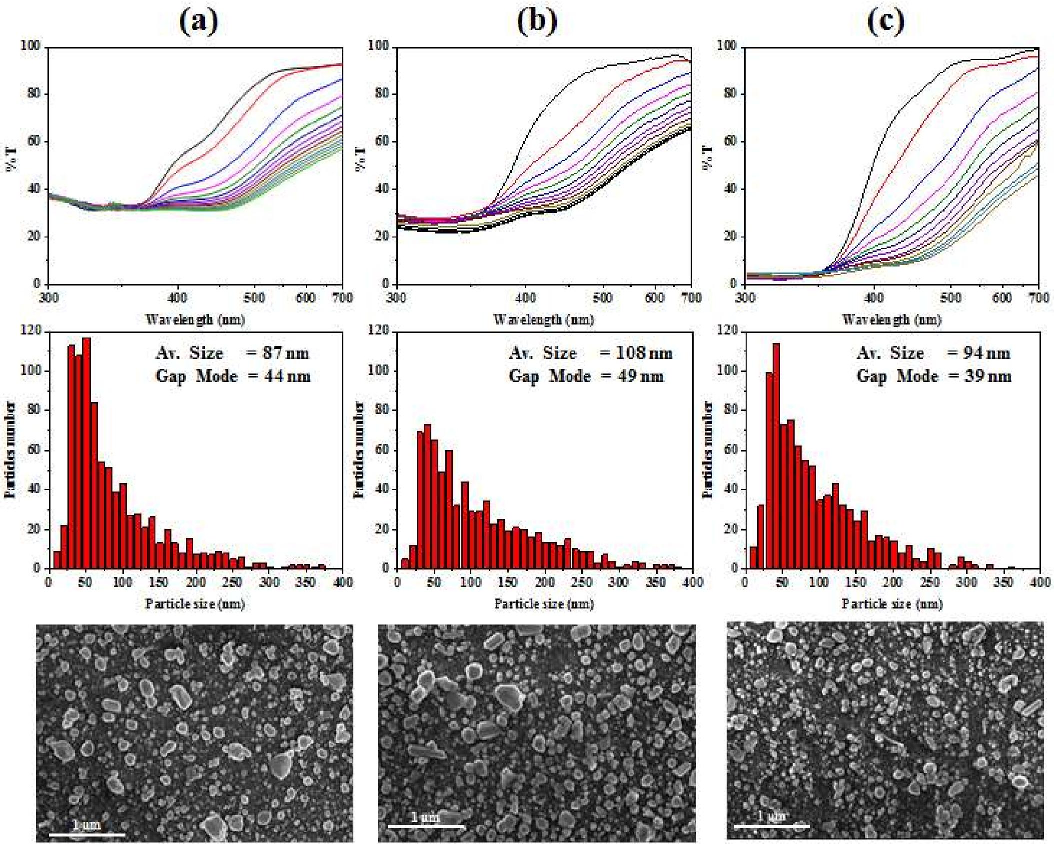

Figure A.2 – UV-Vis transmittance spectra, particle size distribution, and FESEM micrographs for the samples synthetized in dynamic conditions using a 10 mM $AgNO_3$ at 40 °C employing a flow rate of a) 1 ml/min b) 2 ml/min c) 3 ml/min.

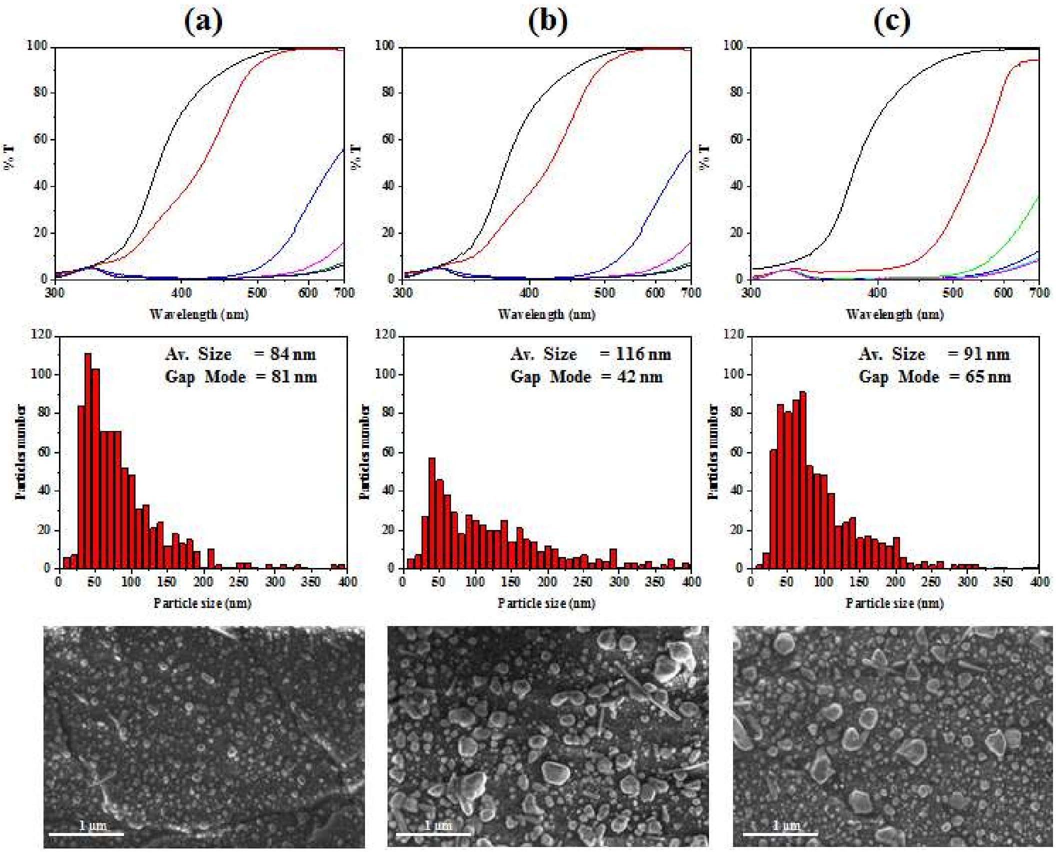

Figure A.3 - UV-Vis transmittance spectra, particle size distribution, and FESEM micrographs for the samples synthetized in dynamic conditions using a 100 mM $AgNO_3$ at 40 °C employing a flow rate of a) 1 ml/min b) 2 ml/min c) 3 ml/min.

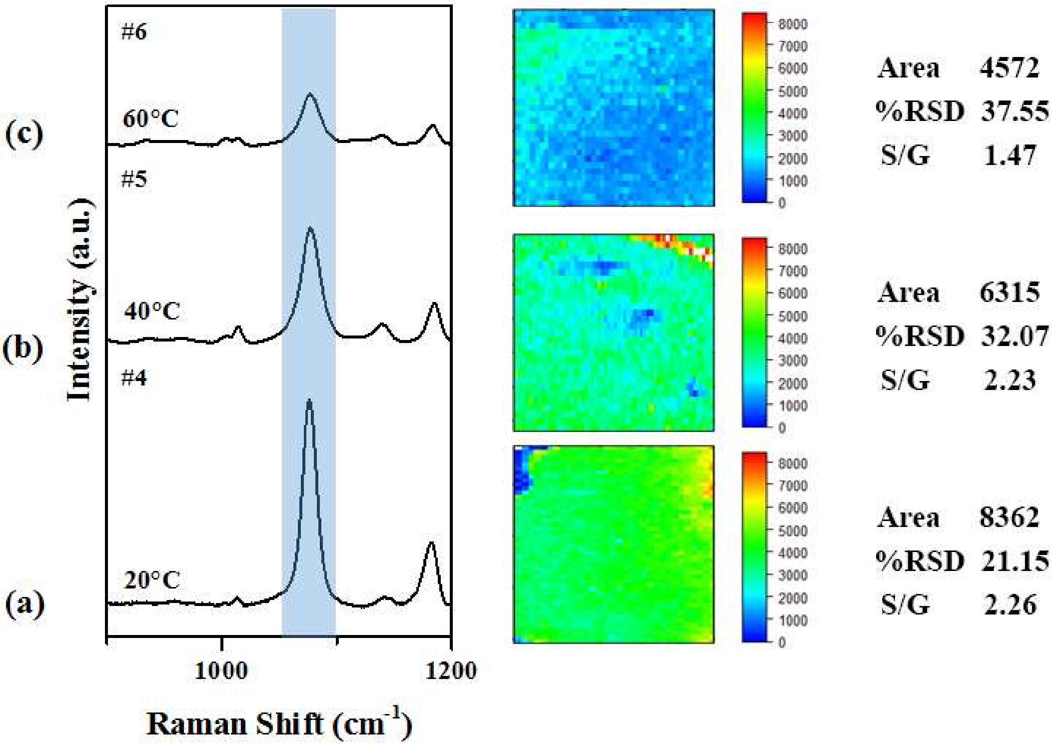

Figure A.4 - SERS efficiency and reproducibility evaluation for samples synthetized in static conditions using a 10 mM $AgNO_3$ solution at a) 20 °C b) 40 °C and c) 60 °C. SERS spectrum and the related false colour maps of the integrated area of the 1077 cm^{-1} peak are reported on the left and in the centre, respectively, of the graph. On the right side, the numerical value of the integrated area of the

highlighted band and its %RSD along with the size-gap ratio obtained by the FESEM images, are reported.

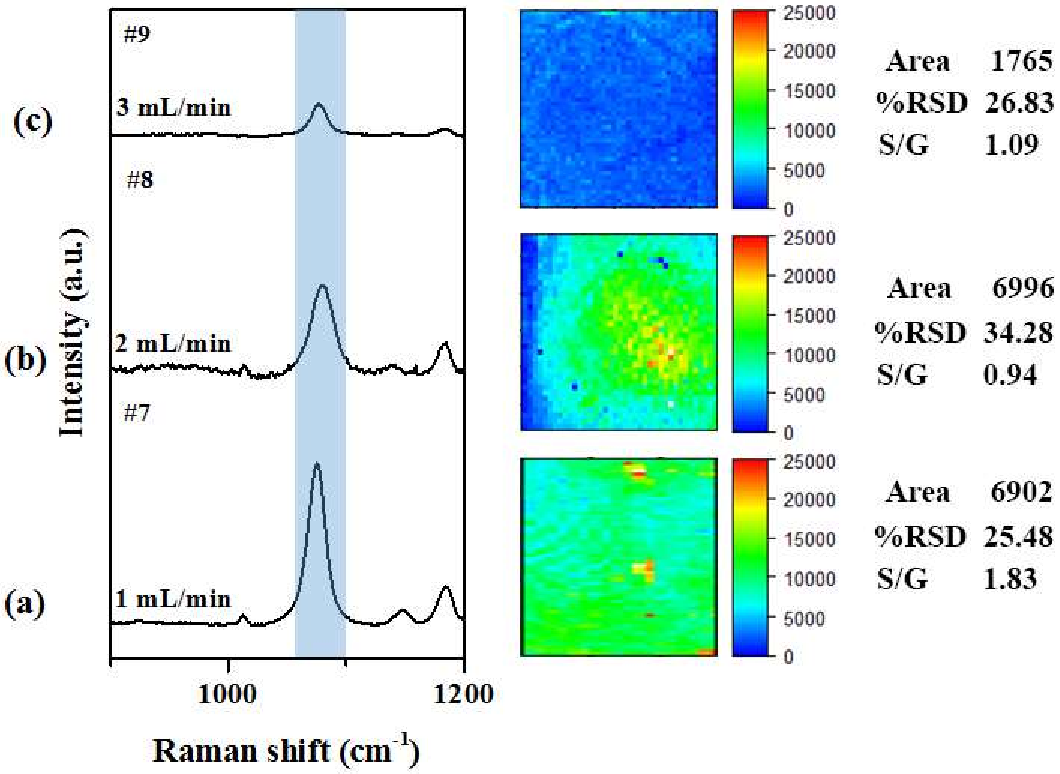

Figure A.5 - SERS efficiency and reproducibility evaluation for samples synthetized using a 10 mM $AgNO_3$ at 20 °C with a flow rate of a) 1 ml/min b) 2 ml/min and c) 3 ml/min. SERS spectrum and the related false colour maps of the integrated area of the 1077 cm^{-1} peak are reported on the left and in the centre, respectively, of the graph. On the right side, the numerical value of the integrated area of the highlighted band and its %RSD along with the size-gap ratio obtained by the FESEM images, are reported.

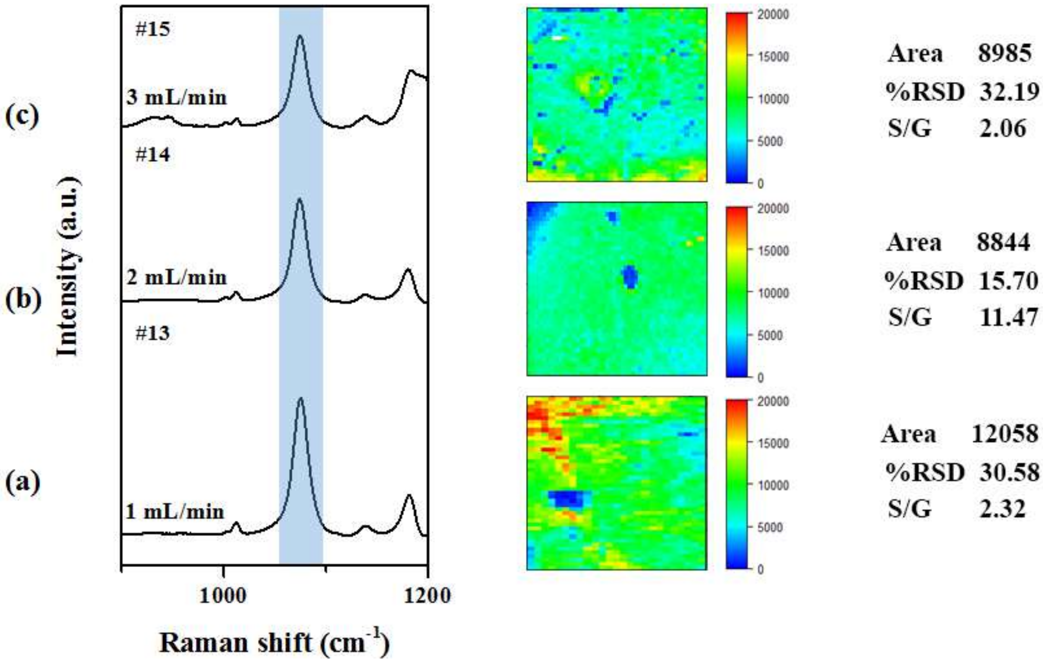

Figure A.6 - SERS efficiency and reproducibility evaluation for samples synthetized using a 10 mM $AgNO_3$ at 60 °C with a flow rate of a) 1 ml/min b) 2 ml/min and c) 3 ml/min. SERS spectrum and the related false colour maps of the integrated area of the 1077 cm^{-1} peak are reported on the left and in the

centre, respectively, of the graph. On the right side, the numerical value of the integrated area of the highlighted band and its %RSD along with the size-gap ratio, are reported.

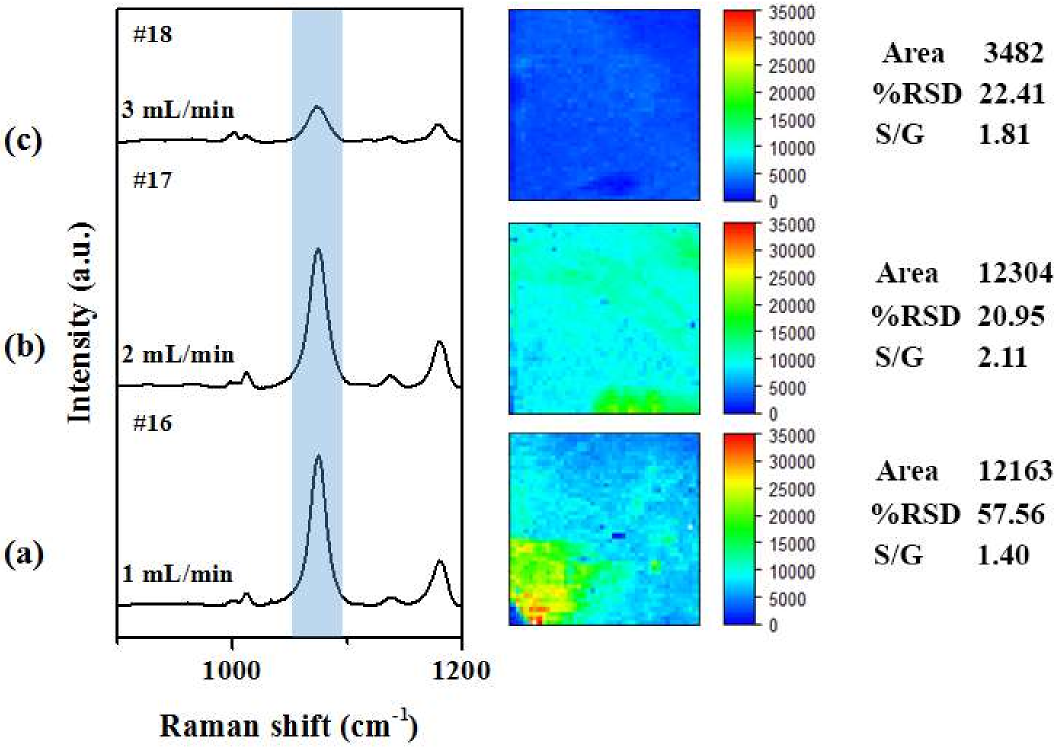

Figure A.7 - SERS efficiency and reproducibility evaluation for samples synthesized using a 100 mM $AgNO_3$ at 20 °C with a flow rate of a) 1 ml/min b) 2 ml/min and c) 3 ml/min. SERS spectrum and the related false colour maps of the integrated area of the 1077 cm^{-1} peak are reported on the left and in the centre, respectively, of the graph. On the right side, the numerical value of the integrated area of the highlighted band and its %RSD along with the size-gap ratio obtained by the FESEM images, are reported.

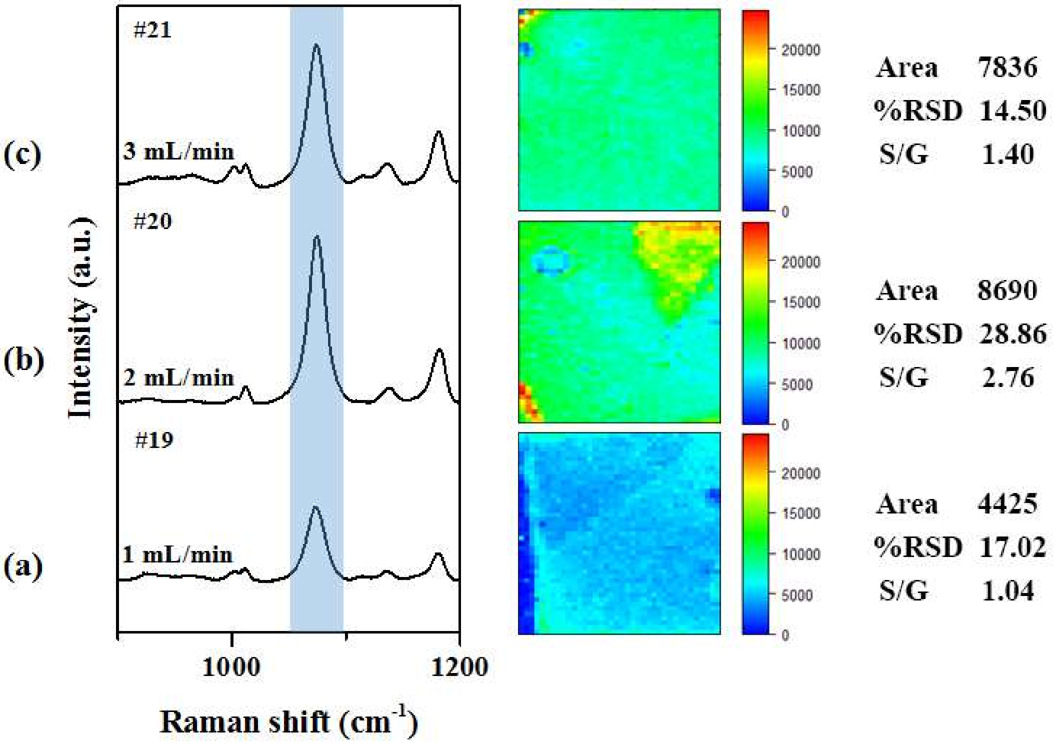

Figure A.8 - SERS efficiency and reproducibility evaluation for samples synthesized using a 100 mM $AgNO_3$ at 40 °C with a flow rate of a) 1 ml/min b) 2 ml/min and c) 3 ml/min. SERS spectrum and

the related false colour maps of the integrated area of the 1077 cm^{-1} peak are reported on the left and in the centre, respectively, of the graph. On the right side, the numerical value of the integrated area of the highlighted band and its %RSD along with the size-gap ratio obtained by the FESEM images, are reported.

Appendix C